การเตรียม $La_{1-x}Sr_xFeO_3$ (LSF) - $La_{0.8}Sr_{0.2}Co_{1-x}Fe_xO_3$ (LSCF) คอมโพสิตแคโทดสำหรับเซลล์เชื้อเพลิงแบบออกไซด์ของแข็ง

นางสาวเพชรพลอย วิเชียรรธวัชชัย

วิทยานิพนธ์นี้เป็นส่วนหนึ่งของการศึกษาตามหลักสูตรปริญญาวิทยาศาสตรมหาบัณฑิต
สาขาวิชาปิโตรเคมีและวิทยาศาสตร์พอลิเมอร์
คณะวิทยาศาสตร์ จุฬาลงกรณ์มหาวิทยาลัย
ปีการศึกษา 2553

PREPARATION OF $La_{1-x}Sr_xFeO_3$ (LSF) - $La_{0.8}Sr_{0.2}Co_{1-x}Fe_xO_3$ (LSCF) COMPOSITE CATHODES FOR SOLID OXIDE FUEL CELL

Miss Petploy Vicheantawatchai

A Thesis Submitted in Partial Fulfillment of the Requirements
for the Degree of Master of Science Program in Petrochemistry and Polymer Science
Faculty of Science
Chulalongkorn University
Academic Year 2010

Thesis Title	PREPARATION OF $La_{1-x}Sr_xFeO_3$ (LSF) - $La_{0.8}Sr_{0.2}Co_{1-x}Fe_xO_3$ (LSCF) COMPOSITE CATHODES FOR SOLID OXIDE FUEL CELL
By	Miss Petploy Vicheantawatchai
Field of Study	Petrochemistry and Polymer Science
Thesis Advisor	Assistant Professor Oravan Sanguanruang, Ph.D.

Accepted by the Faculty of Science, Chulalongkorn University in Partial Fulfillment of the Requirements for the Master's Degree

.....Dean of the Faculty of Science

(Professor Supot Hannongbua, Dr.rer.nat.)

THESIS COMMITTEE

.....Chairman

(Professor Pattarapan Prasassarakich, Ph.D.)

.....Thesis Advisor

(Assistant Professor Oravan Sanguanruang, Ph.D.)

.....Examiner

(Associate Professor Wimonrat Trakarnpruk, Ph.D.)

.....External Examiner

(Associate Professor Preecha Phahonthep)

เพชรพลอย วิเชียรธวัชชัย : การเตรียม $La_{1-x}Sr_xFeO_3$ (LSF) - $La_{0.8}Sr_{0.2}Co_{1-x}Fe_xO_3$ (LSCF) คอมโพสิตแคโทด สำหรับเซลล์เชื้อเพลิงแบบออกไซด์ของแข็ง (PREPARATION OF $La_{1-x}Sr_xFeO_3$ (LSF) - $La_{0.8}Sr_{0.2}Co_{1-x}Fe_xO_3$ (LSCF) COMPOSITE CATHODES FOR SOLID OXIDE FUEL CELL) อ. ที่ปรึกษาวิทยานิพนธ์หลัก: ผศ. ดร. อรวรรณ สงวนเรือง, 122 หน้า

วัสดุคอมโพสิตถูกเตรียมด้วยวิธีทางกายภาพโดยผสม $La_{1-x}Sr_xFeO_{3-\delta}$ (x = 0.6 และ 0.7) กับ $La_{0.8}Sr_{0.2}Co_{1-x}Fe_xO_{3-\delta}$ (x = 0.1 และ 0.2) ในอัตราส่วนต่างๆ คือ 1:2, 1:3, 1:1, 3:1 และ 2:1 โดยศึกษาถึงผลของอุณหภูมิในการเผา อุณหภูมิซินเทอริงและเวลาในการซินเทอริงที่มีต่อลักษณะโครงสร้างและสมบัติต่างๆของสารเพอรอฟสไกต์ LSF-LSCF ผลการวิเคราะห์ด้วยเทคนิคการเลี้ยวเบนของรังสีเอ็กซ์ (XRD) แสดงว่าเฟสของสารเพอรอฟสไกต์ LSF-LSCF เกิดขึ้นหลังจากทำการเผาที่อุณหภูมิ 800 และ 900 องศาเซลเซียส จากการศึกษาโดยกล้องจุลทรรศน์อิเล็กตรอนแบบส่งกราด (SEM) แสดงว่าลักษณะสัณฐานของแผ่นเพอรอฟสไกต์ออกไซด์มีโครงสร้างระดับไมโครที่หนาแน่น ขนาดเกรนของ LSF-LSCF คอมโพสิตเพิ่มขึ้นเมื่อเพิ่มปริมาณของ LSCF และอุณหภูมิซินเทอริงแต่ขนาดเกรนลดลงเมื่อเวลาในการซินเทอริงเพิ่มขึ้น การวัดค่าการนำไฟฟ้าโดยใช้ขั้วกระแสตรงชนิด 4 ขั้วในอากาศแสดงให้เห็นว่าค่าการนำไฟฟ้าของสารคอมโพสิตเพิ่มขึ้นเมื่อเพิ่มปริมาณของ LSCF ผลการนำไฟฟ้าของสารคอมโพสิต LSF-LSCF ที่อัตราส่วน 1:3 มีค่าสูงที่สุดเมื่ออุณหภูมิซินเทอริงที่ 1300°C เป็นเวลา 10 ชั่วโมง ซึ่งค่าการนำไฟฟ้าของ LSF37-LSCF8291 มีค่าสูงที่สุดที่ 1,000.90 ซีเมนต์ต่อเซนติเมตร ณ 650 องศาเซลเซียส ในการวิเคราะห์การขยายตัวทางความร้อน พบว่า ค่าสัมประสิทธิ์การขยายตัวทางความร้อนของ LSF-LSCF คอมโพสิตลดลงด้วยการเติม LSF ซึ่งค่าสัมประสิทธิ์การขยายตัวทางความร้อนต่ำที่สุดที่ 18.10×10^{-6} ต่อองศาเซลเซียส สำหรับ LSF46-LSCF8291

สาขาวิชา ปิโตรเคมีและวิทยาศาสตร์พอลิเมอร์ ลายมือชื่อนิสิต เพชรพลอย วิเชียรธวัชชัย

ปีการศึกษา 2553 ลายมือชื่อ อ.ที่ปรึกษาวิทยานิพนธ์หลัก อรวรรณ สงวนเรือง

5172393023 : MAJOR PETROCHEMISTRY AND POLYMER SCIENCE
KEYWORDS: PEROVSKITE OXIDE/ COMPOSITE/ LSF/ LSCF/ ELECTRICAL CONDUCTIVITY/ THERMAL EXPANSION COEFFICIENT

PETPLOY VICHEANTAWATCHAI: PREPARATION OF $La_{1-x}Sr_xFeO_3$ (LSF) - $La_{0.8}Sr_{0.2}Co_{1-x}Fe_xO_3$ (LSCF) COMPOSITE CATHODES FOR SOLID OXIDE FUEL CELL. ADVISOR: ASST. PROF. ORAVAN SANGUANRUANG, Ph.D., 122 pp.

Composite materials were prepared by physical mixing of $La_{1-x}Sr_xFeO_{3-\delta}$ (x = 0.6 and 0.7) with $La_{0.8}Sr_{0.2}Co_{1-x}Fe_xO_{3-\delta}$ (x = 0.1 and 0.2) in various ratios: 1:2, 1:3, 1:1, 3:1 and 2:1. The influences of calcination temperature, sintering temperature and sintering time on the structures and properties of LSF-LSCF perovskite were investigated. X-ray diffraction (XRD) patterns showed that LSF-LSCF perovskite phase was formed after calcination at 800°C and 900°C. Using SEM, the morphology of the perovskite oxide discs revealed dense microstructures. The grain sizes of LSF-LSCF composites increased with increasing the amount of LSCF and the sintering temperature, but decreased with increasing the sintering time. Conductivity measurements using DC 4-probe in air exhibited that the conductivity of the composites increased with increasing the amounts of LSCF. The conductivity performance of the 1:3 LSF-LSCF composite was maximized by sintering at 1300°C for 10 hours. The specific conductivity of LSF37-LSCF8291 reached the maximum value of 1,000.90 S/cm at 650 °C. For thermal expansion analysis, the TEC values of LSF-LSCF composites reduced with mixing LSF. The lowest thermal expansion coefficient is 18.10×10^{-6} °C^{-1} for LSF46-LSCF8291.

Field of Study: Petrochemistry and Polymer Science Student's Signature Petploy Vicheantawatchai
Academic Year: 2010 Advisor's Signature Oravan Sanguanruang

ACKNOWLEDGEMENTS

The success of this thesis can be attributed to the extensive support and assistance from Assistant Professor Dr. Oravan Saguanruang. I deeply thank her for hers valuable advice and guidance in this research and hers kindness throughout this study.

I would like to gratitude Professor Dr. Pattarapan Prasassarakich, Associate Professor Dr. Wimonrat Trakarnpruk and Associate Professor Preecha Phahonthep as the chairman and members of this thesis committee, respectively, for all of their kindness and useful advice in the research.

I would like to gratefully thank Dr. Thanakorn Wasanapiarnpong from Department of Material Science, Faculty of Science, Chulalongkorn University for supporting many instruments. Moreover, I would like to thank Department of Chemistry, Faculty of Science, Chulalongkorn University for the valuable knowledge and experience. In addition, Thailand Japan Technology Transfer Project supported a loan by Japan Banks for International Cooperation (TJTTP-JBIC) for instrument support and National Center of Excellence for Petroleum, Petrochemicals, and Advanced Materials (NCE-PPAM). Furthermore, I would like to thank the members of Materials Chemistry and Catalysis Research Unit for their kind assistance and generosity.

For all of my friends, I greatly appreciate their help and encouragement throughout the course of my research and study.

Finally, I would like to express my deepest gratitude to my family for their entirely care and support. The usefulness of this thesis, I dedicate to my family and all teachers who have taught me since my childhood.

CONTENTS

Page

ABSTRACT IN THAI iv

ABSTRACT IN ENGLISH v

ACKNOWNLEDGEMENTS vi

CONTENTS vii

LIST OF TABLES x

LIST OF FIGURES xii

LIST OF ABBREVIATIONS xvii

CHAPTER I INTRODUCTION 1

1.1 Fuel cells 1

1.2 Solid oxide fuel cells 3

1.2.1 Operation of solid oxide fuel cells 4

1.2.2 Components of solid oxide fuel cells 6

1.2.2.1 Electrolyte 6

1.2.2.2 Anode 7

1.2.2.3 Cathode 7

1.2.2.4 Interconnect 8

1.3 Perovskite 8

1.3.1 Structure of perovskite oxides 9

1.3.2 Nonstoichiometry in perovskites 10

1.3.3 Physical properties 11

1.3.3.1 Magnetic properties 11

1.3.3.2 Electrical properties 12

1.3.3.3 Mixed ionic-electronic conductors 14

1.3.4 Oxygen permeation property 15

1.3.5 Perovskite synthesis 17

1.3.5.1 Solid-state reaction 17

1.3.5.2 Sol-gel techniques 18

1.3.5.3 Co-precipitation 20

1.3.5.4 Hydrothermal synthesis 20

1.3.5.5 Spray and freeze drying 21

1.3.6 Calcination 21

Page

1.3.7 Sintering 22
1.4 Literature reviews 24
1.5 The objectives of the thesis 28

CHAPTER II EXPERIMENTAL 29
2.1 Chemicals 29
2.2 Synthesis of perovskite powder 29
2.2.1 $La_{0.3}Sr_{0.7}FeO_{3-\delta}$ (LSF37) and $La_{0.4}Sr_{0.6}FeO_{3-\delta}$ (LSF46) 29
2.2.2 $La_{0.8}Sr_{0.2}Co_{0.8}Fe_{0.2}O_{3-\delta}$ (LSCF8282) and $La_{0.8}Sr_{0.2}Co_{0.9}Fe_{0.1}O_{3-\delta}$ (LSCF8291) 30
2.3 Preparation of composite perovskite powder by physical method 31
2.4 Perovskite disc preparation 32
2.5 The sintering of the perovskite oxides 33
2.6 Characterization techniques 34
2.6.1 X–ray diffractrometry (XRD) 34
2.6.2 Scanning electron microscopy (SEM) 34
2.7 The investigation of the perovskite properties 34
2.7.1 Density measurement 34
2.7.2 Electrical conductivity measurement 34
2.7.3 Thermal expansion measurement 35

CHAPTER III RESULTS AND DISSCUSSIONS 37
3.1 Synthesis of perovskite 37
3.1.1 $La_{1-x}Sr_xFeO_{3-\delta}$ (LSF) (x = 0.6 and 0.7) by modified citrate method 37
3.1.2 $La_{0.8}Sr_{0.2}Co_{1-x}Fe_xO_{3-\delta}$ (LSCF) (x = 0.1 and 0.2) by citrate method 38
3.1.3 $La_{1-x}Sr_xFeO_{3-\delta}$ (LSF) - $La_{0.8}Sr_{0.2}Co_{1-x}Fe_xO_{3-\delta}$ (LSCF) composites by physical mixing method 38
3.2 Characterization of the synthesized compounds 39
3.2.1 X-ray diffraction (XRD) 39
3.2.1.1 Phase formation of $La_{1-x}Sr_xFeO_{3-\delta}$ (x = 0.6 and 0.7) 39

Page

3.2.1.2 Phase formation of $La_{0.8}Sr_{0.2}Co_{1-x}Fe_xO_{3-\delta}$ (x = 0.1 and 0.2) 40
3.2.1.3 Phase formation of LSF-LSCF composites 42
3.2.2 Scanning electron microscope (SEM) and density 52
3.2.2.1 Morphologies of $La_{1-x}Sr_xFeO_{3-\delta}$ (x = 0.6 and 0.7) 52
3.2.2.2 Morphologies of $La_{0.8}Sr_{0.2}Co_{1-x}Fe_xO_{3-\delta}$ (x = 0.1 and 0.2) 53
3.2.2.3 Morphologies of LSF-LSCF composites 54
3.3 Properties of perovskite compounds 64
3.3.1 Electrical conductivity 64
3.3.1.1 Electrical conductivity of $La_{1-x}Sr_xFeO_{3-\delta}$ (x = 0.6 and 0.7) 64
3.3.1.2 Electrical conductivity of $La_{0.8}Sr_{0.2}Co_{1-x}Fe_xO_{3-\delta}$ (x = 0.1 and 0.2) 67
3.3.1.3 Electrical conductivity of LSF-LSCF composites 69
3.3.2 Thermal expansion coefficients 87
3.3.2.1 Thermal expansion coefficients of $La_{1-x}Sr_xFeO_{3-\delta}$ (x = 0.6 and 0.7) 88
3.3.2.2 Thermal expansion coefficients of $La_{0.8}Sr_{0.2}Co_{1-x}Fe_xO_{3-\delta}$ (x = 0.1 and 0.2) 89
3.3.2.3 Thermal expansion coefficients of LSF-LSCF composites 91

CHAPTER IV CONCLUSIONS 93
REFERENCES 95
APPENDICES 100
APPENDIX A 101
APPENDIX B 102
APPENDIX C 104
VITAE 122

LIST OF TABLES

Table **Page**

1.1 Types of fuel cells..... 2

2.1 Reagents for synthesis of perovskites.....29

3.1 The lattice parameters of $La_{1-x}Sr_xFeO_{3-\delta}$ (x = 0.6 and 0.7) after calcined at 900°C for 6 hours.....40

3.2 The lattice parameters of $La_{0.8}Sr_{0.2}Co_{1-x}Fe_xO_{3-\delta}$ (x = 0.1 and 0.2) after calcined at 800°C for 4 hours.....41

3.3 The lattice parameters of LSF-LSCF composites in a weight ratio of 1:3 after calcined at 800^{o}C with different sintering temperature for 10 hours in air.....48

3.4 The lattice parameters of LSF-LSCF composites in a weight ratio of 1:3 after calcined at 800^{o}C with different sintering time for sinterd at 1,300^{o}C in air.....51

3.5 Density of $La_{1-x}Sr_xFeO_{3-\delta}$ (x = 0.6 and 0.7) discs.....52

3.6 Density of $La_{0.8}Sr_{0.2}Co_{1-x}Fe_xO_{3-\delta}$ (x = 0.1 and 0.2) discs.....53

3.7 Density of LSF37-LSCF8291 and LSF37-LSCF8282 composite discs with different weight ratios of LSCF.....57

3.8 Density of LSF46-LSCF8291 and LSF46-LSCF8282 composite discs with different weight ratios of LSCF.....58

3.9 Density of LSF-LSCF composite discs in a weight ratios of 1:3 after calcined at 800^{o}C with different sintering temperatures for 10 hours.....60

3.10 Density of LSF-LSCF composite discs in a weight ratios of 1:3 after calcined at 800^{o}C with different sintering times for sintered at 1,300^{o}C.....63

3.11 Maximum specific conductivity of $La_{1-x}Sr_xFeO_{3-\delta}$ (x = 0.3-0.7).....65

3.12 Activation energy of $La_{1-x}Sr_xFeO_{3-\delta}$ (x = 0.6 and 0.7).....66

3.13 Maximum specific conductivity of $La_{0.8}Sr_{0.2}Co_{1-x}Fe_xO_{3-\delta}$ (x = 0.0-0.5).....67

3.14 Activation energy of $La_{0.8}Sr_{0.2}Co_{1-x}Fe_xO_{3-\delta}$ (x = 0.1 and 0.2).....69

3.15 Maximum specific conductivity of LSF37-LSCF8291 and LSF37-LSCF8282 composites with different weight ratios of LSCF.....72

Table **Page**

3.16 Maximum specific conductivity of LSF46-LSCF8291 and LSF46-LSCF8282 composites with different weight ratios of LSCF.....73

3.17 Activation energy of LSF37-LSCF8291 and LSF37-LSCF8282 composites with different weight ratios of LSCF.....76

3.18 Activation energy of LSF46-LSCF8291 and LSF46-LSCF8282 composites with different weight ratios of LSCF.....78

3.19 Maximum specific conductivity of LSF-LSCF composites in a weight ratio of 1:3 after calcined at 800^{o}C with different sintering temperatures for 10 hours.....80

3.20 Activation energy of LSF-LSCF composites in a weight ratio of 1:3 after calcined at 800^{o}C with different sintering temperature for 10 hours.....82

3.21 Maximum specific conductivity of LSF-LSCF composites in a weight ratio of 1:3 after calcined at 800^{o}C with different sintering time for sinterd at 1,300^{o}C.....84

3.22 Activation energy of LSF-LSCF composites in a weight ratio of 1:3 after calcined at 800^{o}C with different sintering time for sintered at 1,300^{o}C.....86

3.23 Maximum specific conductivity of LSF-LSCF8291 composites in a weight ratio of 1:3 after calcined at 800^{o}C and sintered at 1,300^{o}C for 10 hours.....86

3.24 The TEC values of $La_{1-x}Sr_xFeO_3$ (x = 0.6 and 0.7) 89

3.25 The TEC values of $La_{0.8}Sr_{0.2}Co_{1-x}Fe_xO_{3-\delta}$ (x = 0.0-0.2) 90

3.26 The TEC values of LSF-LSCF composites in a weight ratio of 1:3 after calcined at 800^{o}C and sintered at 1,300^{o}C for 10 hours.....91

3.27 The TEC values of LSF-LSCF8291 composites in a weight ratio of 1:3 after calcined at 800^{o}C and sintered at 1,300^{o}C for 10 hours.....92

LIST OF FIGURES

Figure **Page**

1.1 Tubular and flat plate Solid oxide fuel cell 3

1.2 Operating concept of a SOFC 4

1.3 ABO_3 ideal perovskite structure 9

1.4 The relationship of ionic radii in perovskite structure 10

1.5 DC 4-probemethod 13

1.6 Oxygen transport through a perovskite type membrane 16

1.7 Mechanism of sintering; *X* is the internal radius of the neck; *r* is the particle radius 23

2.1 The condition of calcination for LSF 30

2.2 The condition of calcination for LSCF 31

2.3 The condition of calcination for LSF-LSCF 32

2.4 KBr die 32

2.5 The sintering conditions of perovskite (a) LSF (b) LSCF and (c) LSF-LSCF composite 33

2.6 DC 4-probes measurement 35

3.1 XRD patterns of $La_{1-x}Sr_xFeO_{3-\delta}$ (x = 0.6 and 0.7) powders after calcined at 900°C for 6 hours 39

3.2 XRD patterns of $La_{0.8}Sr_{0.2}Co_{1-x}Fe_xO_{3-\delta}$ (x = 0.1 and 0.2) powders after calcined at 800°C for 4 hours 41

3.3 XRD patterns of LSF37-LSCF8291 composite in a weight ratio of 1:3 at calcination temperature 800-1,000^oC for 10 hours in air 42

3.4 XRD patterns of LSF-LSCF composites with different weight ratios. (a) LSF37-LSCF8291 after calcined at 800^oC, (b) LSF37-LSCF8291 after calcined at 900^oC, (c) LSF37-LSCF8282 after calcined at 800^oC and (d) LSF37-LSCF8282 after calcined at 900^oC 43

Figure **Page**

3.5 XRD patterns of LSF-LSCF composites with various weight ratios. (a) LSF46-LSCF8291 after calcined at 800^{o}C, (b) LSF46-LSCF8291 after calcined at 900^{o}C, (c) LSF46-LSCF8282 after calcined at 800^{o}C and (d) LSF46-LSCF8282 after calcined at 900^{o}C 44

3.6 Magnified XRD pattern of LSF37-LSCF8291 composite with various weight ratios after calcined at 800^{o}C 45

3.7 XRD patterns of LSF-LSCF composites in a weight ratio of 1:3 after calcined at 800^{o}C with different sintering temperatures for 10 hours in air. (a) LSF37-LSCF8291, (b) LSF37-LSCF8282, (c) LSF46-LSCF8291 and (d) LSF46-LSCF8282 46

3.8 Magnified XRD pattern of LSF46-LSCF8291 composite with different sintering temperatures for 10 hours 47

3.9 XRD patterns of LSF-LSCF composites in a weight ratio of 1:3 after calcined at 800^{o}C with different sintering time for sintered at 1,300^{o}C in air. (a) LSF37-LSCF8291, (b) LSF37-LSCF8282, (c) LSF46-LSCF8291 and (d) LSF46-LSCF8282 49

3.10 Magnified XRD patterns of LSF37-LSCF8282 with different sintering time for sintered at 1,300^{o}C 50

3.11 Surface morphology of $La_{1-x}Sr_xFeO_{3-\delta}$ (x = 0.6 and 0.7) discs 52

3.12 Surface morphology of $La_{0.8}Sr_{0.2}Co_{1-x}Fe_xO_{3-\delta}$ (x = 0.1 and 0.2) discs 53

3.13 Surface morphology of LSF37-LSCF8291 composite discs 54

3.14 Surface morphology of LSF37-LSCF8282 composite discs 54

3.15 SEM pictures of cross section of LSF37-LSCF8291 and LSF37-LSCF8282 composite discs 55

3.16 Surface morphology of LSF46-LSCF8291 composite discs 55

3.17 Surface morphology of LSF46-LSCF8282 composite discs 56

3.18 SEM pictures of cross section of LSF46-LSCF8291 and LSF46-LSCF8282 composite discs 56

3.19 Surface morphology of LSF37-LSCF8291 composite discs 59

3.20 Surface morphology of LSF37-LSCF8282 composite discs 59

3.21 Surface morphology of LSF46-LSCF8291 composite discs 59

Figure **Page**

3.22 Surface morphology of LSF46-LSCF8282 composite discs 59
3.23 Surface morphology of LSF37-LSCF8291 composite discs 61
3.24 Surface morphology of LSF37-LSCF8282 composite discs 61
3.25 Surface morphology of LSF46-LSCF8291 composite discs 62
3.26 Surface morphology of LSF46-LSCF8282 composite discs 62
3.27 Temperature dependence of the specific conductivity (σ) for $La_{1-x}Sr_xFeO_{3-\delta}$ (x = 0.6 and 0.7) 64
3.28 Arrhenius plot of the electrical conductivity of $La_{1-x}Sr_xFeO_{3-\delta}$ (x = 0.6 and 0.7) 66
3.29 Temperature dependence of the specific conductivity (σ) for $La_{0.8}Sr_{0.2}Co_{1-x}Fe_xO_{3-\delta}$ (x = 0.1 and 0.2) 67
3.30 Arrhenius plot of the electrical conductivity of $La_{0.8}Sr_{0.2}Co_{1-x}Fe_xO_{3-\delta}$ (x = 0.1 and 0.2) 68
3.31 Temperature dependence of the specific conductivity (σ) for LSF-LSCF composites with different weight ratios. (a) LSF37-LSCF8291 after calcined at 800°C, (b) LSF37-LSCF8282 after calcined at 800°C, (c) LSF37-LSCF8291 after calcined at 900°C and (d) LSF37-LSCF8282 after calcined at 900°C 69
3.32 Temperature dependence of the specific conductivity (σ) for LSF-LSCF composites with different weight ratios. (a) LSF46-LSCF8291 after calcined at 800°C, (b) LSF46-LSCF8282 after calcined at 800°C, (c) LSF46-LSCF8291 after calcined at 900°C and (d) LSF46-LSCF8282 after calcined at 900°C 70
3.33 Weight ratios of LSCF dependence of the maximum specific conductivity for LSF37-LSCF8291 and LSF37-LSCF8282 composites. (a) calcined at 800°C and (b) calcined at 900°C 71
3.34 Weight ratios of LSCF dependence of the maximum specific conductivity for LSF46-LSCF8291 and LSF46-LSCF8282 composites. (a) calcined at 800°C and (b) calcined at 900°C 71

Figure **Page**

3.35 Arrhenius plot of the electrical conductivity of LSF-LSCF composites with different weight ratios. (a) LSF37-LSCF8291 after calcined at 800°C, (b) LSF37-LSCF8282 after calcined at 800°C, (c) LSF37-LSCF8291 after calcined at 900°C and (d) LSF37-LSCF8282 after calcined at 900°C 75

3.36 Arrhenius plot of the electrical conductivity of LSF-LSCF composites with different weight ratios. (a) LSF46-LSCF8291 after calcined at 800°C, (b) LSF46-LSCF8282 after calcined at 800°C, (c) LSF46-LSCF8291 after calcined at 900°C and (d) LSF46-LSCF8282 after calcined at 900°C 77

3.37 Temperature dependence of the specific conductivity (σ) for LSF-LSCF composites in a weight ratio of 1:3 after calcined at 800°C with different sintering temperatures for 10 hours. (a) LSF37-LSCF8291, (b) LSF37-LSCF8282, (c) LSF46-LSCF8291 and (d) LSF46-LSCF8282 79

3.38 Sintering temperature dependence of the maximum specific conductivity for LSF-LSCF composites in a weight ratio of 1:3 for 10 hours 80

3.39 Arrhenius plot of the electrical conductivity of LSF-LSCF composites in a weight ratio of 1:3 after calcined at 800°C with different sintering temperature for 10 hours. (a) LSF37-LSCF8291, (b) LSF37-LSCF8282, (c) LSF46-LSCF8291 and (d) LSF46-LSCF8282 81

3.40 Temperature dependence of the specific conductivity (σ) for LSF-LSCF composites in a weight ratio of 1:3 after calcined at 800°C with different sintering time for sintered at 1,300°C. (a) LSF37-LSCF8291, (b) LSF37-LSCF8282, (c) LSF46-LSCF8291 and (d) LSF46-LSCF8282 83

3.41 Sintering time dependence of the maximum specific conductivity for LSF-LSCF composites in a weight ratio of 1:3 for sintered at 1,300°C 84

3.42 Arrhenius plot of the electrical conductivity of LSF-LSCF composites in a weight ratio of 1:3 after calcined at 800°C with different sintering time for sintered at 1,300°C. (a) LSF37-LSCF8291, (b) LSF37-LSCF8282, (c) LSF46-LSCF8291 and (d) LSF46-LSCF8282 85

Figure **Page**

3.43 Temperature dependence of the thermal expansion for $La_{1-x}Sr_xFeO_{3-\delta}$ (x = 0.6 and 0.7) 88

3.44 Temperature dependence of the thermal expansion for $La_{0.8}Sr_{0.2}Co_{1-x}Fe_xO_{3-\delta}$ (x = 0.1 and 0.2) 90

3.45 Temperature dependence of the thermal expansion for LSF-LSCF composites in a weight ratio of 1:3 after calcined at 800°C and sintered at 1,300°C for 10 hours 91

LIST OF ABBREVIATIONS

LSF37	$La_{0.3}Sr_{0.7}FeO_{3-\delta}$
LSF46	$La_{0.4}Sr_{0.6}FeO_{3-\delta}$
LSCF8291	$La_{0.8}Sr_{0.2}Co_{0.9}Fe_{0.1}O_{3-\delta}$
LSCF8282	$La_{0.8}Sr_{0.2}Co_{0.8}Fe_{0.2}O_{3-\delta}$
LSF-LSCF	$La_{1-x}Sr_xFeO_{3-\delta}$ - $La_{0.8}Sr_{0.2}Co_{1-x}Fe_xO_{3-\delta}$
SOFC	Solid Oxide Fuel Cell
MIEC	Mixed Ionic Electronic Conductor
XRD	X-ray diffractrometry
SEM	Scanning Electron Microscopy
TEC	Thermal Expansion Coefficients
T	temperature
ºC	degree Celsius
K	Kelvin
k	kilo
%	percent
r_x	ionic radii of x
a,b,c	unit lattice parameter
ml	milliliter (s)
g	gram (s)
min	minute (s)
hrs	hour (s)
mg	milligram (s)
μm	micrometer (s)
Nm	nanometer (s)
mm	millimeter
cm	centimeter
Å	Angstrom
σ	Specific conductivity
t	tolerance factor

δ	oxygen non-stoichiometry
L	length
I	current
T	thickness
V	voltage
W	width
ρ	Specific resistance
R	the universal gas constant
F	the Faraday constant
Ω	Ohm

CHAPTER I

NTRODUCTION

At present, global demand of energy is increasing but petroleum fuels are limited. Moreover, it is related to increasing environmental problems such as global warming, air pollution and ozone depletion. The efficient and environmentally friendly production of energy is a goal for the development of energy technologies. Hence most researchers have tried to find a new energy resource such as fuel cell, biodiesel and gasohol. Furthermore, fuel cells are considered as a prime candidate for green energy production: clean, quiet, and efficient. Solid oxide fuel cells (SOFCs), one type of fuel cells, is hoped to find widespread application in the direct conversion of chemical energy into electricity with high thermodynamic efficiency and minimal environmental pollution.

1.1 Fuel cells

A fuel cell is an electrochemical device that converts the chemical energy in fuels (such as hydrogen, methane, butane or even gasoline and diesel) into electrical energy by exploiting the natural tendency of oxygen and hydrogen to react and giving much high conversion efficiency. The electricity produced is used to power an electric traction motor in a vehicle. In essence fuel cells are similar to batteries except that where batteries run down and become depleted, fuel cells are continually replenished with fuel and are able to provide a continuous supply of electric power.

Fuel cells are classified primarily by the kind of electrolyte they employ. This determines the kind of chemical reactions that take place in the cell, the kind of catalysts required, the temperature range in which the cell operates and the fuel required, as shown in Table 1.1.

Table 1.1 Types of fuel cells [1].

Fuel Cell type	**Electrolyte**	**Operating Temperature (°C)**	**Fuel**
Alkaline fuel cell (AFC)	Potassium hydroxide (KOH)	50-200	Pure hydrogen or hydrazine
Direct methanol fuel cell (DMFC)	Polymer	60-200	Liquid methanol
Phosphoric acid fuel cell (PAFC)	Phosphoric acid	160-210	Hydrogen from hydrocarbons and alcohol
Sulphuric acid fuel cell (SAFC)	Sulphuric acid	80-90	Alcohol or impure hydrogen
Proton-exchange membrane fuel cell (PEMFC)	Polymer, proton exchange membrane	50-80	Less pure hydrogen from hydrocarbons or methanol
Molten carbonate fuel cell (MCFC)	Molten salt such as nitrate, sulphate, carbonates	630-650	Hydrogen, carbon monoxide, natural gas, propane, marine diesel
Solid oxide fuel cell (SOFC)	Stabilised zirconia and doped perovskite	600-1000	Natural gas or propane
Solid polymer fuel cell (SPFC)	Solid sulphonated polystyrene	90	Hydrogen

Every fuel cell also has an electrolyte, which carries electrically charged particles from one electrode to the other, and a catalyst, which speeds the reactions at the electrodes.

1.2 Solid oxide fuel cells (SOFCs)

Solid oxide fuel cells are a class of fuel cell characterized by the use of a solid ceramic material as the electrolyte and operate at very high temperatures, typically between 500 and 1,000°C allowing a number of fuels to be used. At these temperatures, SOFCs do not require expensive platinum catalyst material, as is currently necessary for lower temperature fuel cells such as PEMFCs, and are not vulnerable to carbon monoxide catalyst poisoning. SOFCs have a wide variety of applications from use as auxiliary power units in vehicles to stationary power generation with outputs from 100 W to 2 MW. The SOFC has been in development since the late 1950s and has two configurations that are being investigate-planar (flat panel) and tubular, as shown in Figure 1.1.

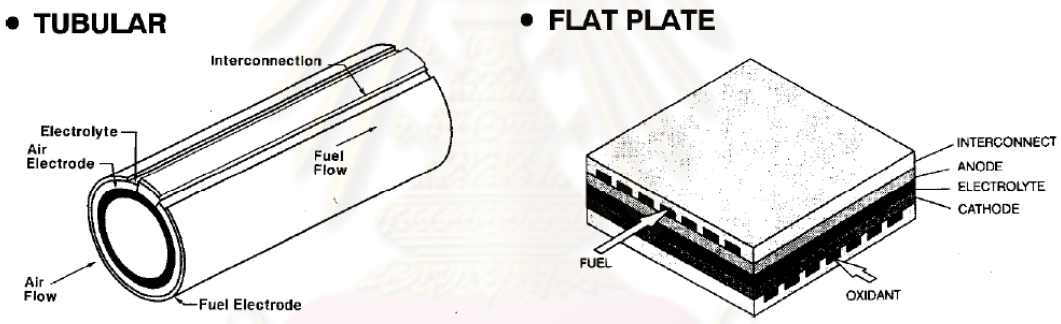

Figure 1.1 Tubular and flat-plates Solid oxide fuel cell [2].

Solid oxide fuel cells (SOFC) are promising candidates' for high efficiency energy production in the near future. Indeed, the advantages of SOFC are as consequence of

- SOFCs use one piece solid state ceramic cells, they are easier to maintain due to the lack of the corrosion.
- SOFCs can use many common hydrocarbon fuels such as natural gas, diesel, gasoline and alcohol.
- SOFCs have a potentially lower cost due the high operating temperature (500–1,000^{o}C), allowing the use of non-precious metal electrocatalysts, heat recovery and the superior ionic conductivity of the different components.
- High energy conversion efficiency.

- No emission of pollutant by CO.
- No moving parts and the cells therefore vibration-free, the noise pollution associated with power generation is also eliminated.
- SOFCs have a potential long life expectancy of more than 40,000-80,000 h.

The attraction of solid oxide fuel cells (SOFCs) is based on a number of aspects including the clean conversion of chemical energy to electricity, low levels of noise pollution, the ability to cope with different fuels, but most of all high efficiency. The enhanced efficiency of SOFC in comparison with other energy conversion systems is born out of its high operating temperature, which in some designs may exceed 1,000°C. In these cases the potential exists, by extracting the energy present in the high temperature exhaust gases - e.g. by using gas or steam turbines, to boost the overall efficiency of the SOFC system to about 70%.

1.2.1 Operation of solid oxide fuel cells

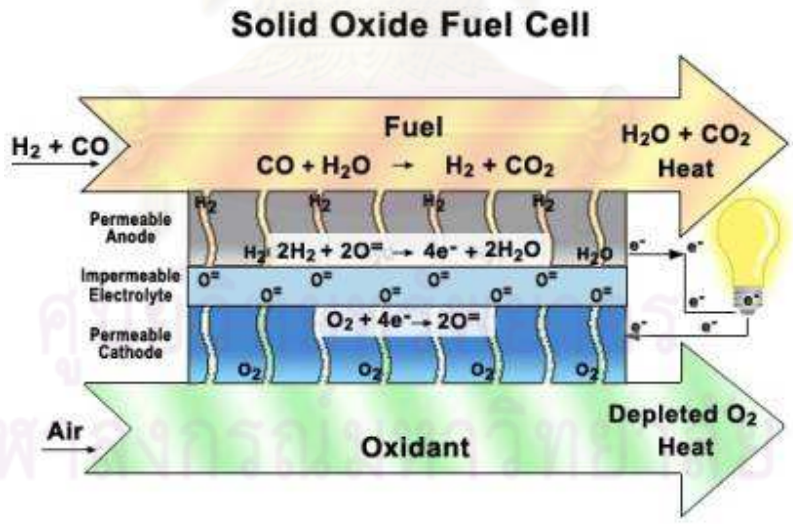

Figure 1.2 Operating concept of a SOFC [3].

Figure 1.2 shows schematically how a solid oxide fuel cell works. The cell is constructed with two porous electrodes which sandwich an electrolyte. Air flows along the cathode (which is therefore also called the "air electrode"). When an oxygen

molecule contacts the cathode/electrolyte interface, it catalytically acquires four electrons from the cathode and splits into two oxygen ions. The oxygen ions diffuse into the electrolyte material and migrate to the other side of the cell where they encounter the anode (also called the "fuel electrode"). The oxygen ions encounter the fuel at the anode/electrolyte interface and react catalytically, giving off water, carbon dioxide, heat, and most importantly electrons. The electrons transport through the anode to the external circuit and back to the cathode, providing a source of useful electrical energy in an external circuit.

When using hydrogen fuel, the electrochemical reactions of the SOFC:

Anode side:

$$H_2 + O^{2-} \longrightarrow H_2O + 2e^- \quad (1.1)$$

Cathode side:

$$½O_2 + 2e^- \longrightarrow O^{2-} \quad (1.2)$$

The overall cell reaction:

$$H_2 + ½O_2 \longrightarrow H_2O \quad (1.3)$$

When using carbon monoxide fuel, the electrochemical reactions of the SOFC:

Anode side:

$$CO + 2O_2{-} \rightarrow 2CO_2 + 4e^- \quad (1.4)$$

Cathode side:

$$O_2 + 4e^- \rightarrow 2O_2^- \quad (1.2)$$

The overall cell reaction:

$$CO + O_2 \rightarrow 2CO_2 \quad (1.5)$$

At high temperature, carbon monoxide can be oxidized with water to form carbon dioxide and hydrogen gas as the water–gas shift reaction

$$CO + H_2O \rightarrow CO_2 + H_2 \quad (1.6)$$

When using hydrocarbon ($C_nH_mO_p$) as fuels, the electrochemical reactions of the SOFC:

Anode side:

$$C_nH_m + (2n + 0.5m)O_2^- \rightarrow nCO_2 + (0.5m)H_2O + (4n + m)e^- ; p = 2n + 0.5m \quad (1.7)$$

Cathode side:

$$(n + 0.25m)O_2 + (4n + m)e^- \rightarrow (2n + 0.5m)O_2^- \quad (1.8)$$

The overall cell reaction:

$$C_nH_m + (n + 0.25m)O_2 \rightarrow nCO_2 + (0.5m)H_2O \quad (1.9)$$

The hydrocarbon-reforming reaction can be described as

$$C_nH_m + nH_2O \rightarrow (n + 0.5m)H_2 + nCO \quad (1.10)$$

1.2.2 Components of solid oxide fuel cells

Each component of the SOFC serves several functions and must therefore meet certain requirements such as [4].

(a) High chemical and structural stability to endure fabrication and operation at high temperatures.

(b) High conductivity

(c) Reactivity and interdiffusion between the components must be as low as possible

(d) The thermal expansion coefficients of the components must be as close to one another as possible in order to minimize thermal stresses which could lead to cracking and mechanical failure

(e) Porous anode and cathode to allow gas transport to the reaction sites

(f) High strength and toughness properties

(g) Low cost

1.2.2.1 Electrolyte

The electrolyte is a solid, nonporous ceramic, usually Y_2O_3-stabilized ZrO_2 (YSZ). The properties of materials used as electrolytes in SOFCs must be [5]:

(a) A good ionic conductor.

(b) Non-electron conductor.

(c) Good chemical compatability.

(d) Excellent mechanical properties.

(e) Thermal expansion that matches electrodes.

(f) Dense and leak tight.

(g) Thin to reduce ionic resistance.

(h) Economically processable.

1.2.2.2 Anode

The ceramic anode layer must be very porous to allow the fuel to flow towards the electrolyte. Like the cathode, it must conduct electrons, with ionic conductivity a definite asset. The most common material used is a cermet made up of nickel mixed with the ceramic material that is used for the electrolyte in that particular cell, typically YSZ (yttria stabilized zirconia). The anode is commonly the thickest and strongest layer in each individual cell, because it has the smallest polarization losses, and is often the layer that provides the mechanical support. Design requirements for the anode are [5]:

(a) High electronic conductivity

(b) High catalytic activity of Ni promotes cracking of hydrocarbon

(c) Stable in a reducing environment

(d) Thermal expansion coefficient similar neighboring cell component

(e) Chemically compatible with neighboring cell component

1.2.2.3 Cathode

The ceramic cathode layer must be porous, so that it allows air flow through it and into the electrolyte. Today the most commonly used cathode material are lanthanum strontium manganite, $LaSrMnO_3$ (LSM) and lanthanum calcium manganite, $LaCaMnO_3$ (LCM). The conductivity of these perovskites is all electronic (no ionic conductivity), a desirable feature since the electrons from the open circuit flow back through the cell via the cathode to reduce the oxygen molecules, forcing the oxygen ions through the electrolyte. In addition to being compatible with YSZ electrolytes and provide good performance at operating temperatures above 800°C. The cathode has to meet the following requirements [5]:

(a) High ionic-electronic conductivity

(b) High catalytic activity for oxygen molecule dissociation and oxygen reduction
(c) Chemically compatible with neighboring cell component
(d) Thermal expansion compatible with SOFC electrolyte

1.2.2.4 Interconnect

The interconnect can be either a metallic or ceramic layer that sits between each individual cell. Its purpose is to connect each cell in series, so that the electricity each cell generates can be combined. Because the interconnect is exposed to both the oxidizing and reducing side of the cell at high temperatures, it must be extremely stable. The requirements of the interconnection are the most severe of all cell components and include the following [5]:

(a) 100% electrical conductivity.
(b) No porosity (to avoid mixing of fuel and oxygen).
(c) Thermal expansion compatible with other fuel cell components.
(d) Inertness with respect to the other fuel cell components.
(e) Stability in both oxidizing and reducing atmospheres at the cell operating temperature since it is exposed to air (or oxygen) on one side and fuel on the other.

1.3 Perovskite [6]

Perovskite is an inorganic compound that the ideal structure is primitive cube. Perovskite (calcium titanium oxide, $CaTiO_3$) was discovered in the Ural mountains of Russia by G. Rose in 1839 and named for Russian mineralogist, L. A. Perovski (1792-1856). Under the high pressure conditions of the mantle, the pyroxene enstatite, $MgSiO_3$, is a perovskite polymorph and may be the most common mineral in the Earth. Perovskite is also the name of a more general group of crystals which take the same structure. There are many kinds of perovskites such as oxides, some carbides, nitrides, halides, and hydrides also crystallize in this structure. Perovskite exhibits both electronic and ionic conductivities (Mixed ionic electronic conductors; MIEC), making them promising candidate materials for solid oxide fuel cells.

1.3.1 Structure of perovskite oxides

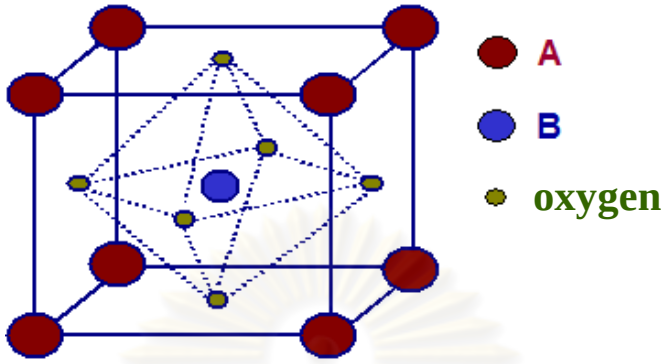

Figure 1.3 ABO_3 ideal perovskite structure.

The general chemical formula for perovskite oxides is ABO_3, where A is the larger cation (such as an alkaline earth cation) and B is the smaller cation (such as a transition metal cation). The ideal perovskite structure ABO_3 is primitive cubic, as shown in Figure 1.3. The ideal cubic-symmetry structure has the B cation in 6-fold coordination, surrounded by an octahedron of oxygen ions, and the A cation in 12-fold cuboctahedral coordination. The perovskite structures can be appropriately modified by partial substitution of A or B cations by other cations with different ionic radius or valence numbers.

The formation of perovskite-oxides with high oxygen ionic conductivity requires high oxygen vacancy concentrations created by dopants, and best conditions for oxygen mobility. The ionic radii of the dopants must be fitted to the lattice, This can be illustrated for the perovskite structure by deriving a relationship between the radii of the various ions. Figure 1.4 shows the relationship between ionic radii in the perovskite structure.

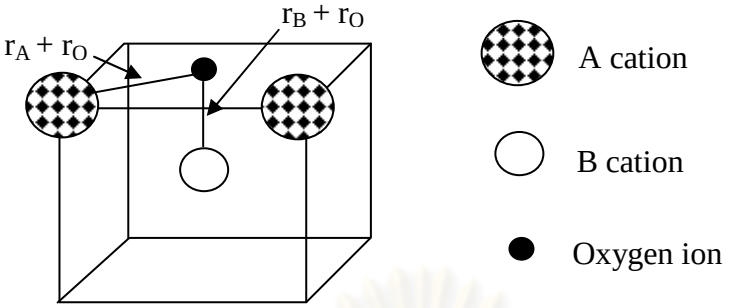

Figure 1.4 The relationship of ionic radii in perovskite structure.

$$a = 2\times(B-O) = 2(r_B + r_O) \tag{1.11}$$

and

$$a = \frac{1}{\sqrt{2}}\times 2\times(A-O) = \sqrt{2}(r_A + r_O) \tag{1.12}$$

hence,

$$2(r_B + r_O) = \sqrt{2}(r_A + r_O) \tag{1.13}$$

Where the atoms are touching one another, the B-O distance is equal to *a*/2 (*a* is the cubic unit cell parameter) while the A-O distance is $a/\sqrt{2}$ and the following relationship between the ionic radius holds shown in Equation 1.13. In general, the perovskite structure is formed if the tolerance factor, *t*.

$$t = \frac{(r_A + r_O)}{\sqrt{2}(r_B + r_O)} \tag{1.14}$$

The ideal perovskite is the cubic structure with the tolerance factor close to 1.0 at high temperature. The perovskite structure is stable in the range 0.75< t <1.0, and is cubic in the range t > 0.95. Deviations from the ideal structure are well known as orthorhombic, rhombohedral, tetragonal, monoclinic and triclinic symmetry. The distorted structure may exist at room temperature but it transforms to the cubic structure at ambient temperature.

1.3.2 Nonstoichiometry in perovskites [7]

Besides the ionic radii requirements, another condition to be fulfilled is electroneutrality, i.e., the sum of charges of A and B equals the total charge of oxygen

anions (such as form $A^{1+}B^{5+}O_3$, $A^{2+}B^{4+}O_3$ or $A^{3+}B^{3+}O_3$). In addition, partial substitution of A and B ions is allowed, thus yielding a plethora of compounds while preserving the perovskite structure. However, deficiencies of cations at the A- or B-sites or of oxygen anions are frequent which results in defective perovskites.

Oxygen vacancies are accomplished by substituting ions of similar size but different valence. Oxygen vacancies are more common than involving cationic vacancies. The former composition can be considered as an anion-deficient perovskite with one-sixth of the oxygen ions being vacant.

However, oxygen excess nonstoichiometry in perovskite oxides is not as common as anion-deficient nonstoichiometry probably because introduction of interstitial oxygen in perovskite structure is thermodynamically unfavorable. There are two reasons occur of oxygen excess nonstoichiometry. First, because the trivalent cation vacancies cause a large electronic imbalance and local lattice distortion, it does not stay close to each other. Second, with the formation of cation vacancies, a nonbonding O2p level is formed by the oxide ions around the vacancies. This nonbonding O2p level serves as the hole-trap. Applying this structure, nonstoichiometry of the oxygen-deficient composition was explained by the random distribution of oxide-ion vacancies. The general formula of oxygen-deficient perovskite oxides is $ABO_{3-\delta}$ or $ABO_{3+\delta}$.

1.3.3 Physical properties

The ABO_3 perovskites display several interesting physical properties such as ferroelectricity ($BaTiO_3$), ferromagnetism ($SrRuO_3$), weak ferromagnetism ($LaFeO_3$), superconductivity ($YBa_2Cu_3O_7$), large thermal conductivity due to exciton transport ($LaCoO_3$), insulator-to-metallic transitions of interest for thermistor applications ($LaCoO_3$), a fluorescence compatible with laser action ($LaAlO_3$: Nd), and transport properties of interest for high temperature thermoelectric power (La_2CuO_4).

1.3.3.1 Magnetic properties [7]

In the ideal cubic perovskite structure, each oxygen is shared by two B^{3+}ions, forming a B-O-B angle of 180°. Such a configuration is favorable for

superexchange interactions between magnetic B^{3+} cations. This exchange usually results in antiparallel coupling of nearest-neighbor magnetic moments. When the B^{3+}ions are in two sublattices ($A_2BB'O_6$) other spin arrangements are possible. If B′ is a diamagnetic ion, the B^{3+}ions are aligned antiferromagnetically, and the most important exchange mechanism is believed to be a longer range superexchange interaction through two oxygens of the type B-O-B′-O-B. The B-B separation is now considerably longer than the 0.4 nm separation found in the ideal perovskite. The $LnFeO_3$ (Ln=lanthanide) perovskites are those that have attracted the most attention because of their possible applications as technological magnetic materials. These compounds show a weak spontaneous magnetic moment, which is attributed to a slight canting of the iron moments, which are otherwise antiferromagnetically aligned. The iron moments align in such a way that the direction of easy magnetization is along the *a* or *c* axis of the orthorhombic cell. The weak ferromagnetic moment of 0.03-0.07μB/mol led to the materials being considered for memory devices. Similarly, $LnMnO_3$ shows very interesting magnetic properties. These manganites containing mostly Mn^{3+} or Mn^{4+} ions show antiferromagnetic behavior. However, ferromagnetic behavior is observed in the range from 25 to 35% Mn^{4+}. A weak magnetic interaction was found between Mn^{3+} ions, together with a negative interaction between Mn^{4+} ions and a strong positive interaction between Mn^{3+} and Mn^{4+}. A similar kind of behavior was found for the combination of Co^{3+} and Co^{4+}, but the Cr and Fe compounds were found to be antiferromagnetic.

1.3.3.2 Electrical properties [7]

The electrical conductivity of perovskites also shows wide variations. Several compounds have been used for their dielectric properties, while others show metallic conductivity, although most are semiconductors. As for other compounds, the electrical behavior in perovskites depends on the outermost electrons, which may be localized at specific atomic sites or may be collective. Since localized electrons may carry a spontaneous moment, there is a strong correlation between the electrical and magnetic properties of perovskites. Rare-earth perovskites containing transition ions

show widely differing electrical properties. The electrical properties of perovskites have aroused special interest since the discovery in 1986 of superconductivity at 40 K in cuprates. These cuprates are hole superconductors, exhibiting a mixed valence of copper Cu(II)-Cu(III). Among these, the exception is Ce doped Nd_2CuO_4, with T_c close to 25 K, which belongs to a different structural type and is an electron superconductor. All these compounds have a common feature, the bidimensional character of the structure, which has been shown to be an important factor for the existence of superconductivity at high temperature.

The electrical conductivity of perovskite was measured by using DC 4-probe or "Kelvin" measurement.

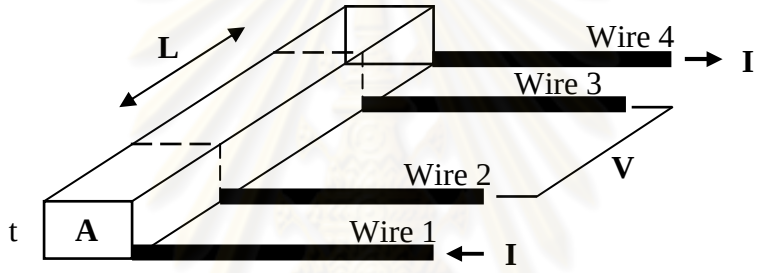

Figure 1.5 DC 4-probe method.

The measurement method then includes a forced current I through the outer wires 1 and 4 and a measurement of the voltage drop over wire 2 and 3, using a very high ohmic measurement device, so that the current flowing through wire 2 and 3 nearly zero. In that case the individual, additional contact resistance does not play a role as it cancels out of the equation. To study the behavior of the structure an I/V curve is generated, typically in the μA to the mA range. If the graph shows a straight line, the structure behaves as an Ohmic resistor. If assume that the resistance of a structure to be R then the following applies:

$$R = \frac{\rho L}{A} \tag{1.15}$$

With L = the length of the structure (m)

A = the area (width x thickness) of the cross section (m^2)

ρ = the specific resistivity (Ω.m of the practical unit μΩ.cm)

1.3.3.3 Mixed ionic-electronic conductors

The perovskite oxides exhibit both ionic and electronic conductivity. These oxides may show both high oxygen ion conductivity due to the high oxygen vacancy concentration, and a high electronic conductivity due to the mixed-valence state [8]. The B ions can take a mixed-valence state, charge neutrality is maintained by both the formations of oxygen vacancies and a change in the valence state of the B ions. The B-site ion substitution can increase the concentration of oxygen vacancies, such as Cu and Ni ions, which naturally take the divalent oxidation state [9]. If the valence state of the B ions is fixed, neutrality is maintained only by the formation of oxygen vacancies. The oxides may be predominantly ionic conductors, in this case.

In order to characterize the materials, it is more often to measure their electronic and ionic conductivity instead of concentrations of electrons (holes) and mobile ions (vacancies). The calculated ionic and electronic conductivity, which were separately, measured by using 4-probe ionic direct current and ordinary 4-probe direct current techniques, respectively.

In all materials that there are in principle nonzero electronic and ionic conductivity, the overall electrical conductivity σ_{tot} is the sum of electronic conductivity σ_e and ionic conductivity σ_i, as Equation (1.16),

$$\sigma_{tot} = \Sigma \sigma_{ij} + \sigma_e \qquad (1.16)$$

where σ_{ij} is the partial conductivity (in $\Omega^{-1}cm^{-1}$) of the *jth*-type ionic charge carriers presenting in the solid. Ionic charge carriers can be either atomic in nature or normally defects of either the anionic or cationic sublattice. Ionic conductivity occurs normally via interstitial sites or by hopping into a vacant site (vacancy motion) or a more complex combination based on interstitial and vacant sites. Electronic (electron/hole) conductivity occurs via delocalized states in the conduction-valence band or via localized states by a thermally assisted hopping mechanism. The presence of electronic conduction in perovskites proceeds via B.

Lattice cations through overlapping B-O-B bonds via a mechanism known as the Zerner double exchange process is shown in Equation (1.17) [10]:

$$B^{n+}\text{-}O^{2-}\text{-}B^{(n+1)} \longrightarrow B^{(n+1)+}\text{-}O^{2-}\text{-}B^{(n+1)+} \longrightarrow B^{(n+1)+}\text{-}O^{2-}\text{-}B^{n+} \quad (1.17)$$

This process is facilited by strong overlap of the B site cation and O_2^- orbital which is maximized for B-O-B angles at 180°C, i.e., cubic structure. In the orthorhombic structure, the tilting of BO_6 give rise to a decrease in the B-O-B overlap and thus would be expected to provide a larger barrier to electronic conduction. In the above double exchange mechanism, electronic conduction requires the presence of B site cations with multiple valences.

Furthermore, the electronic conduction can be n-type or p-type, depending on the material properties and ambient oxygen partial pressure. The energy level shifts from the center of the energy gap toward the empty zone for an n-type semiconductor or the filled band for a p-type semiconductor. An n-type conductor is an electron conductor while a p-type conductor is an electron hole conductor [11].

1.3.4 Oxygen permeation property [12]

Mixed-conducting oxides with high electron and oxygen ion conductivities (MIEC) are applied as ceramic membranes to separate oxygen from other gases by selective permeation. The very high O_2 separation factor is achieved by oxygen ion transport through the dense membrane at temperatures generally higher than 700 °C. The driving force is the oxygen partial pressure gradient over the membrane. At the high oxygen partial pressure side, the oxygen molecules adsorb on the membrane surface, dissociate into atoms which become ionized and migrate through the membrane to the low oxygen partial pressure side of the membrane. Finally, they release electrons forming oxygen atoms and molecules by recombination. In the opposite direction, the electrons move through the membrane thus ensuring local electrical neutrality. A schematic description of the dense perovskite type membrane is given in Fig.1.6

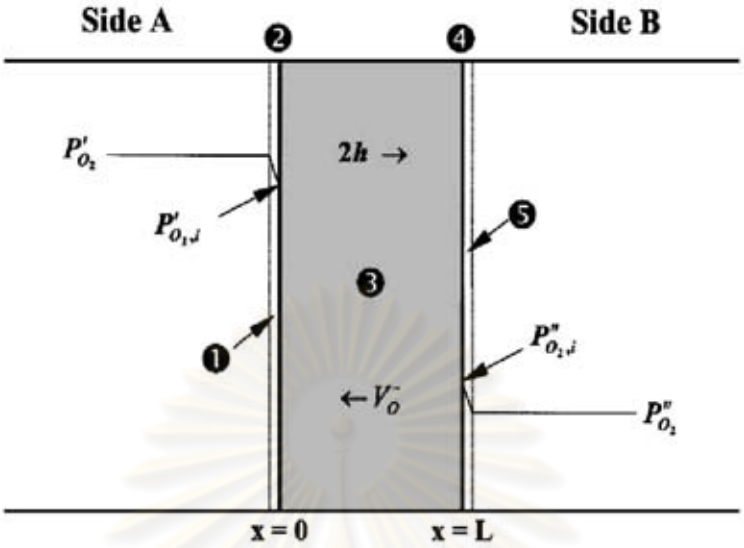

Figure 1.6 Oxygen transport through a perovskite type membrane.

In the above diagram, membrane is in the middle, and high and low oxygen pressure zones are, respectively, in the left and right sides of the membrane. The driving force for oxygen transport is the difference of oxygen partial pressures of both sides. High temperature provides the energy for the increasing motion of ions.

The theory of oxygen permeation through mixed-conducting materials has been described by the following relation into the case of a steady-state, diffusion-limited, with electronic conductivity much higher than ionic conductivity and one-dimensional oxygen transport. The simplified form of the Wagner equation which has been derived originally to describe the oxide film growth on metals [13] is as follows:

$$Jo_2 = \frac{RT}{(4F)^2}\frac{\sigma_{amb}}{L}\ln\frac{P'o_2}{P''o_2} \qquad (1.18)$$

Where $P''o_2$ and $P'o_2$ stand for the oxygen partial pressure in the higher and lower oxygen partial pressure compartment, respectively, L is the sample thickness, T is the temperature, R is the universal gas constant and F is the faraday constant. The ambipolar conductivity is defined as:

$$\sigma_{amb} = \frac{\sigma_e \sigma_i}{(\sigma_e + \sigma_i)} \qquad (1.19)$$

Where σ_e is the electronic contribution and σ_i is the ionic contribution to the total conductivity.

There is no need for an external current but the membrane must be a mixed conductor to allow the reverse flow of the electrons needed for the oxygen dissociation. The expected oxygen permeation flux in such membranes depends therefore on the difference of oxygen partial pressure between the two compartments, on the membrane thickness and on the ionic and electronic conductivity of the membrane.

1.3.5 Perovskite synthesis

The procedure for preparing perovskite type membranes consists of three steps: powder synthesis, shaping and sintering. Powder synthesis, as the first step, plays a critical role in determining the particle size of perovskite powder, and consequently has an influence on the microstructure of perovskite membrane. There are many routes to synthesize perovskite, such as a conventional solid–state reaction method and a wet chemical process that includes thermal decomposition of cyanide, metal–EDTA, chemical co precipitation and the sol-gel process etc.

1.3.5.1 Solid-state reaction

The most common procedure for perovskite oxides synthesis via solid state reactions is the calcination of a homogenous mixture of the corresponding metal-carbonates, hydroxides, oxides or salts. This is also known as ball milling and calcinations method. This method is very convenient but the impurities are introduced from raw materials, milling media, and the calcination container. Because of the high temperature required for the complete reaction. The problems such as multiphase have to be minimized in order to generate homogeneous high performance perovskite. For example, LSCF represents a typical case. Raw materials La_2O_3, $SrCO_3$, CoO_3, and Fe_2O_3 were mixed and ball-milled. After drying, then the mixed powders were calcined at 1,000°C to remove impurities and to achieve single-phase perovskite powder. The high temperature was required to complete reaction.

1.3.5.2 Sol-gel technique

The sol-gel process, also known as chemical solution deposition, is a wet-chemical technique widely used in the fields of materials science and ceramic engineering. Such methods are used primarily for the fabrication of materials (typically a metal oxide) starting from a chemical solution (or sol) that acts as the precursor for an integrated network (or gel) of either discrete particles or network polymers. Typical precursors are metal alkoxides and metal chlorides, which undergo various forms of hydrolysis and polycondensation reactions to form a colloid, a system composed of solid particles (size ranging from 1 nm to 1 μm) dispersed in a solvent. The sol evolves then towards the formation of an inorganic continuous network containing a liquid phase (gel). Formation of a metal oxide involves connecting the metal centers with oxo (M-O-M) or hydroxo (M-OH-M) bridges, therefore generating metal-oxo or metal-hydroxo polymers in solution. Sol-gel process involves producing precursor from citric acid and metal nitrate before thermal decomposition. For example, the production of Sr-substituted LaMnO3 perovskite powder by the amorphous citrate process, obtained the manganese citrate-nitrate precursor as shown in Equation 1.20 [14].

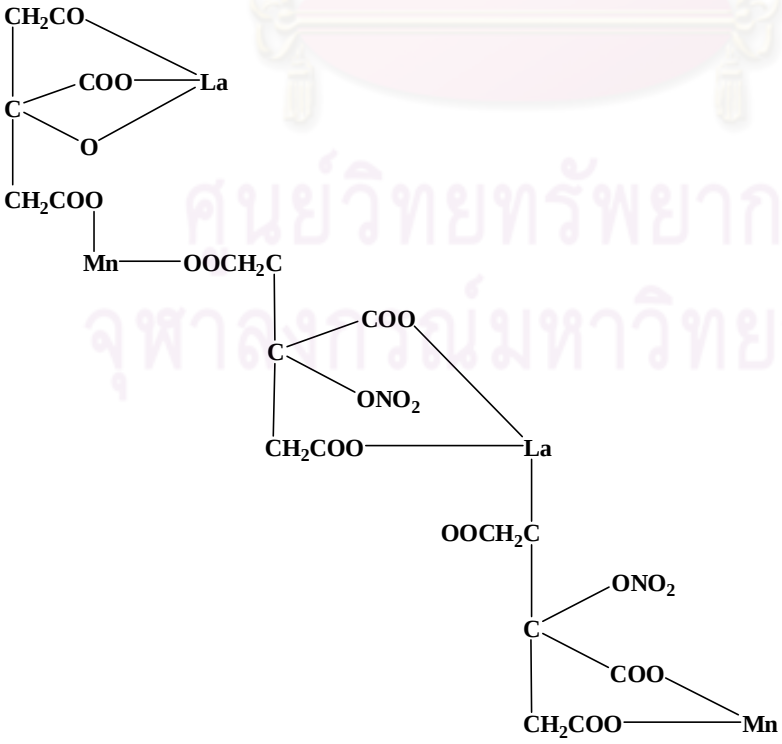

(1.20)

In the complex, the lanthanum is triply charged and replaces in normal citrate formation in the hydrogen of three -COOH groups and it replaces in the hydrogen of one -OH group and two -COOH groups. As manganese is divalent state replaces in the hydrogen of two -COOH groups while NO_2 replaces the hydrogen of one -OH group, respectively.

In all cases the minimum amount of citric acid used was that necessary to bond the metals if all the NO_3^- ions were replaced. However, the amounts of metal and citric acid should not less than equimolar. If the high amount of citric acid was used, Mn_2O_3 was presented from the complex as in Equation 1.21:

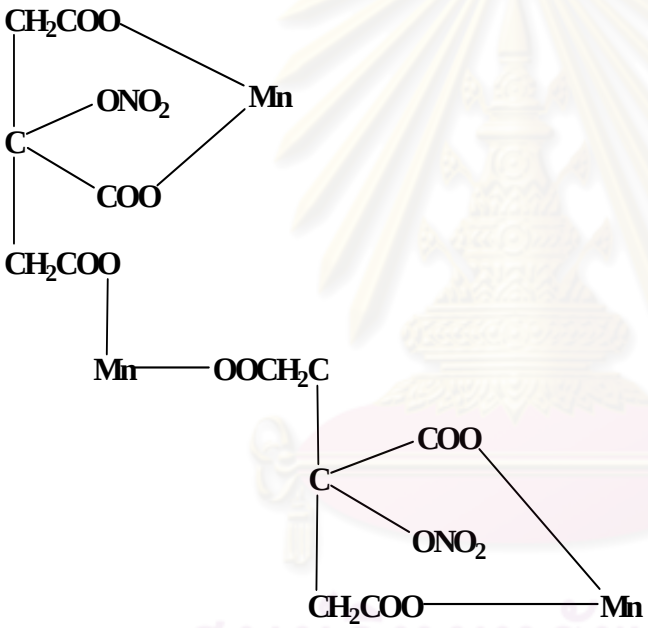

(1.21)

The formation of above structure would allow some citric acid, water, and nitrate ions to be lost during the preparation of gel. Every three molecules of citric originally present one remains uncombined and may be removed from the mixture by either evaporation or decomposition to yield acetone, carbon dioxide and water during the precursor preparation in the vacuum oven. The formation of this complex would also liberate NO_3^- groups for each two molecules of $Mn(NO_3)_2$ originally present in solution. The calcinations temperature should be higher than 800^oC because the wide range of homogeneity at lower temperatures was a result of the segregation of $Sr(NO_3)_2$ during precursor preparation and the production of $SrCO_3$ during precursor

decomposition. However, it should not be higher than 1,100^{o}C because these would inevitably lead to a decrease in surface area. They also reported that the best compromise would appear and initial treatment of the precursor at 700^{o}C to yield the high surface area followed by an increase in temperature to 1,100^{o}C for a period of up to 4 hours to remove carbon.

The drying process serves to remove the liquid phase from the gel thus forming a porous material, then a thermal treatment (firing) may be performed in order to favor further polycondensation and enhance mechanical properties [15].

1.3.5.3 Co-precipitation

One of the oldest techniques comprised of mixing an aqueous solution containing the desired cations and another solution acting as a precipitation agent. Filtration, drying and thermal decomposition followed to acquire desired products. The desired products and their physical properties are adjusted using pH, mixing rates, temperatures and concentration. Usually, the morphology, purity and composition control achieved is good, although different precipitation rates sometimes result in inhomogeneities. A doping agent may be added to assist in reaching the compositional homogeneity. A careful control of pH and precipitation temperature is substantial to obtain material with an exact stoichiometric condition. After coprecipitation the resulting powders undergo intermediate high-temperature calcination to decompose the salts and produce fine crystallites of the desired oxides [16].

1.3.5.4 Hydrothermal synthesis

Hydrothermal synthesis is a widely used technique for the preparation of fine particles. It can be carried out in batch or flow systems, although most studies have used batch reactors below 200^{o}C. More recently, however, continuous hydrothermal synthesis has been employed in near- and supercritical water to obtain metal oxide particles. This technique offers tremendous promise for control of particle characteristics due to the rapidly changing properties of water with temperature and pressure in the critical region [17]. This synthesis method can be defined as a method

of synthesis of single crystals which depends on the solubility of minerals in hot water under high pressure. The crystal growth is performed in an apparatus consisting of a steel pressure vessel called autoclave, in which a nutrient is supplied along with water. A gradient of temperature is maintained at the opposite ends of the growth chamber so that the hotter end dissolves the nutrient and the cooler end causes seeds to take additional growth.

Possible advantages of the hydrothermal method over other types of crystal growth include the ability to create crystalline phases which are not stable at the melting point. Also, materials which have a high vapour pressure near their melting points can also be grown by the hydrothermal method. The method is also particularly suitable for the growth of large good-quality crystals while maintaining good control over their composition. Disadvantages of the method include the need of expensive autoclaves, and the impossibility of observing the crystal as it grows [18].

1.3.5.5 Spray and freeze drying

Freeze-drying, another route to homogenous and reactive precursor powders, a mixture of water-soluble salts is dissolved in water. Small droplets are then rapidly frozen by spraying the solution into a chilled organic liquid such as hexane. With rapid freezing of the spray droplets into small ice crystals, segregation of the chemical constituents is minimized. The frozen material is removed from the hexane by sieving, and water is then removed from the ice by sublimation under vacuum [16]. Excellent impurity and composition control is inherent, leading to homogeneous fine materials. In addition, spray drying is an industrially established process and the manufacture of complex multi-metallic oxides can be scaled up easily.

1.3.6 Calcination [19]

Calcination (also referred to as calcining) is a thermal treatment process applied to ores and other solid materials in order to bring about a thermal decomposition, phase transition, or removal of a volatile fraction but without fusion. The calcination process normally takes place at temperatures below the melting point of the product materials. The objects of calcination are usually: (1) to drive off water,

present as absorbed moisture, as water of crystallization, or as water of constitution; (2) to drive off carbon dioxide, sulfurdioxide, or other volatile constituent; (3) to oxidize a part or the whole of the substance. There are a few other purposes for which calcination is employed in special cases, and these will be mentioned in their propel' places. The process is often called roasting, firing, or burning by the workmen.

1.3.7 Sintering [20, 21]

Sintering is a method for making objects from powder, by heating the material in a sintering furnace below its melting point (solid state sintering) until its particles adhere to each other. The fusing of particles results in an increase in the density of the part and hence the process is sometimes called densification. The driving force of sintering process is reduction of surface energy of the particles caused by decreasing their vapour-solid interfaces. When a powder aggregate is sintered, necks form between the particles, and the aggregate may increase in density. The growth of the neck is due to the transport of matter or of the counter-flow of vacancies between the particles and the pores. In crystalline powder, its transport occurs by diffusion (bulk, surface or grain boundary diffusion), whereas in amorphous materials, it occurs by viscous flow. Kuczynski has defined the neck growth as in Equation 1.22

$$X^n/r^m = \text{kt} \qquad (1.22)$$

Where X and r are defined in Figure 1.7, t is the time, k is the temperature dependent constant, n and m are constants dependent on the mechanisms of growth, viscous or bulk diffusion, surface diffusion, or evaporation and condensation.

The sintering process can be distinguished by three stages. The early stage or initial stage during which the necks form at points of particle contact and the particles usually center approach each other. At this stage the individual particles are still distinguishable. The intermediate stage during that the necks become large, resulting in the formation of an interconnected pore structure. The third or the final stage during, the pores become isolated. Elimination of the interconnectivity of pores eliminates surface and vapor transport.

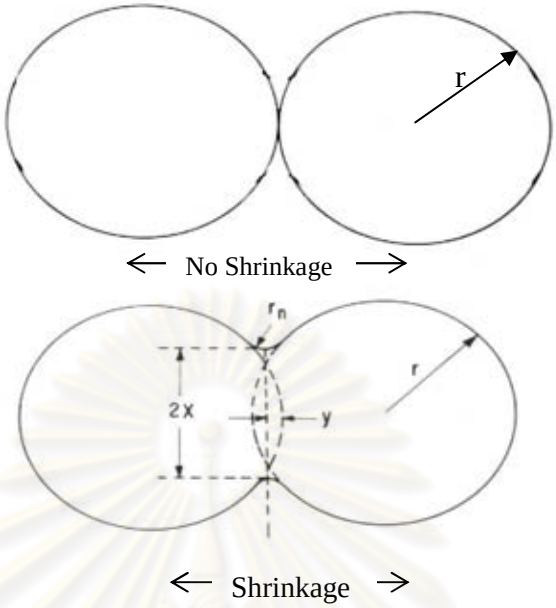

Figure 1.7 Mechanism of sintering; *X* is the internal radius of the neck; *r* is the particle radius.

Closed pores isolated from grain boundaries shrink very slowly because grain boundary diffusion is far away from the pores. The growth of grains, therefore, hinders the attainment of theoretical density, since the pore's growth is also enhanced. It is essential, therefore, to retard grain growth so that densification of the compact can continue to the theoretical limit. This is particularly important with the present trend for the fabrication of technical ceramics. Surface diffusion becomes important in the case of very fine particles. Grain boundary diffusion and volume diffusion are the main mechanisms causing shrinkage of the neck, whereas surface diffusion does not contribute to any shrinkage. The most important diffusion paths during the sintering of two spheres with a grain boundary are surface diffusion, grain boundary diffusion, volume diffusion from the grain boundary to the neck surface, and volume diffusion from the sphere surface to the neck surface. The sintering rate also affected by the crystallization and growth processes, which occur concurrently. The sintering rate is reduced when there is intensive grain growth because when diffusion forms the pores occurs toward the boundaries of individual grains, the distance over which diffusion occurs with a reduction in pores is determined by the size of the crystals.

1.4 Literature reviews

In 2002, Gopalan et al. [22] investigated the effect of the time of sintering on the electrical conductivity of Li_2SO_4-Al_2O_3 composites. It was found that the electrical conductivity of composite increased with increasing the sintering time but the electrical conductivity decreased with increasing the sintering temperature. The composite containing 50% Al_2O_3 has maximum conductivity, about three order of magnitude higher than that of pure Li_2SO_4. The value of the conductivity for this composition are 1.76×10^{-2} and 6×10^{-5} $\Omega^{-1}cm^{-1}$ at 500 and 200°C, respectively.

In 2003, Shiratori et al. [23] prepared yttria-stabilized zirconia (YSZ)-MgO composite electrolyte materials with the aim to decrease the TEC mismatch with other SOFC components. The composite electrolytes were prepared by mixing partially stabilized zirconia with various amounts of magnesium oxide and firing at 1,400°C for 5 hours. The thermal expansion increased with increasing MgO content and a thermal expansion coefficient (TEC) of 12.3×10^{-6} K^{-1} was obtained with 80 mol% MgO in the starting mixture, the TEC value of the composite electrolyte agrees with that of the Ni/YSZ cermet anode. However, at this MgO content, the electrical conductivity is decreased and one order of magnitude lower than the conductivity of 8 mol% yttria-stabilized zirconia (8YSZ). The composite with 60 mol% MgO is an attractive material for further development because the composite material has rather low TEC value of 11.6×10^{-6} K^{-1} and acceptable conductivity.

In 2004, Dyck et al. [24] examined the thermal expansion match of the $Gd_{1-x}Sr_xCoO_{3-\delta}$ system to the $Ce_{0.8}Gd_{0.2}O_{1.95}$ IT-SOFC electrolyte material for x = 0 to 0.5. The optimum composition in the $Gd_{1-x}Sr_xCoO_{3-\delta}$ system was found to be $Gd_{0.8}Sr_{0.2}CoO_{3-\delta}$ as a result of its high electrical conductivity (400 Scm^{-1} at 600°C), linear thermal expansion response with temperature, and high mechanical stability. The thermal expansion mismatch for all $Gd_{1-x}Sr_xCoO_{3-\delta}$ compositions with the $Ce_{0.8}Gd_{0.2}O_{1.95}$ electrolyte was shown to be high. The formation of composite $Gd_{0.8}Sr_{0.2}CoO_{3-\delta}$/$Ce_{0.8}Gd_{0.2}O_{1.95}$ cathodes solved the thermal mismatch problem. High electrical conductivity values on the order of 115 and 60 Scm^{-1} were maintained for $Ce_{0.8}Gd_{0.2}O_{1.95}$ additions of 12.5 and 25 wt%, respectively. High electrical conductivity was maintained for compositions with excellent thermal expansion matching to the IT-SOFC electrolyte material $Ce_{0.8}Gd_{0.2}O_{1.95}$.

Huang et al. [25] studied composites of yttria-stabilized zirconia (YSZ) with Sr-doped $LaFeO_3$ (LSF) for application as high-performance cathodes for solid oxide fuel cells (SOFCs). The composites were formed by aqueous impregnation of porous YSZ with La, Sr and Fe salts, followed by calcination at various temperatures. X-ray diffraction measurements showed that the LSF perovskite phase had formed by 1,023 K and that solid-state reaction with the YSZ did not occur below approximately 1,223 K. The electronic conductivity of the 40 wt% LSF-YSZ composite was maximized by calcination at 1,123 K. SOFCs prepared with a 40 wt% LSF-YSZ cathode showed improved performance over SOFCs prepared with conventional LSM-YSZ cathodes at 973 K, although the performance of cells made with cathodes having lower LSF content did not perform as well.

In 2005, Pelosato et al. [26] studied composites of $(1\text{-}x)La_{0.83}Sr_{0.17}Ga_{0.83}Mg_{0.17}O_{2.83}$ (LSGM) – $xLa_{0.8}Sr_{0.2}MnO_3$ (LSM) (x = 0, 0.01, 0.05, 0.25, 0.50, 0.75 and 1). Composites have been sintered at 1,300°C in air for 2 hours, and their relative densities vary in the range 89–85%. The total conductivity was about 2×10^{-2} Scm^{-1} at 800°C for samples with 1% and 5% LSM; such low conductivity is consistent with the values found in the literature for pure LSGM sintered at 1,400°C and may account for the low relative densities. The presence of large quantity of LSM induces high electronic conductivity and these composites could be suitable as electrode cathodic material in IT-SOFC.

In 2007, Zhou et al. [27] prepared $Ba_{0.5}Sr_{0.5}Co_{0.8}Fe_{0.2}O_{3-\delta}$ + $LaCoO_3$ (BSCF + LC) composite as a cathode for intermediate-temperature solid-oxide fuel cells based on a $Sm_{0.2}Ce_{0.8}O_{1.9}$ (SDC) electrolyte. The LC oxide was added to BSCF cathode in order to improve its electrical conductivity. X-ray diffraction examination demonstrated that the solid-state reaction between LC and BSCF phases occurred at temperatures above 950°C and formed the final product with the composition: $La_{0.316}Ba_{0.342}Sr_{0.342}Co_{0.863}Fe_{0.137}O_{3-\delta}$ at 1,100°C with a lattice parameter of 3.789 °A. The electrical conductivity of the BSCF + LC composite oxide increased with increasing calcination temperature, and reached a maximum value of about 300 Scm^{-1} at a calcination temperature of 1,050°C, while the electrical conductivity of the pure BSCF was only about 40 Scm^{-1}. The improved conductivity resulted in attractive cathode performance. Peak power densities as high as about 700 $mWcm^{-2}$ at 650°C

and about 525 $mWcm^{-2}$ at 600°C were reached for the thin-film fuel cells with the optimized cathode composition and calcination temperatures.

In 2008, Xu et al. [28] investigated the structure, electrical conducting and thermal expansion properties of $La_{0.6}Sr_{0.4}Co_{0.8}Fe_{0.2}O_{3-\delta}$ - $Ce_{0.8}Sm_{0.2}O_{2-\delta}$ composite cathodes with respect to the fraction of $Ce_{0.8}Sm_{0.2}O_{2-\delta}$ electrolyte. No chemical reaction product between the two constituents was detected for the composite cathodes sintered at 1,200°C for 4 hours. A dense microstructure composing of homogeneously distributed constituent phases was observed. It was found that the electrical conducting and thermal expansion properties of the composite cathodes are sensitive to the fraction of $Ce_{0.8}Sm_{0.2}O_{2-\delta}$ electrolyte. In terms of both electrical conducting and thermal expansion properties, the composite cathode containing 50 wt% $Ce_{0.8}Sm_{0.2}O_{2-\delta}$ electrolyte was ascertained to be the optimum composition. This composition offers sufficiently high electrical conductivities of 100–116 $\Omega^{-1}cm^{-1}$ at intermediate temperatures (600–800°C) and a moderate thermal expansion coefficient of 14.4 x 10^{-6} K^{-1} averaged between 100 and 730°C.

Zhu et al. [29] studied $Ba_{0.5}Sr_{0.5}Co_{0.8}Fe_{0.2}O_{3-\delta}$–$xSm_{0.5}Sr_{0.5}CoO_{3-\delta}$ (BSCF–xSSC, x = 0–40 wt%) composite cathodes supported on $Sm_{0.2}Ce_{0.8}O_{1.9}$ (SDC) electrolyte for applications in IT-SOFCs. X-ray diffraction patterns showed obvious solid-state reactions between BSCF and SSC. However, the composite materials exhibited higher conductivity than that of pure BSCF, e.g., around 176 Scm^{-1} at 500°C for the x = 30 wt% composite, which was nearly seven times higher than that of BSCF. The thermal expansion coefficients of the BSCF–SSC were between (18.0 and 21.9) x 10^{-6} K^{-1} from 30 to 800°C, which was slightly higher than that of BSCF. In addition, electrochemical impedance spectra exhibited the better performance of BSCF–SSC composite cathodes than pure BSCF. The results of the polarization resistance indicated that the optimum content of SSC in the composite cathodes was about 30 wt%, e.g., the polarization resistance value of BSCF–30 wt% SSC was only 0.71 Ωcm^2 at 550°C, about one seventh of that BSCF at 550°C, which indicated that the composite BSCF–30SSC could be a potential candidate for IT-SOFCs cathode materials.

In 2010, Zhou et al. [30] prepared SSC (70 wt% $SrSc_{0.2}Co_{0.8}O_{3-\delta}$)-SDC (30 wt% $Sm_{0.2}Ce_{0.8}O_{1.9}$) composite cathode in various sintering temperature (950-

1,100^{o}C). The chemical interaction between SSC and SDC was characterized by oxygen-temperature programmed desorption (O_2-TPD) technique. The conductivity of the composite was measured by a four-probe direct current technique. As a result, the phase reaction likely occurred by the incorporation of cerium and samarium from SDC into both the A-site and B-site of SSC. The phase reaction increased the reducibility of the cobalt ions. The newly formed phase had a higher electrical conductivity than the calculated values for the composite of the reactants, SSC and SDC, without phase reaction. The derived electrical conductivity of the composite was only slightly lower than that of SSC. Due to lower ionic conductivity and electronic conductivity of SDC as compared to SSC, a lower electrode performance was observed for the SSC+SDC composite than for the pure SSC electrode. The increase in firing temperature resulted in a lower electrode surface area and in a higher degree of the phase reaction between SSC and SDC. The SSC+SDC electrode fired at 950^{o}C showed the best performance.

Zhang et al. [31] studied $La_{0.7}Ca_{0.3}CrO_3$ (LCC)–$Ce_{0.8}Gd_{0.2}O_{1.9}$ (GDC) composites as symmetrical electrodes for solid-oxide fuel cells (SOFCs) on $La_{0.9}Sr_{0.1}Ga_{0.8}Mg_{0.2}O_{3-\delta}$ (LSGM) electrolyte, where there is no interlayer between anode and electrolyte. LCC oxide is chemically compatible with GDC and LSGM electrolyte at temperatures up to 1,200^{o}C. The TECs of the LCC–GDC composites increased from 10.1 x 10^{-6} K^{-1} to 10.8 x 10^{-6} K^{-1} on increasing the GDC content from 20% to 40%, showing thermal compatibility with the LSGM electrolyte in the temperature range 30–1,000^{o}C. The LCC doped with 20% of GDC (LCC–GDC20) sample displayed the highest electrical conductivities of 18.64 Scm^{-1} in air and 1.86 Scm^{-1} in H_2 at 850^{o}C. Cell performances with the symmetrical electrodes decreased with increasing GDC content due to the decrease in conductivity. The maximum power densities attained with the LCC–GDC/LSGM/LCC–GDC symmetrical cells were 573, 481, and 476 $mWcm^{-2}$ at 900^{o}C in H_2 fuel with GDC contents of 20%, 30%, and 40%, respectively. No obvious carbon deposition and sulfur poisoning were observed in city gas over a period of 20 hours. The LCC–GDC20 composite showed high electrical conductivity, good thermal expansion compatibility with LSGM electrolyte, and pertinent electrochemical performance, hence it is recommended as a promising symmetrical electrode material for use in SOFCs.

Ortiz-Vitoriano et al. [32] prepared $La_{0.6}Ca_{0.4}Fe_{0.8}Ni_{0.2}O_3$ (LCFN) – $Ce_{0.8}Sm_{0.2}O_2$ (SDC) composite cathodes with different mass content of SDC. The best electrochemical performance is for LCFN cathode doped with 10% of SDC (LCFN–SDC9010), exhibiting an ASR value of 0.13 Ωcm^2 at 850 °C. The electrical conductivity of LCFN–SDC9010 composite at temperatures above 600 °C is over 100 Scm^{-1}. These results suggest that the LCFN and SDC composites are promising cathode materials for intermediate-temperature-operation solid oxide fuel cells (IT-SOFC) applications.

Recently, many researchers are looking for new cathode materials for intermediate temperature solid oxide fuel cell (IT-SOFC). $La_{1-x}Sr_xCo_{1-y}Fe_yO_{3-\delta}$ is a good candidate for cathode material for IT-SOFC because of their superior mixed electronic ionic conducting properties. However, $La_{1-x}Sr_xCo_{1-y}Fe_yO_{3-\delta}$ exhibits a high thermal expansion coefficient (TEC) value, resulting in a difficulty in matching with other SOFC components such as solid state electrolyte. Numerous research efforts have been devoted in solving the problem by means of adjusting the content of acceptor dopant Sr at the A site and/or Co/Fe ratio at B site [33, 34]. Unfortunately, lowering TEC is usually coupled with a decrease of electrical conducting property. Thus, it is difficult to attain a compromise between acceptable thermal expansion behavior and high electrical conducting property. On the other hand LSF perovskite oxide exhibit lower thermal expansion and electrical conducting properties. Therefore, this research is focused to minimize the TEC mismatch problem by adding $La_{1-x}Sr_xFeO_{3-\delta}$ into $La_{1-x}Sr_xCo_{1-y}Fe_yO_{3-\delta}$ for making composite.

1.5 The objectives of the thesis

The objectives of this study are as follows:

1. To synthesize composite perovskite of $La_{1-x}Sr_xFeO_{3-\delta}$ (x=0.6 and 0.7)-$La_{0.8}Sr_{0.2}Co_{1-x}Fe_xO_{3-\delta}$ (x=0.1 and 0.2) in various weight ratios, calcined temperature, sintering temperature and time.
2. To study the properties of synthesized composite perovskite oxides in order to evaluate their potential as cathode materials for SOFC.

CHAPTER II

EXPERIMENTAL

The chemicals, apparatus and experimental procedures including processing of perovskite powders synthesis, perovskite disc preparation and characterization of materials, are described as below:

2.1 Chemicals

The chemicals listed in Table 2.1, were used without further purification.

Table 2.1 Reagents for synthesis of perovskites

Reagents	Formula Weight	Purity%	Company
$La(NO_3)_3 \cdot 6H_2O$	433.02	≥ 99.0	Fluka
$Sr(NO_3)_2$	211.63	≥ 99.0	Fluka
$Fe(NO_3)_3 \cdot 9H_2O$	404.00	98	Fluka
$Co(NO_3)_2 \cdot 6H_2O$	291.03	98.0	Fluka
$C_6H_8O_7$	192.43	99.5	Riedel-deHaën
$NH_3 \cdot H_2O$	35.05	25	Merck
C_2H_5OH	46.07	30	Merck

2.2 Synthesis of perovskite powder

2.2.1 $La_{0.3}Sr_{0.7}FeO_{3-\delta}$ (LSF37) and $La_{0.4}Sr_{0.6}FeO_{3-\delta}$ (LSF46)

The perovskite powders $La_{0.3}Sr_{0.7}FeO_{3-\delta}$ (LSF37) and $La_{0.4}Sr_{0.6}FeO_{3-\delta}$ (LSF46) were synthesized in basic solution. $La(NO_3)_3 \cdot 6H_2O$, $Sr(NO_3)_2$ and $Fe(NO_3)_3 \cdot 9H_2O$, were used as raw materials. Stoichiometric amounts of corresponding high purity metal nitrates (based on 3 g. of perovskite powder) were partially dissolved in 15 ml D.I. water, and citric acid was added with 2 times of total metal ions. The above

solution was mixed at room temperature under constant stirring for 3 hours. The mixture solution was then titrated with 25% ammonia solution at the controlled rate of 2-3 ml/min. The pH of the solution was adjusted to ~9 and the solution was allowed to stir at room temperature for 2 hours. The homogenous clear solution (in a 2,500 ml beaker covered with a fine sieve) was heated and stirred on a hot plate at around 200-300°C until the dried gel was obtained. Then the self combustion was initiated and the mixture was burned instantaneously and transformed into black powder. The as-burned loose powders were ground by mortar and pestle, subsequently the synthesized perovskite oxide was calcined in a furnace in air to achieve phase purity and eliminate the residual organic compound.

The conditions used for the calcination of the perovskite powders were set as follows:

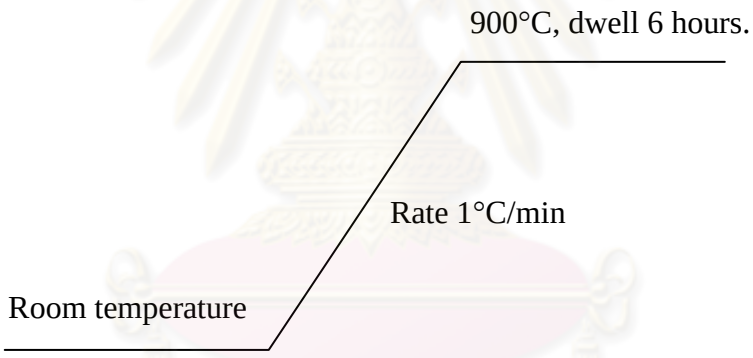

Figure 2.1 The condition of calcination for LSF.

2.2.2 $La_{0.8}Sr_{0.2}Co_{0.8}Fe_{0.2}O_{3-\delta}$ (LSCF8282) and $La_{0.8}Sr_{0.2}Co_{0.9}Fe_{0.1}O_{3-\delta}$ (LSCF8291)

The perovskite powders $La_{0.8}Sr_{0.2}Co_{0.8}Fe_{0.2}O_{3-\delta}$ (LSCF8282) and $La_{0.8}Sr_{0.2}Co_{0.9}Fe_{0.1}O_{3-\delta}$ (LSCF8291) were synthesized in basic solution. $La(NO_3)_3 \cdot 6H_2O$, $Sr(NO_3)_2$, $Co(NO_3)_2.6H_2O$ and $Fe(NO_3)_3 \cdot 9H_2O$, were used as raw materials. Stoichiometric amounts of corresponding high purity metal nitrates (based on 3 g. of perovskite powder) were partially dissolved in 10 ml D.I. water, and citric acid was added with 1.2 times of total metal ions. The above solution was mixed at room temperature under constant stirring for 24 hours, and then heated at 96-100°C

for 3.5 hours. The solution changed from partially dissolved dark red solution to dark red gel**.**

The combustion of the homogeneous solution was carried out on a hot plate at around 200^{o}C in a three-liter beaker covered with a fine sieve to prevent the loss of fine powders. The water was evaporated until a sticky gel was obtained. Then it became a large swelling viscous mass and finally self ignited by nitrate compound. The combustion lasted for about 10-20 seconds. The resulting powder was ground by mortar and pestle, subsequently the synthesized perovskite oxide was calcined in a furnace in air.

The conditions used for the calcination of the perovskite powders were set as follows:

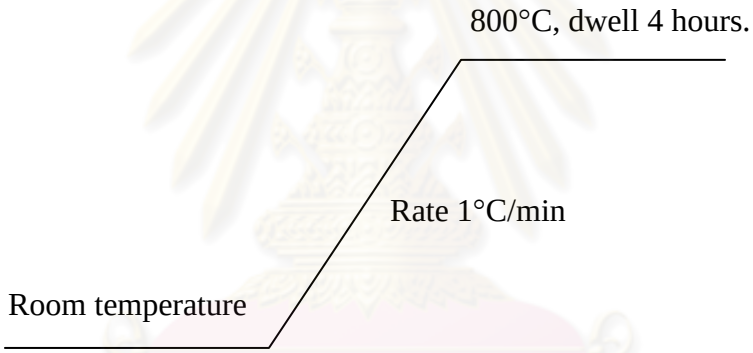

Figure 2.2 The condition of calcination for LSCF.

2.3 Preparation of composite perovskite powder by physical method

The composite perovskite powders LSF37-LSCF8291, LSF37-LSCF8282, LSF46-LSCF8291 and LSF46-LSCF8282 were prepared by physical mixing method with various weight ratios**;** LSF:LSCF = 3:1, 2:1, 1:1, 1:2 and 1:3. Mixture powders were calcined in a furnace in air at 800-1,000^{o}C for 10 hours.

The conditions used for the calcination of the composite perovskite powders were set as follows:

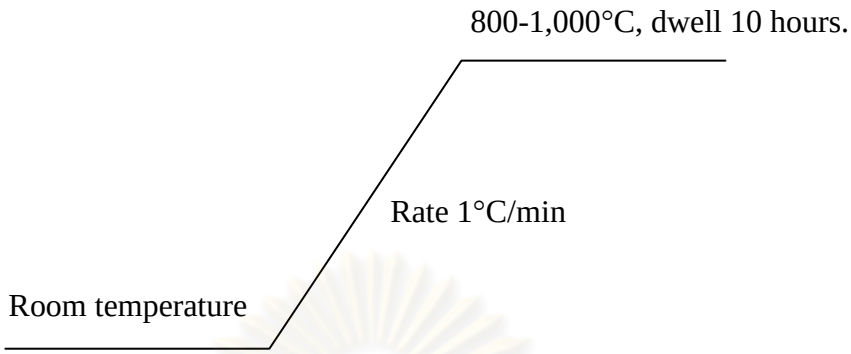

Figure 2.3 The condition of calcination for LSF-LSCF.

2.4 Perovskite disc preparation

The shape-forming process of perovskite powders was performed by using a KBr die.

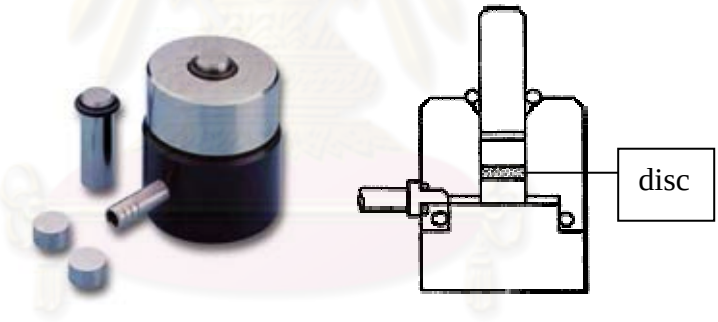

Figure 2.4 KBr die.

The calcined perovskite powders were ground with ethanol by mortar for three times. The fine perovskite powders about 1.8 g. were loaded into the cavity of die. The plunger was brought to the surface of the powder gently and then rotates for smooth surface.

The pressure was slowly applied about 2-2.5 tons on the plunger of the die by the uniaxial pressing machine. The pressure was released and the die was removed from the pressing machine after 10-15 minutes. The disc is around 1 mm thick, 13 mm diameter were stripped from the die and plunger. Then the discs were generally sintered in air.

2.5 The sintering of the perovskite oxides

The perovskite discs were generally sintered in air under different conditions, depending on the composition. The conditions used for sintering were set as follows:

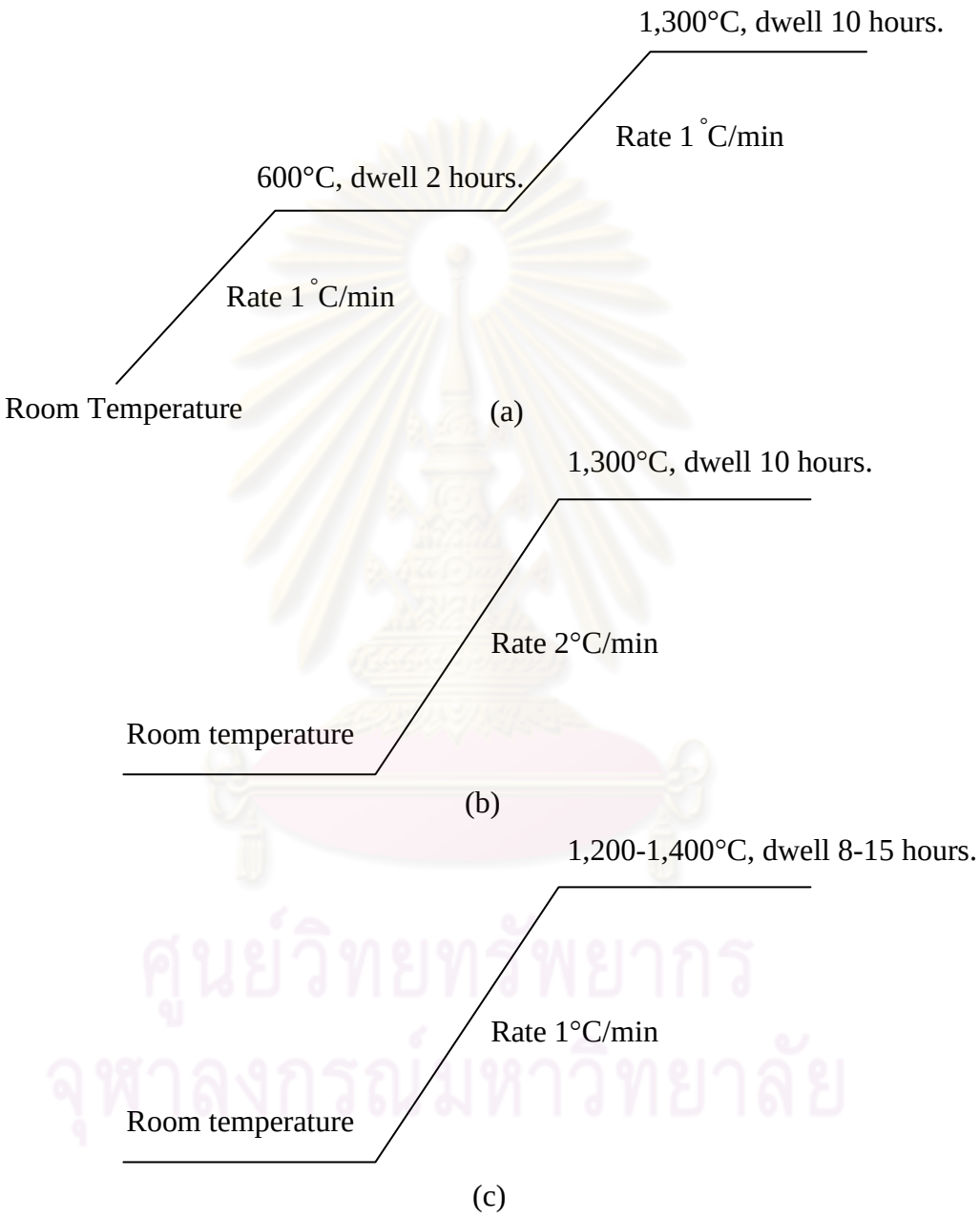

Figure 2.5 The sintering conditions of perovskite (a) LSF (b) LSCF and (c) LSF-LSCF composites.

2.6 Characterization techniques

2.6.1 X–Ray Diffractrometry (XRD)

The phase formations of perovskite oxide were investigated after calcinations and sintering by X-ray powder diffraction (XRD). The XRD patterns, for both powder and disc, were taken by using Rigaku, DMAX 2002 Ultima Plus X-Ray powder diffractometer equipped with a monochromator and a Cu-target X-ray tube (40 kV, 30 mA) and angles of 2θ ranged from 20-70 degree (step time 0.5 sec., scan step 0.020 degree) at Department of Chemistry, Faculty of Science, Chulalongkorn University.

2.6.2 Scanning Electron Microscopy (SEM)

The morphology of the sintered disc was carried out using a JEOL JSM-5800LV scanning electron microscopy, Oxford Instrument (Link ISIS series 300) at the Scientific and Technological Research Equipment Center (STREC), Chulalongkorn University. This instrument uses X-rays or electrons scattered back from the surface “illuminated” by a restored electron beam to generate an image with remarkable three-dimensional qualities.

2.7 The investigation of the perovskite properties

2.7.1 Density measurement

Density of perovskite disc was determined by the Archimedes immersion method using D.I. water as a medium, Precisa Gravimetrics AG (model R 2055M-DR), at Department of Chemistry, Faculty of Science, Chulalongkorn University.

2.7.2 Electrical conductivity measurement

The DC 4-probe is a device used to investigate the electrical property of the perovskite materials. The sintered disc was cut into a rectangular specimen with approximate dimensions of 12 mm x 5 mm x 1.5 mm. Four Pt wires were attached to the specimen with Pt paste as shown in Figure 2.6.

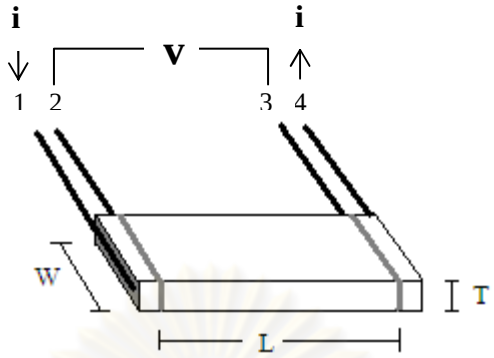

Figure 2.6 DC 4-probe measurement.

The specimen was heated to 950°C for 10 min with the heating rate of 5°C/min. The electrical conductivity measurements were performed in a tube furnace at the temperature range of room temperature to 800°C. Specimen was applied current (I) through the outer wires 1 to 4 and measured the voltages drop over wires 2 and 3 at each temperature by potentiostat/galvanostat (Autolab PG100).

The electrical conductivity was calculated by the equation:

$$\sigma = \frac{I}{V}\frac{L}{W \times T} \tag{2.1}$$

where σ = electrical conductivity

I = applied current (A)

V = resulting voltages (V)

L = length between Pt wires 2 and 3 (cm)

T = thickness of specimen (cm)

W = width of specimen (cm)

2.7.3 Thermal expansion measurement

The thermal expansion behavior explore the compatible behavior between electrolyte and electrode materials for SOFC.

A dilatometer, NETZSCH DIL 402C (from Department of Materials Science, Faculty of Science, Chulalongkorn University) was used to determine the thermal expansion coefficients (TEC) of the sintered specimens. The sintered disc was cut

into small pieces (about 12 mm in length, 5 mm in width and 1.5 mm in thickness). The length of the sample piece was measured as the temperature increased from room temperature to 800°C in air.

CHAPTER III

RESULTS AND DISCUSSIONS

The objectives of this research are as follows:

1. Synthesis of perovskite
    1.1 $La_{0.4}Sr_{0.6}FeO_{3-\delta}$ (LSF46) and $La_{0.3}Sr_{0.7}FeO_{3-\delta}$ (LSF37) by modified citrate method.
    1.2 $La_{0.8}Sr_{0.2}Co_{0.9}Fe_{0.1}O_{3-\delta}$ (LSCF8291) and $La_{0.8}Sr_{0.2}Co_{0.8}Fe_{0.2}O_{3-\delta}$ (LSCF8282) by citrate method.
    1.3 LSF37-LSCF8291, LSF37-LSCF8282, LSF46-LSCF8291, LSF46-LSCF8282 composites by physical mixing method in various weight ratios, calcination temperature, sintering temperature and sintering time.
2. Characterization techniques
    2.1 X-ray diffractrometry (XRD) of LSF, LSCF and LSF-LSCF composites
    2.2 Scanning electron microscopy (SEM) of LSF, LSCF and LSF-LSCF composites
3. The investigation of the perovskite properties
    3.1 Density of LSF, LSCF and LSF-LSCF composites
    3.2 Electrical conductivity of LSF, LSCF and LSF-LSCF composites
    3.3 Thermal expansion coefficient (TEC) of LSF, LSCF and the highest conductivity LSF-LSCF composites

3.1 Synthesis of perovskite

3.1.1 $La_{1-x}Sr_xFeO_{3-\delta}$ (LSF) (x = 0.6 and 0.7) by modified citrate method

The perovskite oxides were prepared by modified citrate method. The metal nitrates were dissolved in distilled water, which then reacted with the mole ratio of metal nitrate to citric acid, 1:2 to form metal-citrate-nitrate complexes. These metal-citrate complexes can undergo polymerization when ammonia solution was added. While $NH_3 \cdot H_2O$ was added, the white fume of NH_4NO_3 was suddenly observed, which came from the free NO_3^- reacting with $NH_3 \cdot H_2O$ and generated heat. Then, the

solution changed from clear red brown to clear deep brown solution (pH ≈ 9). The excess solvent was evaporated until a sticky gel was obtained. Finally, at around 200°C the spontaneous combustion occurred and the black oxide powder was obtained. The mixture powder was calcined at 900°C for 6 hours to achieve pure phase and removed residual organic compound. The calcined powder was ground and pressed to make a disc. The perovskite discs were sintered in air at 1,300°C for 10 hours to increase the density of the perovskite disc and eliminate the pores.

3.1.2 $La_{0.8}Sr_{0.2}Co_{1-x}Fe_xO_{3-\delta}$ (LSCF) (x = 0.1 and 0.2) by citrate method

The mixed LSCF systems were prepared via the citrate process. The metal nitrates were dissolved in distilled water, which then reacted with the mole ratio of metal nitrate to citric acid, 1:1.2 to form metal-citrate-nitrate complexes. These metal-citrate complexes can form polymeric precursor when solution is heated at 96-100^{o}C for 3.5 hours. The solution changed from partially dissolved dark red solution to dark red gel**.** Finally, at around 200°C the spontaneous combustion occurred and the black oxide powder was obtained. The mixture powder was calcined at 800°C for 4 hours to achieve pure phase and removed residual organic compound. The calcined powder was ground and pressed to make a disc. The perovskite discs were sintering in air at 1,300°C for 10 hours to increase the density of the perovskite disc and eliminate the pores.

3.1.3 $La_{1-x}Sr_xFeO_{3-\delta}$ (LSF) - $La_{0.8}Sr_{0.2}Co_{1-x}Fe_xO_{3-\delta}$ (LSCF) composites by physical mixing method

The composite perovskite powders LSF-LSCF were prepared by physical method with various weight ratios. The mixture powder was calcined at 800-1,000°C for 10 hours to achieve pure phase and removed residual organic compound. The calcined powder was ground and pressed to make a disc. The perovskite discs were sintering in air at 1,200-1,400°C for 8-15 hours to increase the density of the perovskite disc and eliminate the pores.

3.2 Characterization of the synthesized compounds

The structures of synthesized perovskite compounds were characterized by XRD and the surface morphology of the sintered discs were examined by SEM.

3.2.1 X-ray diffraction (XRD)

XRD was used to indicate the formation of the perovskite phase. The phase formations of perovskites were investigated after calcination and sintering. The diffraction peaks of perovskites were observed within angles of 2θ ranged from 20-70 degree.

3.2.1.1 Phase formation of $La_{1-x}Sr_xFeO_{3-\delta}$ (x = 0.6 and 0.7)

The formation of $La_{1-x}Sr_xFeO_{3-\delta}$ (x = 0.6 and 0.7) calcined powders investigated by XRD was shown in Figure 3.1.

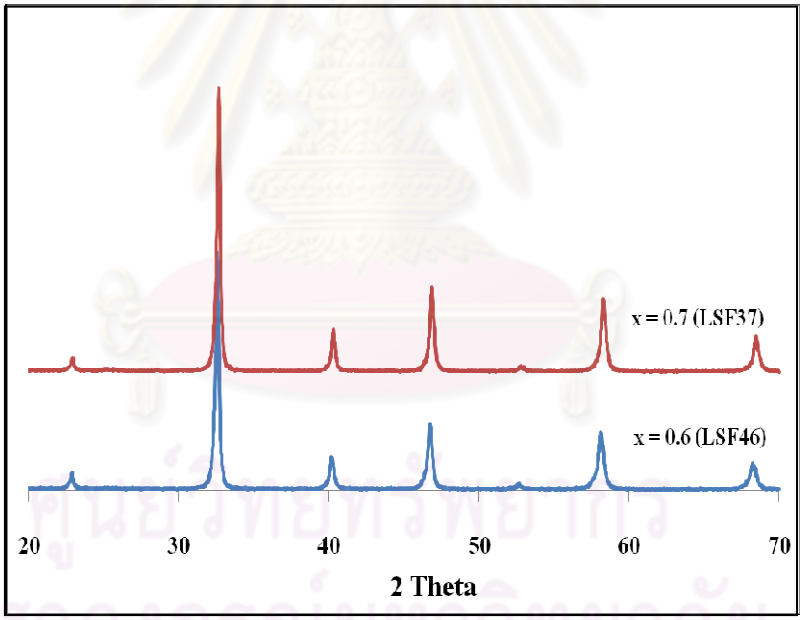

Figure 3.1 XRD patterns of $La_{1-x}Sr_xFeO_{3-\delta}$ (x = 0.6 and 0.7) powders after calcined at 900°C for 6 hours.

The XRD patterns of LSF exhibited the single phase of ABO_3 perovskite oxides with a cubic structure. The lattice parameter calculated by Jade software was shown in Table 3.1.

It was observed that the XRD patterns shifted to the higher angle with increasing of Sr in $La_{1-x}Sr_xFeO_{3-\delta}$, corresponding to the lattice shrinkage. When La lattice sites (La^{3+}; 1.032 Å) are partially occupied by the larger ionic radius of Sr^{2+} (1.180 Å), the charge imbalance occurs. Some of Fe^{3+} (0.645 Å) oxidized to Fe^{4+} (0.585 Å) reduces the average ion radius of the B-site [35]. When content of Sr increases, the lattice must be reduced to maintain the perovskite structure, causing smaller lattice parameter.

Table 3.1 The lattice parameters of $La_{1-x}Sr_xFeO_{3-\delta}$ (x = 0.6 and 0.7) after calcined at 900°C for 6 hours.

Ratio	**Lattice parameter (Å)**
x = 0.6	3.871
x = 0.7	3.850

3.2.1.2 Phase formation of $La_{0.8}Sr_{0.2}Co_{1-x}Fe_xO_{3-\delta}$ (x = 0.1 and 0.2)

The formation of $La_{0.8}Sr_{0.2}Co_{1-x}Fe_xO_{3-\delta}$ (x = 0.1 and 0.2) calcined powders investigated by XRD was shown in Figure 3.2.

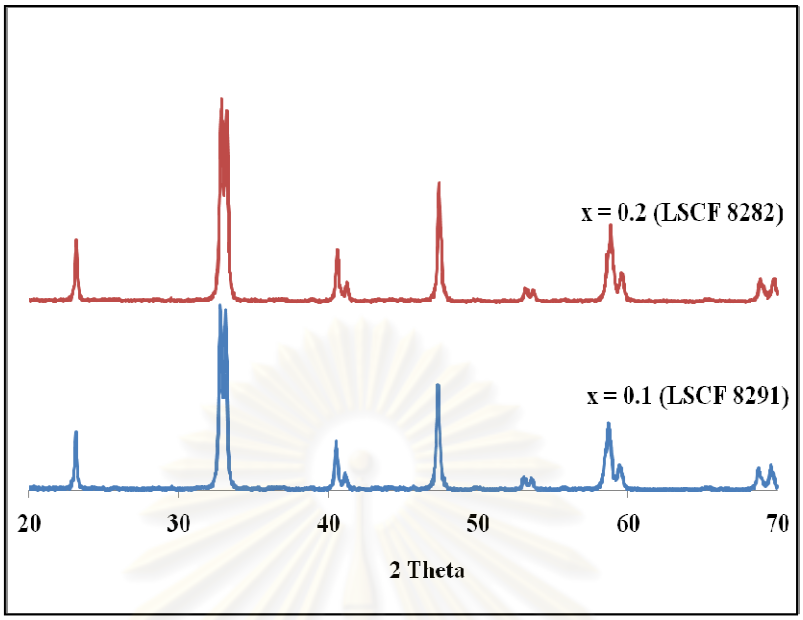

Figure 3.2 XRD patterns of $La_{0.8}Sr_{0.2}Co_{1-x}Fe_xO_{3-\delta}$ (x = 0.1 and 0.2) powders after calcined at 800°C for 4 hours.

Figure 3.2 shows the XRD patterns of $La_{0.8}Sr_{0.2}Co_{0.9}Fe_{0.1}O_{3-\delta}$ (LSCF8291) and $La_{0.8}Sr_{0.2}Co_{0.8}Fe_{0.2}O_{3-\delta}$ (LSCF8282). It demonstrated that all samples have no any impurity phase and the structures are rhombohedral [42]. The XRD peak slightly shifted to the higher angle with increasing of Fe in $La_{0.8}Sr_{0.2}Co_{1-x}Fe_xO_{3-\delta}$ since the ionic radius of Fe^{3+} (0.645 Å) is smaller than that of Co^{3+} (0.718 Å), corresponding to the lattice shrinkage. The lattice must be reduced to maintain the perovskite structure, causing smaller lattice parameter. The decrease of lattice parameter with the increase of Fe content in $La_{0.8}Sr_{0.2}Co_{1-x}Fe_xO_{3-\delta}$ was shown in Table 3.2.

Table 3.2 The lattice parameters of $La_{0.8}Sr_{0.2}Co_{1-x}Fe_xO_{3-\delta}$ (x = 0.1 and 0.2) after calcined at 800°C for 4 hours.

Ratio	**Lattice parameter (Å)**		
	a	**b**	**c**
x = 0.1	5.452	5.452	13.150
x = 0.2	5.435	5.435	13.116

3.2.1.3 Phase formation of LSF-LSCF composites

The XRD patterns of $La_{0.3}Sr_{0.7}FeO_{3-\delta}$ (LSF37)-$La_{0.8}Sr_{0.2}Co_{0.9}Fe_{0.1}O_{3-\delta}$ (LSCF8291) composite with ratio 1:3 calcined at 800-1,000^{o}C were illustrated in Figure 3.3.

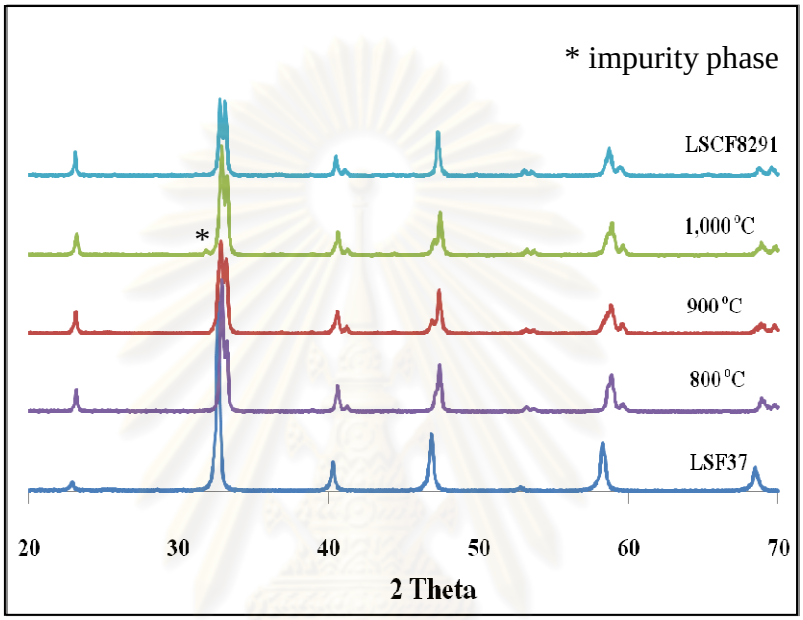

Figure 3.3 XRD patterns of LSF37-LSCF8291 composite in a weight ratio of 1:3 at calcination temperature 800-1,000^{o}C for 10 hours in air.

The pattern obtained after heating to 800^{o}C is indicative of a mixture of LSF and LSCF phases. The impurity phase was observed in XRD patterns of the composite calcined at 1,000^{o}C. It indicated that the optimum calcination temperature for LSF-LSCF composites should be 800 and 900^{o}C.

The formation of LSF37-LSCF8291 and LSF37-LSCF8282 composites calcined powders with different weight ratios investigated by XRD was shown in Figure 3.4.

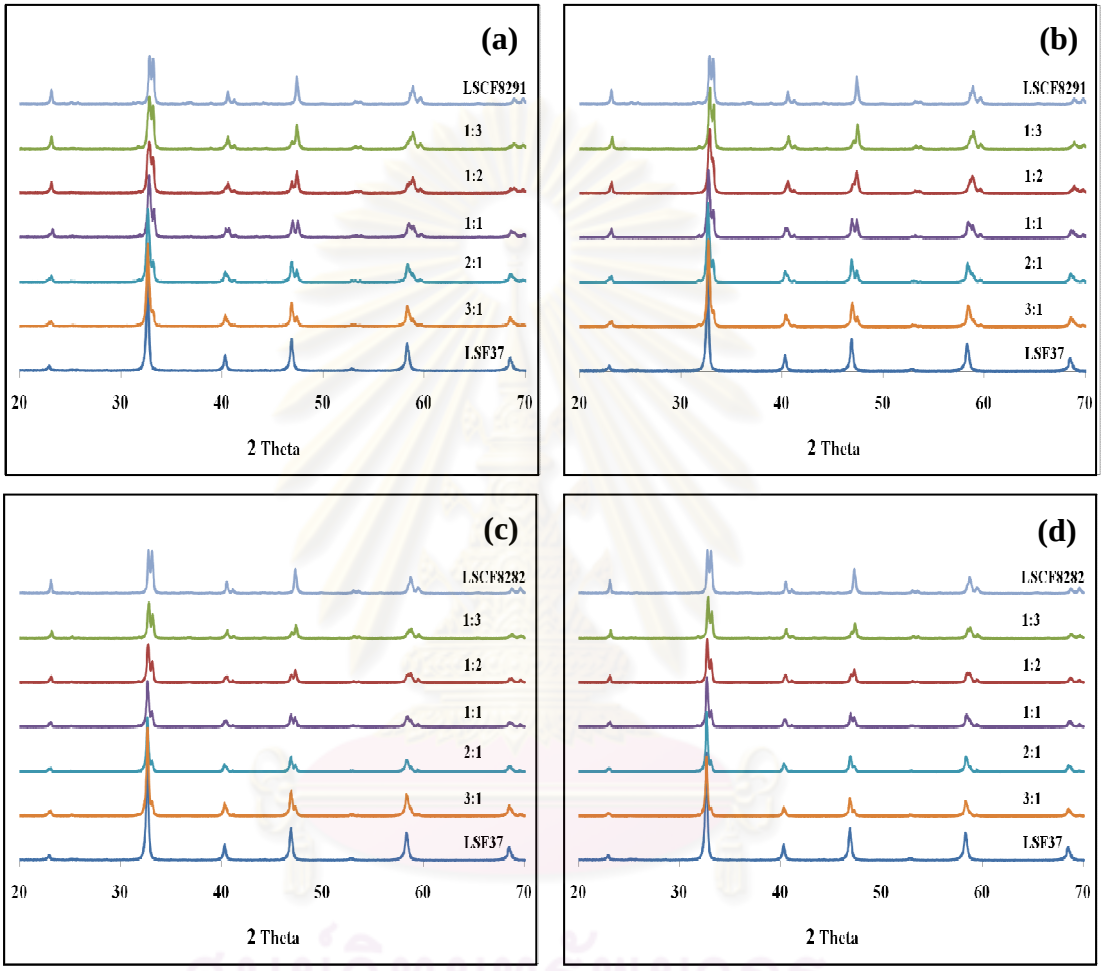

Figure 3.4 XRD patterns of LSF-LSCF composites with different weight ratios. (a) LSF37-LSCF8291 after calcined at 800^{o}C, (b) LSF37-LSCF8291 after calcined at 900^{o}C, (c) LSF37-LSCF8282 after calcined at 800^{o}C and (d) LSF37-LSCF8282 after calcined at 900^{o}C.

The formation of LSF46-LSCF8291 and LSF46-LSCF8282 composites calcined powders with various weight ratios investigated by XRD was shown in Figure 3.5.

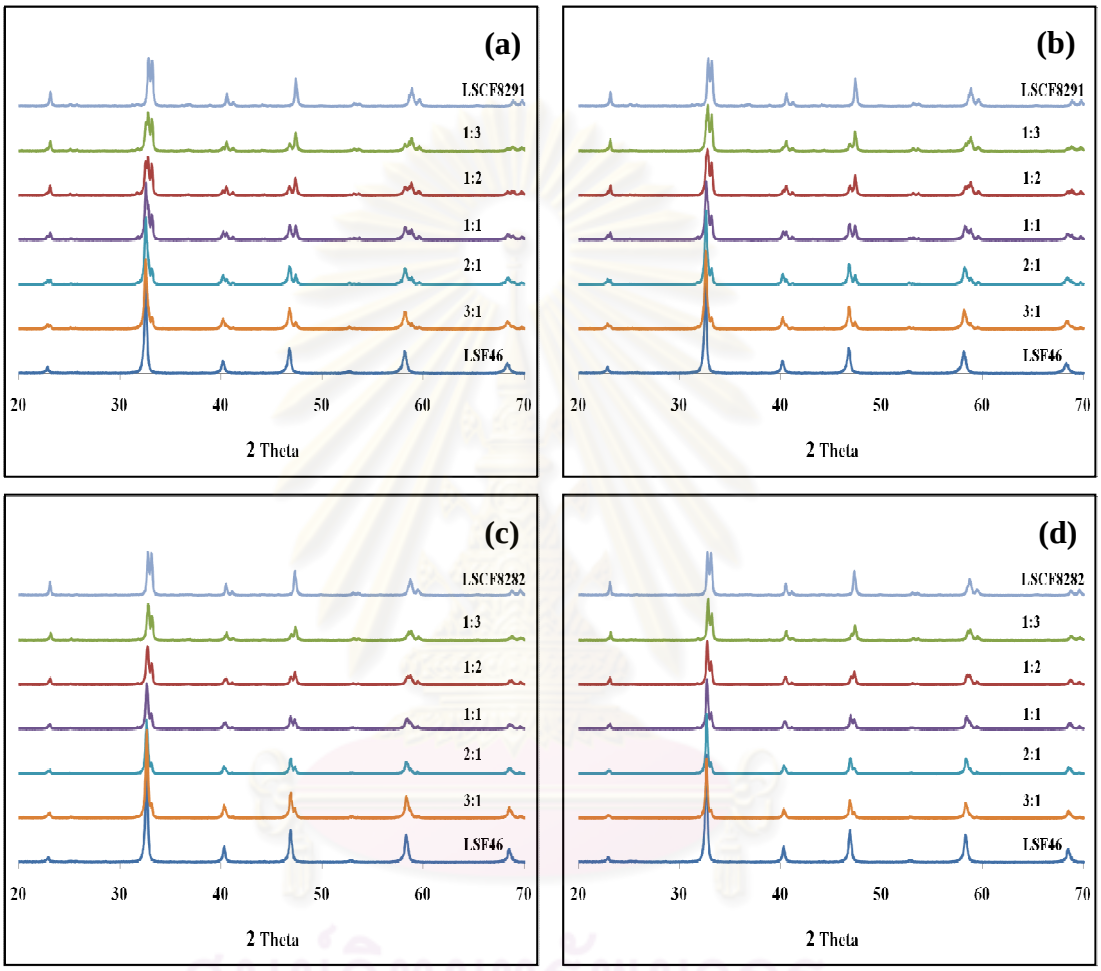

Figure 3.5 XRD patterns of LSF-LSCF composites with various weight ratios. (a) LSF46-LSCF8291 after calcined at 800^{o}C, (b) LSF46-LSCF8291 after calcined at 900^{o}C, (c) LSF46-LSCF8282 after calcined at 800^{o}C and (d) LSF46-LSCF8282 after calcined at 900^{o}C.

The XRD patterns of LSF-LSCF composites calcined at 800 and 900^{o}C with different weight ratios shown in Figures 3.4 and 3.5, revealed the dual-phase composites comprising LSF and LSCF based solutions with cubic perovskite and rhombohedral lattice, respectively. The diffraction patterns (Figure 3.6) are shown only in the region between 20° and 45° 2θ to focus on the major peaks of LSF-LSCF.

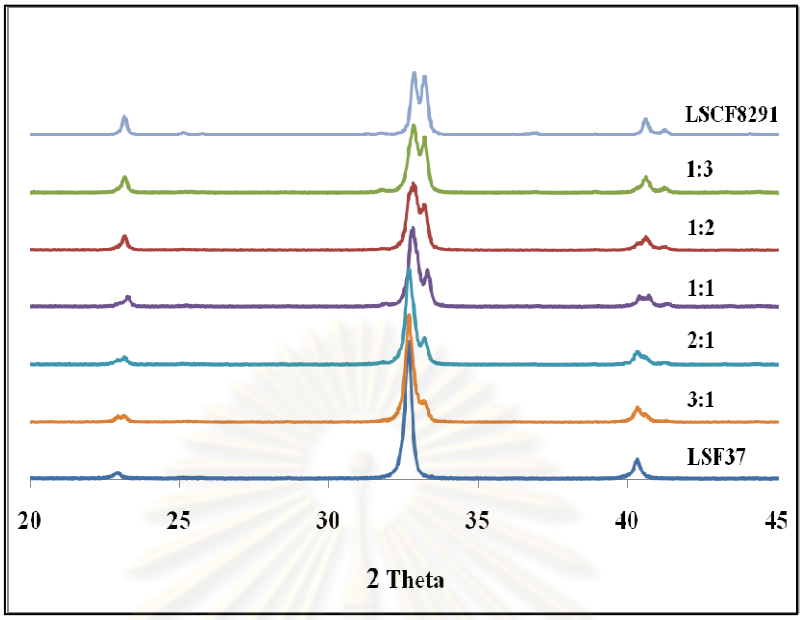

Figure 3.6 Magnified XRD pattern of LSF37-LSCF8291 composite with various weight ratios after calcined at 800°C.

XRD analysis showed that, as expected LSF-LSCF (1:1 ratio) consisted of two equal phases. When the content of LSCF is higher than LSF, the peaks shifted very slightly to the higher angle. The XRD data and comparison of composite unit cell parameters with those in LSF and LSCF system, confirm that LSF part was dissolved in the LSCF lattice. Similarly, LSCF part dissolved into the LSF structure when amounts of LSF are greater than LSCF, corresponding to the XRD peaks shifted to the lower angle direction. But the patterns still showed two perovskite phases: LSF and LSCF, which may indicate that no significant chemical reaction occur between the LSF and LSCF [47].

It is noticed that the XRD patterns of LSF-LSCF composites after calcined at 800 and 900°C do not differ significantly. Therefore 800°C was selected as minimum temperature for calcination LSF-LSCF composite powder.

In Figure 3.7, XRD patterns of LSF-LSCF composites (1:3) sintered at 1,200, 1,300 and 1,400°C for 10 hours are presented.

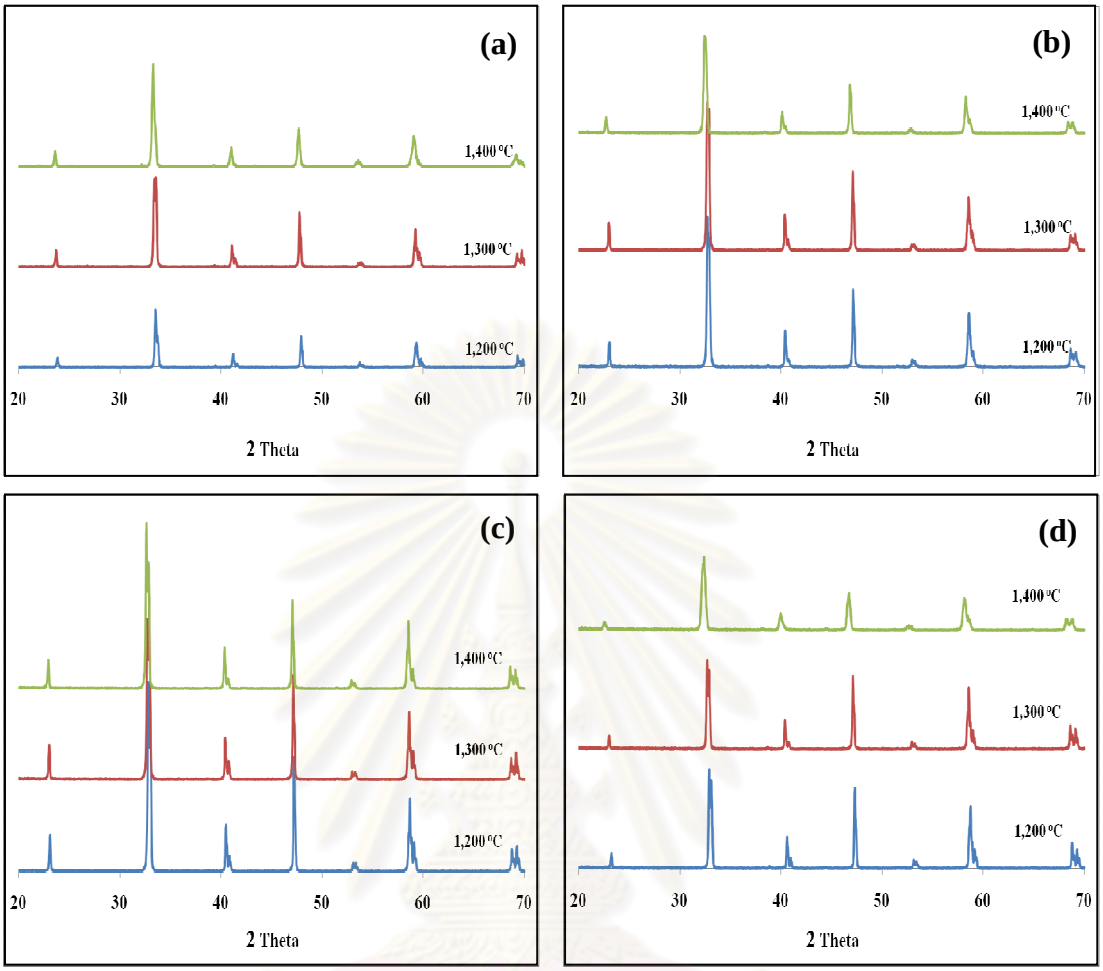

Figure 3.7 XRD patterns of LSF-LSCF composites in a weight ratio of 1:3 after calcined at 800°C with different sintering temperatures for 10 hours in air. (a) LSF37-LSCF8291, (b) LSF37-LSCF8282, (c) LSF46-LSCF8291 and (d) LSF46-LSCF8282.

The sintering behavior of LSF-LSCF compacts in air also shown in the range of 20° and 45° 2θ were exhibited in Figure 3.8.

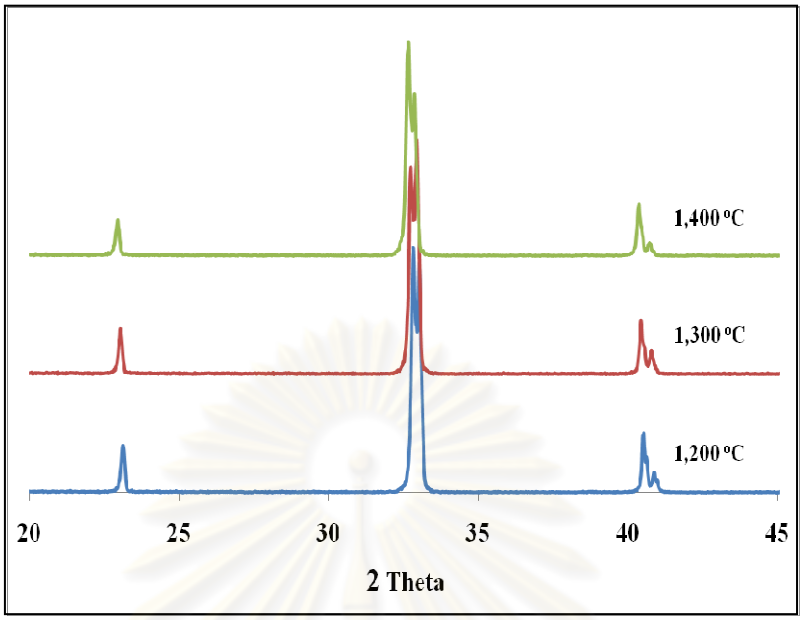

Figure 3.8 Magnified XRD pattern of LSF46-LSCF8291 composite with different sintering temperatures for 10 hours.

In Figures 3.7 and 3.8, the major peaks shift a bit to the low two-theta or the higher of spacing direction when the sintering temperatures is pushed up from 1,200 to 1,400^{o}C, which represents an increase in lattice length (see Table 3.3). The expansion of the lattice was observed. It is suggested that the change in lattice parameter is due to the high solubility of LSF into LSCF structure.

In all patterns, the main peaks are indexed with in the distorted rhombohedral structure of LSCF. The width of the peaks corresponding to peak ~ 32^{o} decreased with the increase of sintering temperature which is related to crystalline grains growth.

Table 3.3 The lattice parameters of LSF-LSCF composites in a weight ratio of 1:3 after calcined at 800^{o}C with different sintering temperature for 10 hours in air.

Sintering temperature (^{o}C)	**LSF37-LSCF8291**			**LSF37-LSCF8282**		
	Lattice parameter (Å)			**Lattice parameter (Å)**		
	a	**b**	**c**	**a**	**b**	**c**
1,200	5.329	5.329	13.119	5.335	5.335	13.104
1,300	5.354	5.354	13.135	5.342	5.342	13.111
1,400	5.371	5.371	13.148	5.359	5.359	13.130

Sintering temperature (^{o}C)	**LSF46-LSCF8291**			**LSF46-LSCF8282**		
	Lattice parameter (Å)			**Lattice parameter (Å)**		
	a	**b**	**c**	**a**	**b**	**c**
1,200	5.355	5.355	13.120	5.342	5.342	13.098
1,300	5.376	5.376	13.143	5.366	5.366	13.114
1,400	5.388	5.388	13.160	5.385	5.385	13.126

The composites after sintered at 1,300^{o}C were sintered with various sintering temperatures (8-15 hours).

The XRD patterns of LSF-LSCF composites in a weight ratio of 1:3 after calcined at 800^{o}C with different sintering time for sintered at 1,300^{o}C were illustrated in Figure 3.9. Figure 3.10 show XRD pattern of LSF37-LSCF8282 for the Bragg angle range of 20°-45° 2θ.

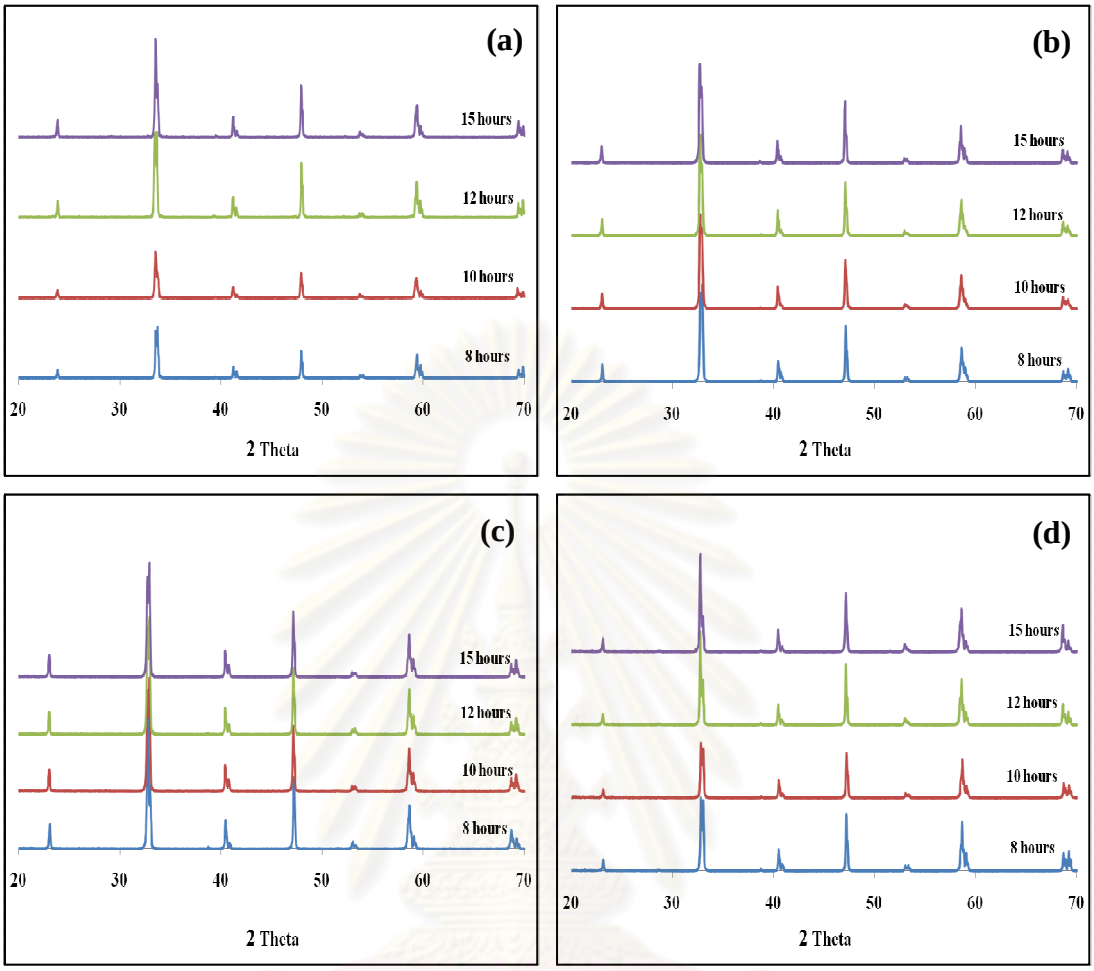

Figure 3.9 XRD patterns of LSF-LSCF composites in a weight ratio of 1:3 after calcined at 800^{o}C with different sintering time for sintered at 1,300^{o}C in air. (a) LSF37-LSCF8291, (b) LSF37-LSCF8282, (c) LSF46-LSCF8291 and (d) LSF46-LSCF8282.

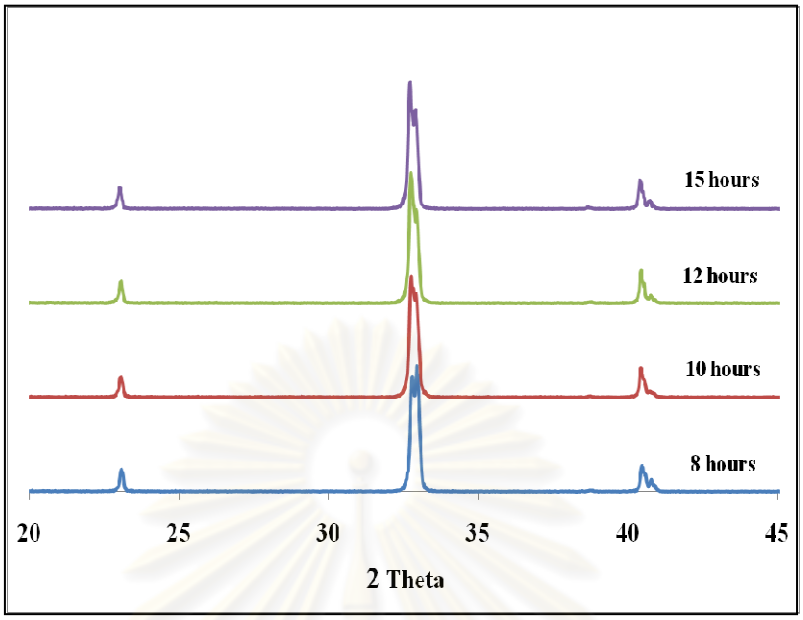

Figure 3.10 Magnified XRD patterns of LSF37-LSCF8282 with different sintering time for sintered at 1,300^{o}C.

However, the patterns showed that heating the composite to 1,300^{o}C for 8-15 hours did not cause the significant shift in the peak position for LSF-LSCF phase. The lattice parameters of LSF-LSCF composites in a weight ratio of 1:3 with different sintering time were shown in Table 3.4.

It is concluded that the optimum conditions to prepared pure LSF-LSCF composites (1:3) are 800^{o}C for calcination and 1,300^{o}C 10 hours for sintering.

Table 3.4 The lattice parameters of LSF-LSCF composites in a weight ratio of 1:3 after calcined at 800°C with different sintering time for sinterd at 1,300°C in air.

Sintering time (hour)	LSF37-LSCF8291			LSF37-LSCF8282		
	Lattice parameter (Å)			Lattice parameter (Å)		
	a	b	c	a	b	c
8	5.354	5.354	13.134	5.340	5.340	13.111
10	5.354	5.354	13.135	5.342	5.342	13.111
12	5.355	5.355	13.133	5.342	5.342	13.112
15	5.353	5.353	13.133	5.341	5.341	13.110

Sintering time (hour)	LSF46-LSCF8291			LSF46-LSCF8282		
	Lattice parameter (Å)			Lattice parameter (Å)		
	a	b	c	a	b	c
8	5.377	5.377	13.143	5.366	5.366	13.112
10	5.376	5.376	13.143	5.366	5.366	13.114
12	5.374	5.374	13.144	5.365	5.365	13.116
15	5.376	5.376	13.145	5.367	5.367	13.114

3.2.2 Scanning electron microscope (SEM) and density

The surface morphologies of perovskite discs were characterized by SEM technique. Densities of samples were determined by the Archimedes immersion method using water as a medium.

3.2.2.1 Morphologies of $La_{1-x}Sr_xFeO_{3-\delta}$ (x = 0.6 and 0.7)

The surface morphology of $La_{1-x}Sr_xFeO_{3-\delta}$ (x = 0.6 and 0.7) sintered discs was investigated by SEM shown in Figure 3.11.

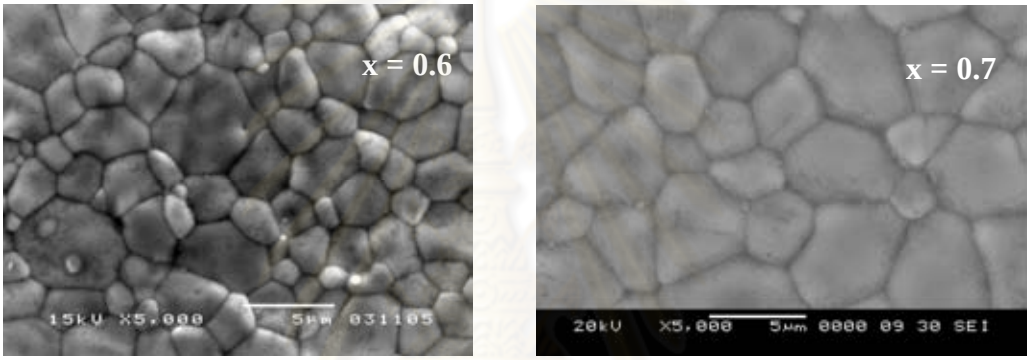

Figure 3.11 Surface morphology of $La_{1-x}Sr_xFeO_{3-\delta}$ (x = 0.6 and 0.7) discs.

SEM micrographs of $La_{1-x}Sr_xFeO_{3-\delta}$ (x = 0.6 and 0.7) discs exhibited high density (relative density > 92%) and homogeneous surface. The grain size increases with increasing of Sr content. The relative density of $La_{1-x}Sr_xFeO_{3-\delta}$ discs increased with the increase of Sr which was listed in Table 3.5.

Table 3.5 Density of $La_{1-x}Sr_xFeO_{3-\delta}$ (x = 0.6 and 0.7) discs.

Ratio	Density ($g.cm^3$)	Relative density (%)
x = 0.6	5.623	92.44
x = 0.7	5.635	93.38

3.2.2.2 Morphologies of $La_{0.8}Sr_{0.2}Co_{1-x}Fe_xO_{3-\delta}$ (x = 0.1 and 0.2)

The surface morphology of $La_{0.8}Sr_{0.2}Co_{1-x}Fe_xO_{3-\delta}$ (x = 0.1 and 0.2) discs after sintered at 1,300°C for 10 hours were indicated in Figure 3.12.

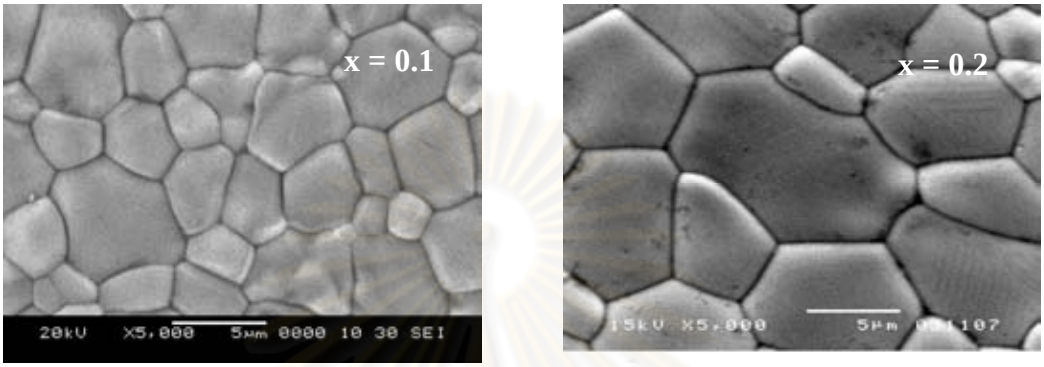

Figure 3.12 Surface morphology of $La_{0.8}Sr_{0.2}Co_{1-x}Fe_xO_{3-\delta}$ (x = 0.1 and 0.2) discs.

The morphologies of $La_{0.8}Sr_{0.2}Co_{1-x}Fe_xO_{3-\delta}$ show dense (relative density > 97%) and homogeneous surface. The grain size increases with increasing of Fe content. The relative density of $La_{0.8}Sr_{0.2}Co_{1-x}Fe_xO_{3-\delta}$ with various Fe contents was listed in Table 3.6.

Table 3.6 Density of $La_{0.8}Sr_{0.2}Co_{1-x}Fe_xO_{3-\delta}$ (x = 0.1 and 0.2) discs.

Ratio	Density ($g.cm^3$)	Relative density (%)
x = 0.1	5.885	98.09
x = 0.2	5.875	97.18

3.2.2.3 Morphologies of LSF-LSCF composites

The surface morphology of LSF37-LSCF8291 and LSF37-LSCF8282 composites discs after calcined at 800^{o}C with different weight ratio for sintered at 1,300^{o}C were investigated by SEM shown in Figures 3.13 and 3.14, respectively. The cross section of LSF-LSCF composite discs are presented in Figure 3.15.

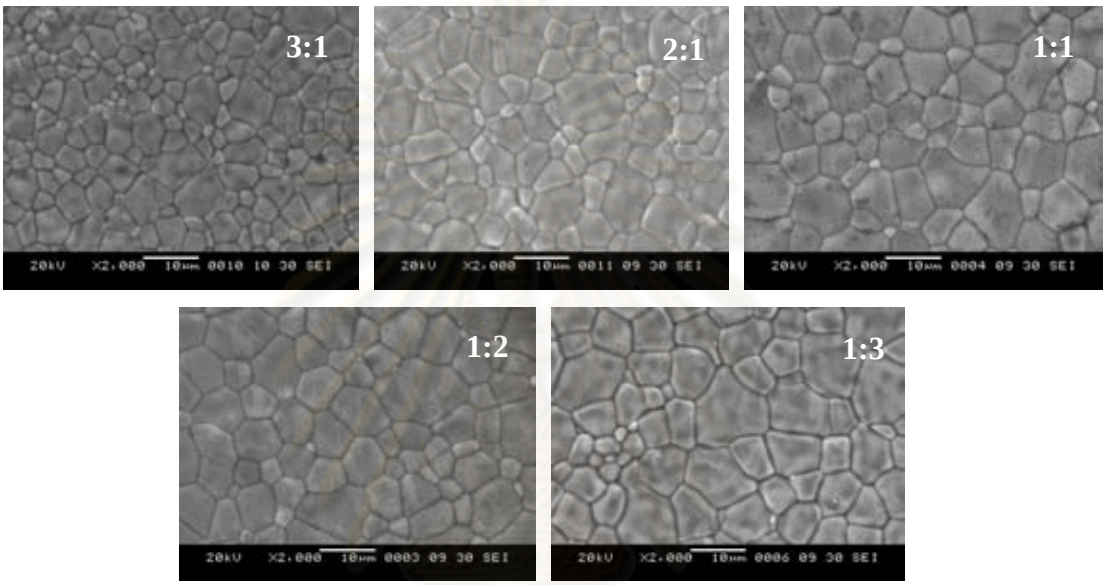

Figure 3.13 Surface morphology of LSF37-LSCF8291 composite discs.

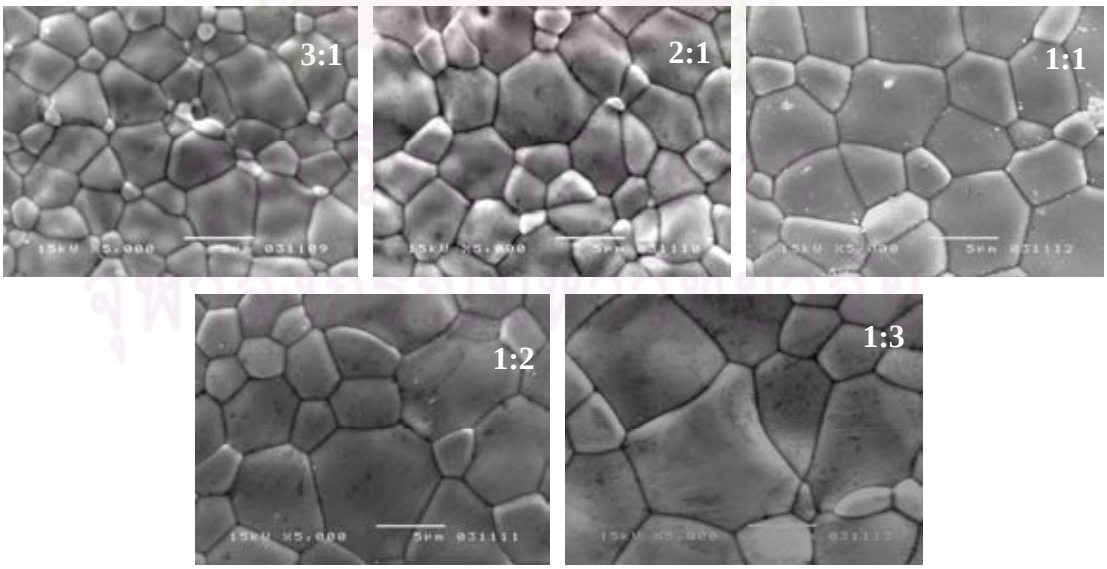

Figure 3.14 Surface morphology of LSF37-LSCF8282 composite discs.

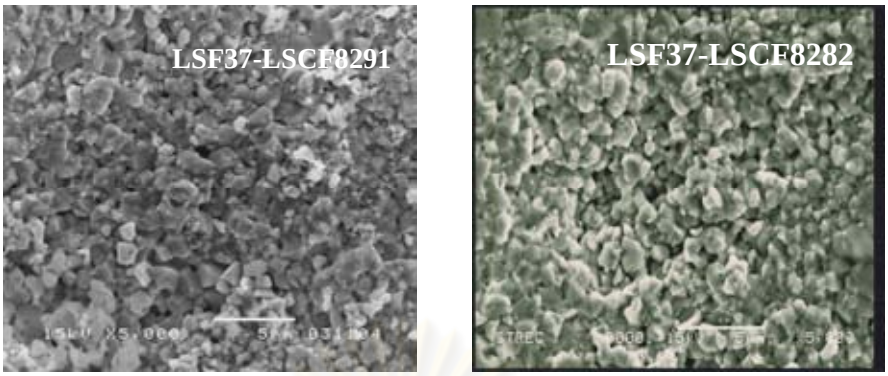

Figure 3.15 SEM pictures of cross section of LSF37-LSCF8291 and LSF37-LSCF8282 composite discs.

These SEM images exhibited the slightly larger grain size with the increase of LSCF content. The micrograph exhibited non-uniform grain structure with no porosity. There was no second phase present in the microstructures that confirmed the phase purity of LSF-LSCF composites that was indicated by XRD results.

The surface morphologies of LSF46-LSCF8291 and LSF46-LSCF8282 composites discs after calcined at 800^{o}C with different weight ratio for sintered at 1,300^{o}C were investigated by SEM shown in Figures 3.16 and 3.17, respectively. The cross section of LSF-LSCF composite discs are presented in Figure 3.18.

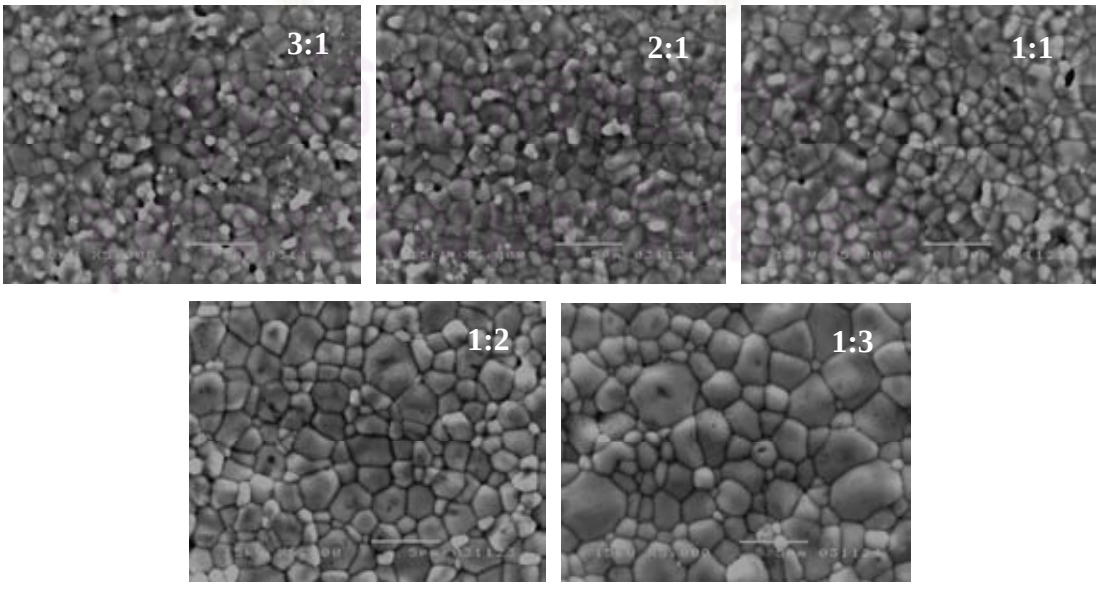

Figure 3.16 Surface morphology of LSF46-LSCF8291 composite discs.

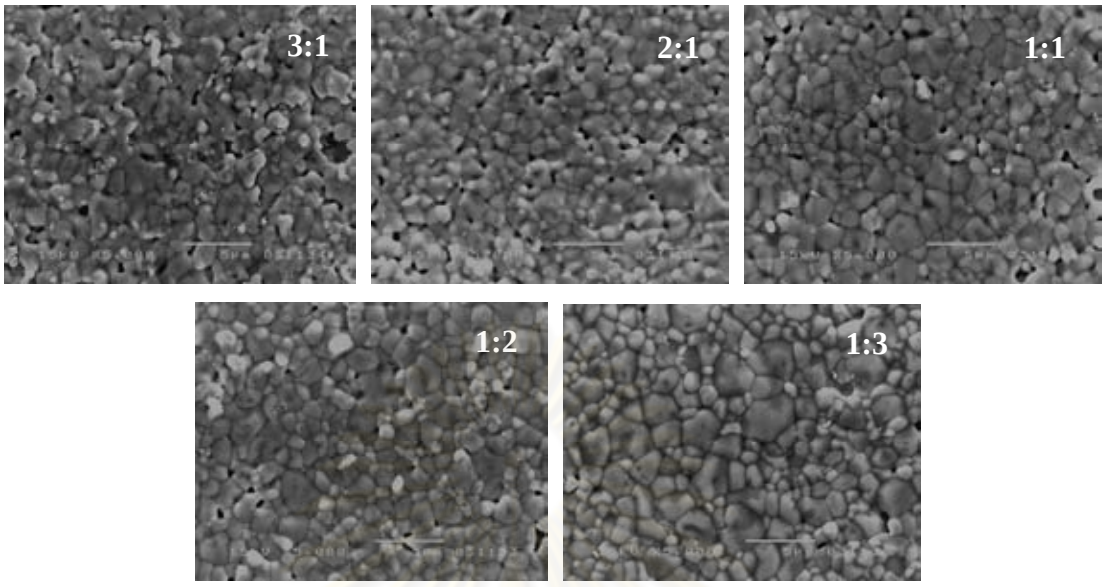

Figure 3.17 Surface morphology of LSF46-LSCF8282 composite discs.

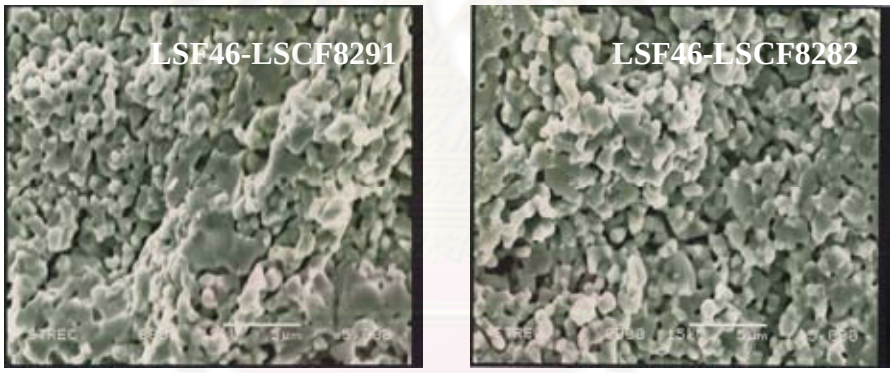

Figure 3.18 SEM pictures of cross section of LSF46-LSCF8291 and LSF46-LSCF8282 composite discs.

The grain sizes of LSF-LSCF composite were slightly larger with the increase of LSCF content and pore sizes decrease with an increasing content of LSCF. In addition, the large closed pores caused the decrease of the disc density. SEM inspection demonstrated the formation of homogeneous composites microstructures of LSF46-LSCF8291 and LSF46-LSCF8282.

The relative density of LSF-LSCF composite discs were listed in Tables 3.7 and 3.8. The densities of LSF-LSCF composites increase with the increase of LSCF content. According to our results, it was found that the morphology and the

relative density of LSF-LSCF composites after calcined at 800 and 900^{o}C do not differ significantly.

Table 3.7 Density of LSF37-LSCF8291 and LSF37-LSCF8282 composite discs with different weight ratios of LSCF.

(a) Calcined at 800^{o}C

Weight ratios of LSCF	LSF37-LSCF8291		LSF37-LSCF8282	
	Density (g.cm^3)	Relative density (%)	Density (g.cm^3)	Relative density (%)
0.25	5.323	93.84	5.337	93.52
0.33	5.401	94.20	5.429	94.12
0.50	5.615	95.85	5.636	95.67
0.67	5.776	96.55	5.776	96.04
0.75	5.899	97.61	5.862	96.48

(b) Calcined at 900^{o}C

Weight ratios of LSCF	LSF37-LSCF8291		LSF37-LSCF8282	
	Density (g.cm^3)	Relative density (%)	Density (g.cm^3)	Relative density (%)
0.25	5.337	94.08	5.344	93.64
0.33	5.434	94.78	5.435	94.23
0.50	5.633	96.16	5.655	95.99
0.67	5.788	96.75	5.788	96.24
0.75	5.868	97.10	5.889	96.93

Table 3.8 Density of LSF46-LSCF8291 and LSF46-LSCF8282 composite discs with different weight ratios of LSCF.

(a) Calcined at 800^{o}C

Weight ratios of LSCF	LSF46-LSCF8291		LSF46-LSCF8282	
	Density (g.cm^3)	Relative density (%)	Density (g.cm^3)	Relative density (%)
0.25	5.376	93.94	5.353	92.99
0.33	5.474	94.83	5.463	94.12
0.50	5.639	95.99	5.613	95.06
0.67	5.775	96.66	5.750	95.76
0.75	5.871	97.45	5.832	96.32

(b) Calcined at 900^{o}C

Weight ratios of LSCF	LSF46-LSCF8291		LSF46-LSCF8282	
	Density (g.cm^3)	Relative density (%)	Density (g.cm^3)	Relative density (%)
0.25	5.394	94.26	5.365	93.20
0.33	5.491	95.12	5.464	94.14
0.50	5.651	96.19	5.614	95.08
0.67	5.788	96.88	5.768	96.06
0.75	5.883	97.65	5.868	96.91

The surface morphology of LSF37-LSCF8291, LSF37-LSCF8282, LSF46-LSCF8291 and LSF46-LSCF8282 composites in a weight ratio of 1:3 after calcined at 800^{o}C with different sintering temperatures for 10 hours were exhibited in Figures 3.19, 3.20, 3.21 and 3.22, respectively.

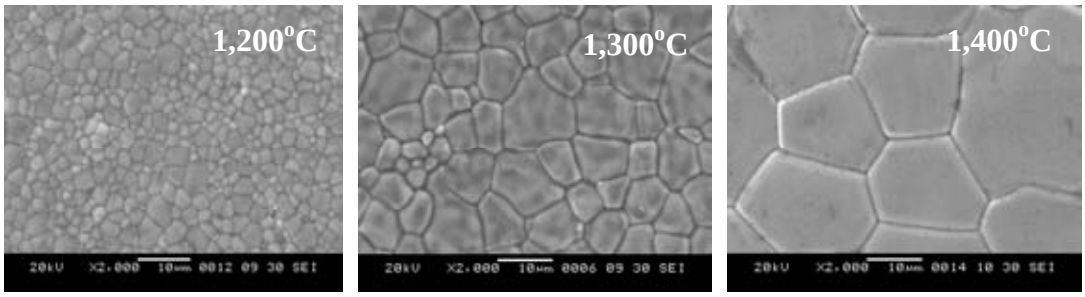

Figure 3.19 Surface morphology of LSF37-LSCF8291 composite discs.

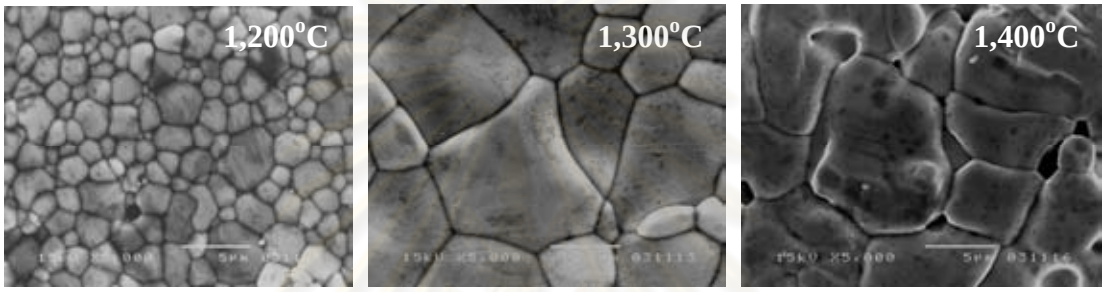

Figure 3.20 Surface morphology of LSF37-LSCF8282 composite discs.

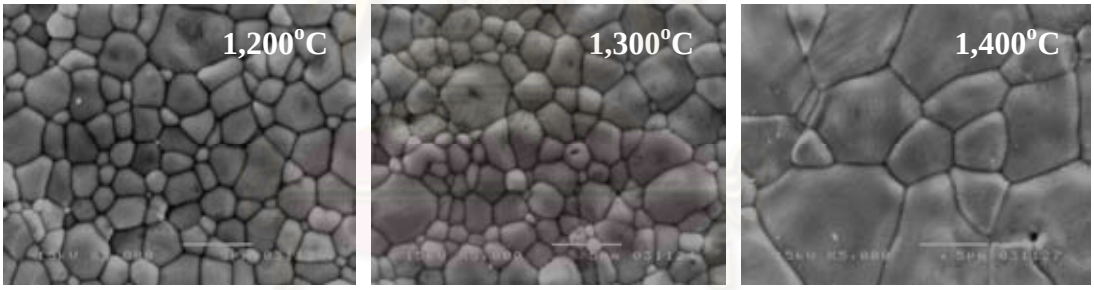

Figure 3.21 Surface morphology of LSF46-LSCF8291 composite discs.

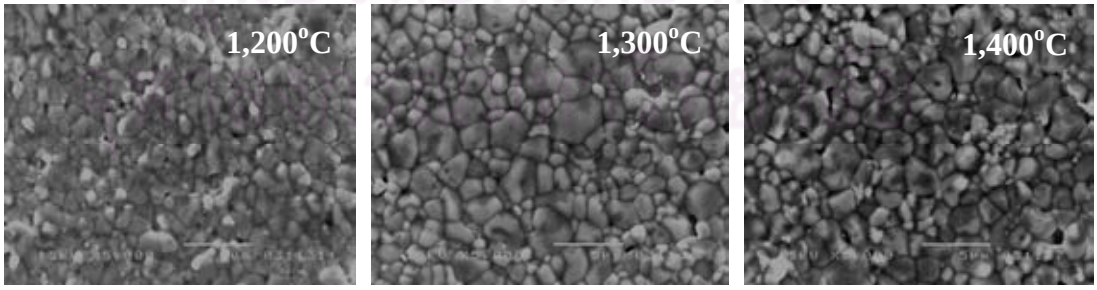

Figure 3.22 Surface morphology of LSF46-LSCF8282 composite discs.

The results show that all of the samples were homogeneous and without any impurity phase. It is seen that the grain size of LSF-LSCF composites increases with increasing of the sintering temperature that was confirmed by XRD results. For the LSF46-LSCF8282 composites, the number of pores increased when the sintering temperature increased from 1,300 to 1,400^{o}C. The relative density of LSF-LSCF composite discs are more than 93% as shown in Table 3.9.

Table 3.9 Density of LSF-LSCF composite discs in a weight ratios of 1:3 after calcined at 800^{o}C with different sintering temperatures for 10 hours.

Sintering temperature (^{o}C)	**LSF37-LSCF8291**		**LSF37-LSCF8282**	
	Density (g.cm^{3})	**Relative density (%)**	**Density (g.cm^{3})**	**Relative density (%)**
1,200	5.845	96.22	5.831	95.67
1,300	5.899	97.61	5.862	96.48
1,400	5.739	95.66	5.655	93.80

Sintering temperature (^{o}C)	**LSF46-LSCF8291**		**LSF46-LSCF8282**	
	Density (g.cm^{3})	**Relative density (%)**	**Density (g.cm^{3})**	**Relative density (%)**
1,200	5.822	95.72	5.754	94.07
1,300	5.871	97.45	5.832	96.32
1,400	5.710	95.33	5.621	93.58

The relative density of composites is quite high after sintering at 1,300^{o}C. The effect of sintering time on the density and grain growth of the composite disc was investigated.

Figures 3.23, 3.24, 3.25 and 3.26 show the SEM micrographs of LSF37-LSCF8291, LSF37-LSCF8282, LSF46-LSCF8291 and LSF46-LSCF8282 composite discs in a weight ratio of 1:3 and sintered at 1,300^{o}C, respectively.

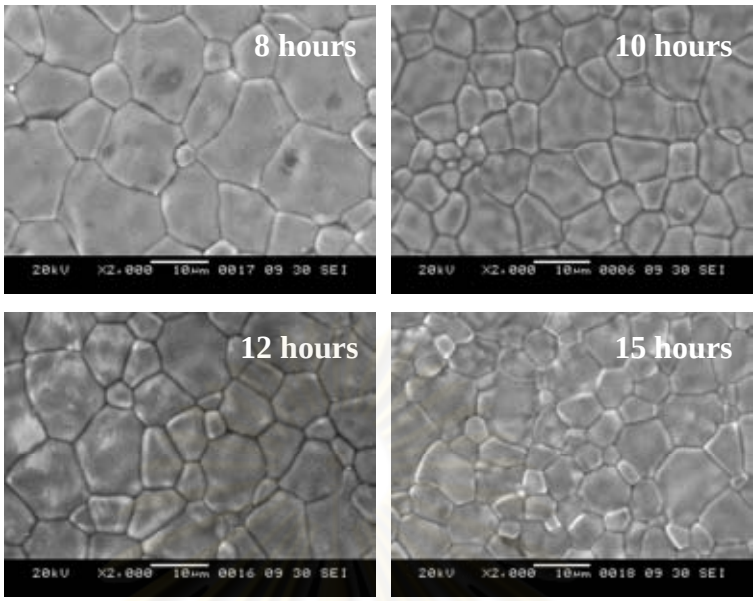

Figure 3.23 Surface morphology of LSF37-LSCF8291 composite discs.

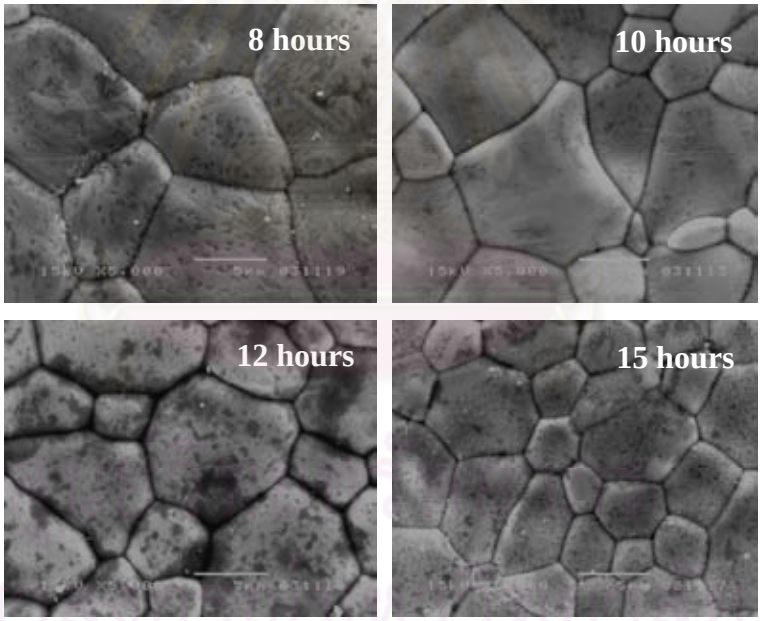

Figure 3.24 Surface morphology of LSF37-LSCF8282 composite discs.

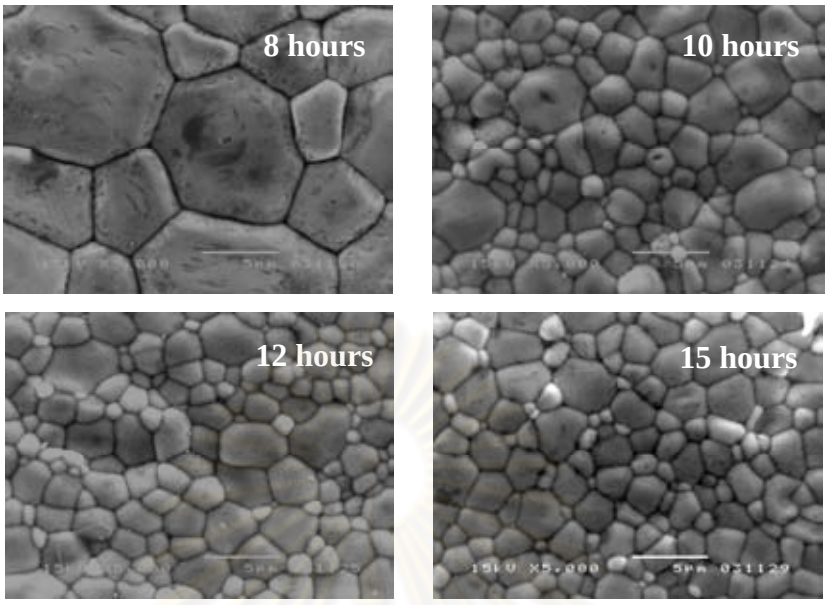

Figure 3.25 Surface morphology of LSF46-LSCF8291 composite discs.

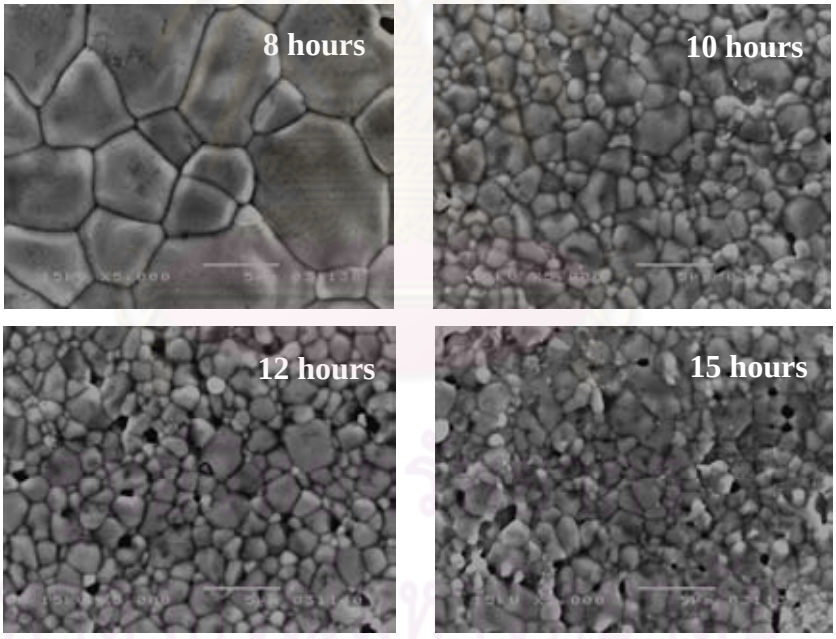

Figure 3.26 Surface morphology of LSF46-LSCF8282 composite discs.

SEM micrographs of LSF-LSCF composites showed dense packed grain and homogeneous surface. It is seen that the grain size of LSF37-LSCF8282 decreases with increasing of the sintering time. On the contrary, LSF37-LSCF8291, LSF46-LSCF8291 and LSF46-LSCF8282, the grain size decreases with increasing of the sintering time from 8 to 10 hours. But the increase of sintering time from 10 to 15

hours has no effect on the grain size. The number of pores for LSF46-LSCF8282 increased when the sintering time increase from 10 to 15 hours. The relative density of LSF-LSCF composite discs are more than 94% as shown in Table 3.10.

Table 3.10 Density of LSF-LSCF composite discs in a weight ratios of 1:3 after calcined at 800^{o}C with different sintering times for sintered at 1,300^{o}C.

Sintering time (hour)	LSF37-LSCF8291		LSF37-LSCF8282	
	Density ($g.cm^3$)	Relative density (%)	Density ($g.cm^3$)	Relative density (%)
8	5.855	96.88	5.818	95.69
10	5.899	97.61	5.862	96.48
12	5.825	96.41	5.793	95.35
15	5.826	96.35	5.789	95.24

Sintering time (hour)	LSF46-LSCF8291		LSF46-LSCF8282	
	Density ($g.cm^3$)	Relative density (%)	Density ($g.cm^3$)	Relative density (%)
8	5.811	96.49	5.776	95.38
10	5.871	97.45	5.832	96.32
12	5.804	96.28	5.652	93.32
15	5.789	96.11	5.633	93.07

No phase impurities and local inhomogenities were detected in LSF-LSCF composite ceramics. The relative density of composites is acceptable after sintering at 1,300^{o}C for 10 hours. In order to study the thermal expansion coefficient of these materials, the samples in a weight ratio of 1:3 after calcined at 800^{o}C and sintering at 1,300^{o}C for 10 hours were used.

3.3 Properties of perovskite compounds

3.3.1 Electrical conductivity

The total electrical conductivities of the obtained oxides as a function of temperature were measured by the DC 4–probes method. The measured value of total conductivity includes electronic and ionic contributions due to the presence of charge carriers and oxygen vacancies, respectively. However, ionic conductivity in the type of perovskite oxides is known to be small in comparison with the overall conductivity [36]. Therefore, the experimental value of the electrical conductivity is assumed to be the electronic conductivity alone.

The electrical conductivity is strongly dependent on temperature. The electrical conductivity of metals decreases with increasing temperature whereas the electrical conductivity of semiconductors increases with increasing temperature.

3.3.1.1 Electrical conductivity of $La_{1-x}Sr_xFeO_{3-\delta}$ (x = 0.6 and 0.7)

As shown in Figure 3.27, the electrical conductivities of the $La_{1-x}Sr_xFeO_{3-\delta}$ (x = 0.6 and 0.7) were studied as a function of temperature from room temperature to 800°C in air.

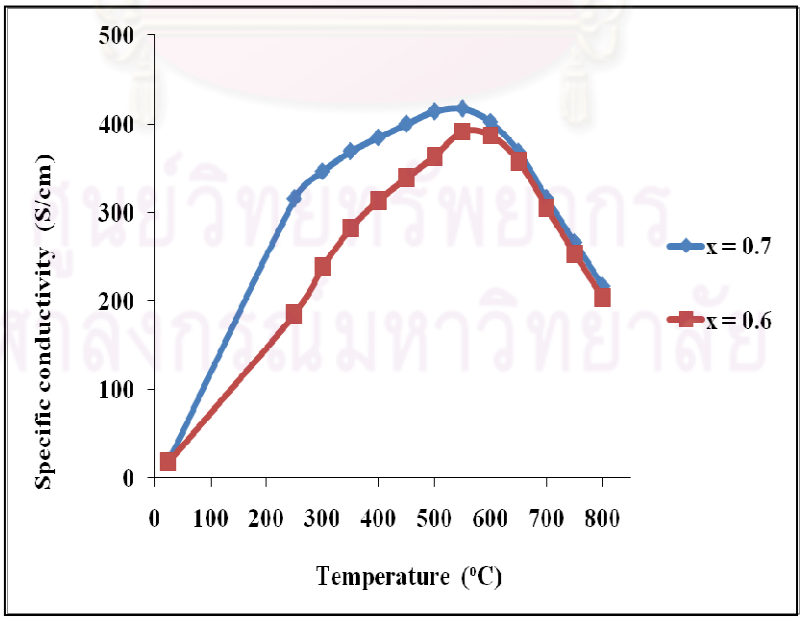

Figure 3.27 Temperature dependence of the specific conductivity (σ) for $La_{1-x}Sr_xFeO_{3-\delta}$ (x = 0.6 and 0.7).

Table 3.11 Maximum specific conductivity of $La_{1-x}Sr_xFeO_{3-\delta}$ (x = 0.3-0.7).

Ratio	Maximum specific conductivity ($S.cm^{-1}$)	Temperature (°C)
x = 0.3	151*	800*
x = 0.4	212*	800*
x = 0.5	325*	650*
x = 0.6	391	550
x = 0.7	417	550

*****from Aunpajsuda's thesis

Figure 3.27 shows a semi-conducting behavior between 25-550°C and metallic property at higher temperature. However, the conductivity value of $La_{1-x}Sr_xFeO_{3-\delta}$ materials was enhanced by doping Sr at A-site. As displayed in Figure 3.27 and Table 3.11, the specific conductivity of $La_{0.3}Sr_{0.7}FeO_{3-\delta}$ reached the maximum value of 417 S/cm at about 550°C.

In Table 3.11, when x increases, the value of maximum specific conductivity increases whereas the temperature at maximum specific conductivity decreases from 800 to 550°C. In order to discuss the possible responses of an oxide system, two extremes need to be considered on the introduction of the dopants (Sr^{2+}). The formation of oxygen vacancies occur when the oxidation state of the iron cations (+3) remains unchanged. Electronic compensation involves only a change of the oxidation state of iron cations from +3 to +4, which may be interpreted as an appearance of electron holes associated with Fe^{4+} cations [37]. Since the partial replacement of La by Sr affects the formation of both oxygen vacancies ($[VO^{\bullet\bullet}]$) and Fe^{4+} ($[Fe_{Fe}\bullet]$).

The assumption can be made that the electronic conduction is caused by the exchange of electron holes between Fe ions of different valence states, where the concentration of oxygen vacancies is always relatively small. It can be suggested that the addition of Sr into La sites increases the *p*-type conductivity.

The Arrhenius plot of $La_{0.3}Sr_{0.7}FeO_{3-\delta}$ (x = 0.6 and 0.7) is given in Figure 3.28. Its linear part can be described by the formula:

$$\sigma = (A/T) \exp(-Ea/kT) \qquad (3.1)$$

where *A* is material constant including the carrier concentration term, *E*a is the activation energy, *k* is the Boltzmann's constant and *T* is the absolute temperature. The activation energy calculated from the linear part of Arrhenius plot (Figure 3.28) is listed in Table 3.12. It can be clearly seen that the activation energy of $La_{0.3}Sr_{0.7}FeO_{3-\delta}$ decreased with the increase of the Sr content. According to these results, $La_{0.3}Sr_{0.7}FeO_{3-\delta}$ showed the lowest activation energy, corresponding to the highest specific conductivity.

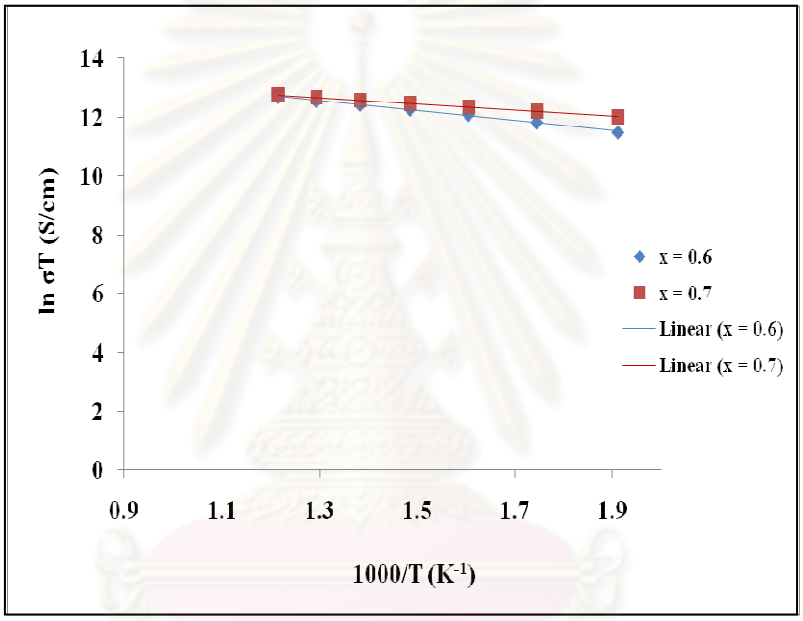

Figure 3.28 Arrhenius plot of the electrical conductivity of $La_{1-x}Sr_xFeO_{3-\delta}$ (x = 0.6 and 0.7).

Table 3.12 Activation energy of $La_{1-x}Sr_xFeO_{3-\delta}$ (x = 0.6 and 0.7).

Ratio	**E_a (kJ/mol)**
x = 0.6	10.98
x = 0.7	9.77

3.3.1.2 Electrical conductivity of $La_{0.8}Sr_{0.2}Co_{1-x}Fe_xO_{3-\delta}$ (x = 0.1 and 0.2)

The temperature dependence of the electrical conductivities of the $La_{0.8}Sr_{0.2}Co_{1-x}Fe_xO_{3-\delta}$ (x = 0.1 and 0.2) are shown in Figure 3.29 and Table 3.13.

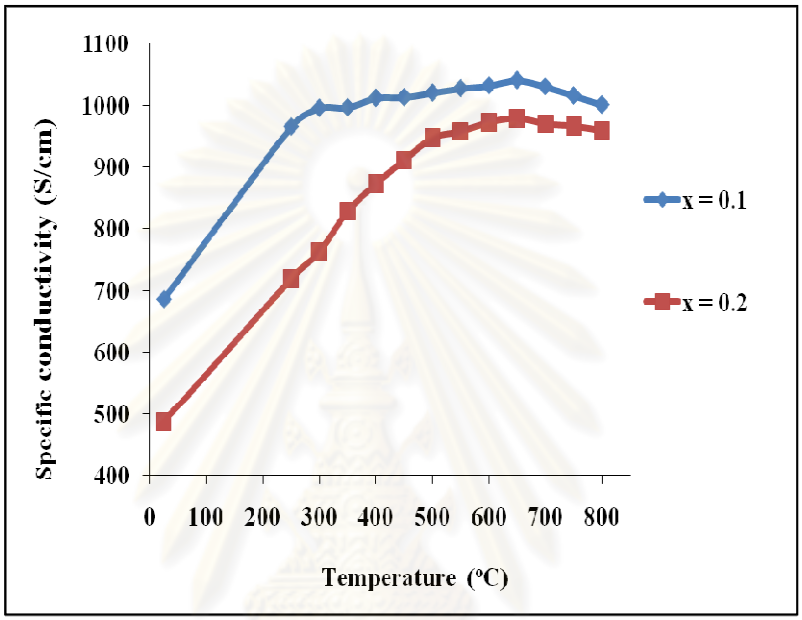

Figure 3.29 Temperature dependence of the specific conductivity (σ) for $La_{0.8}Sr_{0.2}Co_{1-x}Fe_xO_{3-\delta}$ (x = 0.1 and 0.2).

Table 3.13 Maximum specific conductivity of $La_{0.8}Sr_{0.2}Co_{1-x}Fe_xO_{3-\delta}$ (x = 0.0-0.5).

Ratio	Maximum specific conductivity ($S.cm^{-1}$)	Temperature (°C)
x = 0.0	~ 1,610*	200*
x = 0.1	1,040 1,000	650 800
x = 0.2	979 959	650 800
x = 0.3	~ 775*	800*
x = 0.4	~ 450*	900*
x = 0.5	~ 300*	900*

*from reference [43]

Figure 3.29 shows the specific conductivity of $La_{0.8}Sr_{0.2}Co_{1-x}Fe_xO_{3-\delta}$ measured in air as a function of temperature. The specific conductivity of each composition increases with temperature through a maximum, then decreases. The specific conductivity of $La_{0.8}Sr_{0.2}Co_{1-x}Fe_xO_{3-\delta}$ reached the maximum value of 1,040 S/cm at about 650°C.

In Table 3.13, when x increases, the value of maximum specific conductivity increases whereas the temperature at maximum specific conductivity shifts from approximately 200 to 900°C. The electrical conductivity of LSCF decreases with increasing Fe content because oxygen vacancies are formed in these oxides, which results in a reduction in the concentration of electronic charge carriers. Because of the vacancies also can act as random traps for electrons, resulting in the decrease of the electron carrier mobility [43-44].

The activation energy of $La_{0.8}Sr_{0.2}Co_{1-x}Fe_xO_{3-\delta}$ (x = 0.1 and 0.2) specimens calculated from the linear part of Figure 3.30 are shown in Table 3.14. It can be observed that the activation energy increases with the amount of Fe, corresponding to the specific conductivity of $La_{0.8}Sr_{0.2}Co_{1-x}Fe_xO_{3-\delta}$.

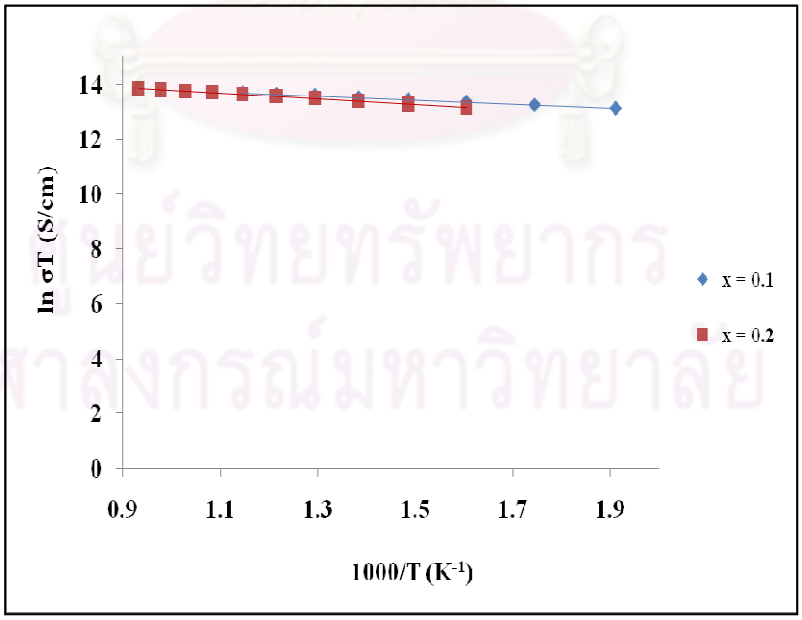

Figure 3.30 Arrhenius plot of the electrical conductivity of $La_{0.8}Sr_{0.2}Co_{1-x}Fe_xO_{3-\delta}$ (x = 0.1 and 0.2).

Table 3.14 Activation energy of $La_{0.8}Sr_{0.2}Co_{1-x}Fe_xO_{3-\delta}$ (x = 0.1 and 0.2).

Ratio	E_a (kJ/mol)
x = 0.1	6.09
x = 0.2	7.05

3.3.1.3 Electrical conductivity of LSF-LSCF composites

Figures 3.31 and 3.32 show the electrical conductivity of LSF-LSCF ceramics as a function of measuring temperature. The maximum electrical conductivity of composites with different weight ratios of LSCF are shown in Figures 3.33, 3.34 and Tables 3.15, 3.16.

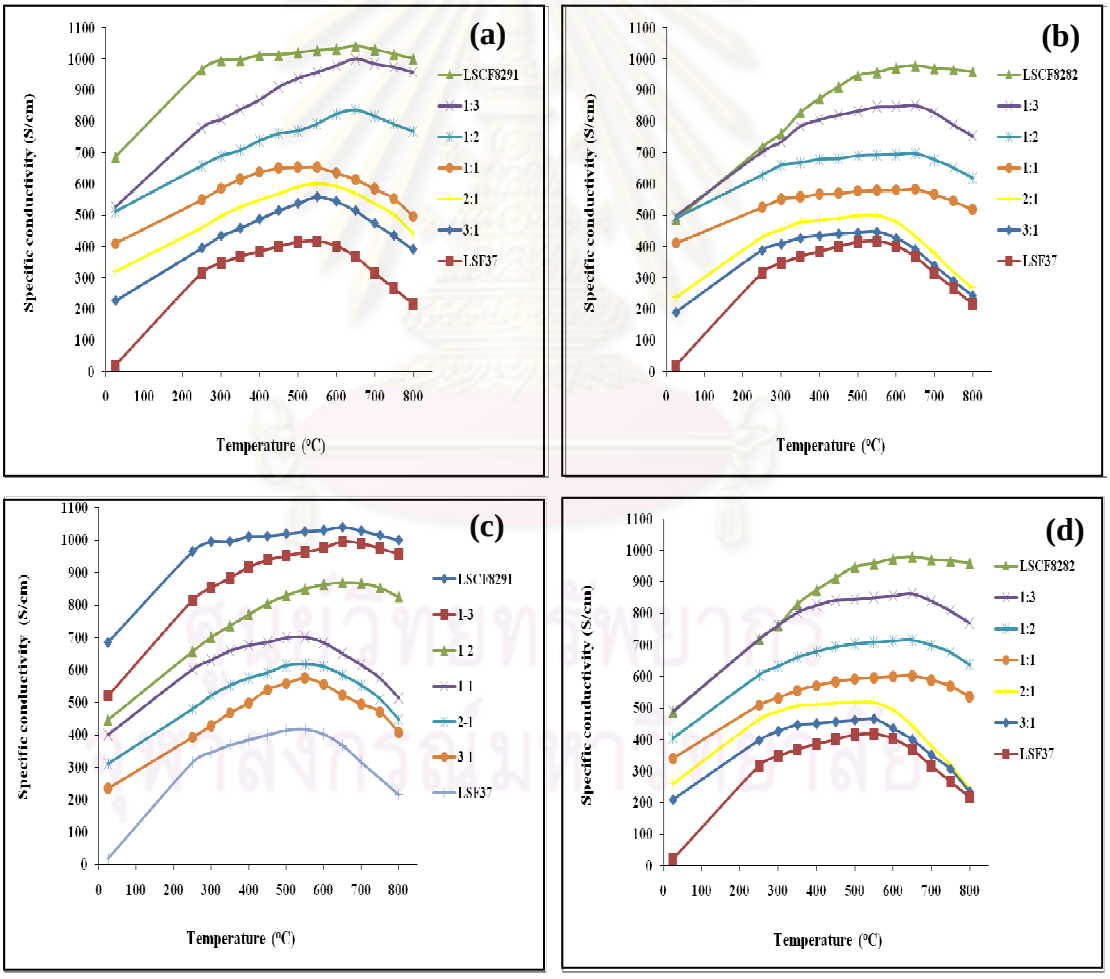

Figure 3.31 Temperature dependence of the specific conductivity (σ) for LSF-LSCF composites with different weight ratios. (a) LSF37-LSCF8291 after calcined at 800°C, (b) LSF37-LSCF8282 after calcined at 800°C, (c) LSF37-LSCF8291 after calcined at 900°C and (d) LSF37-LSCF8282 after calcined at 900°C.

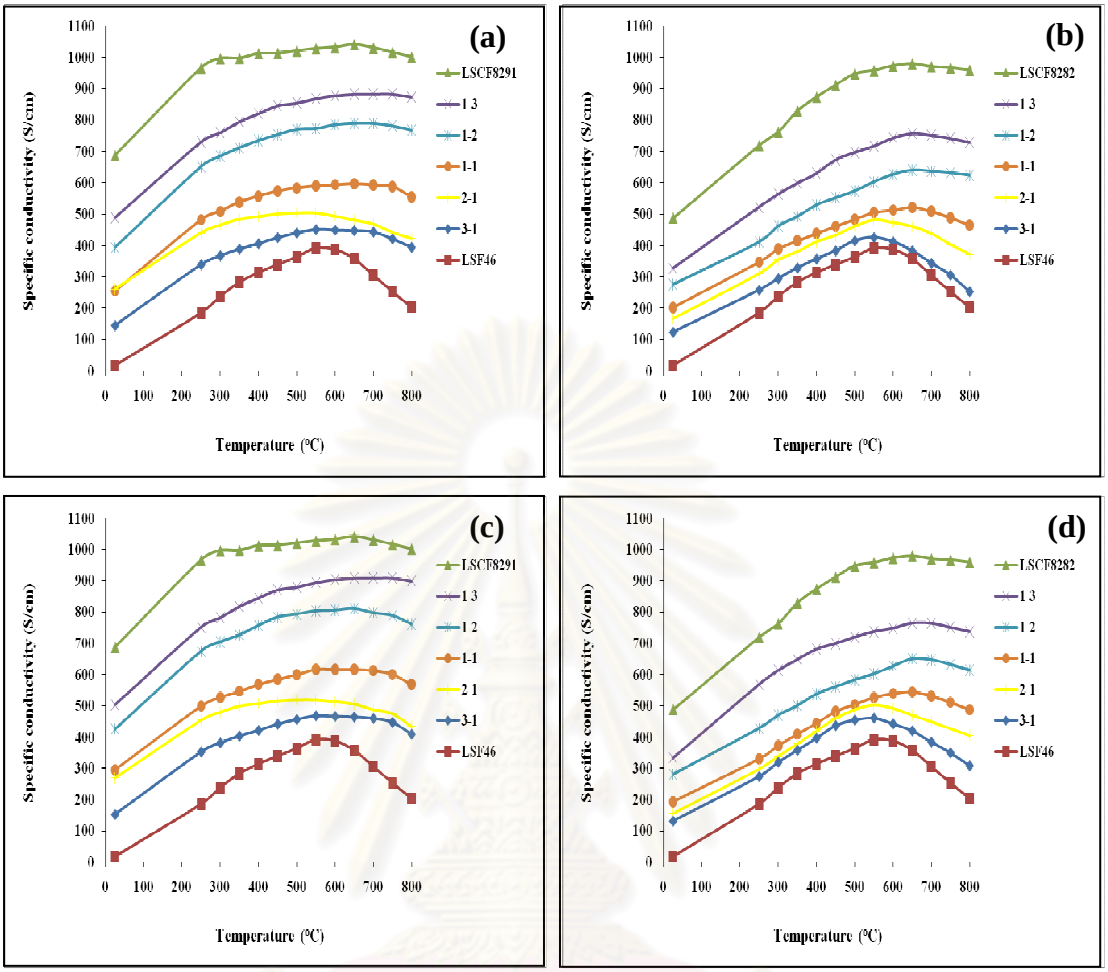

Figure 3.32 Temperature dependence of the specific conductivity (σ) for LSF-LSCF composites with different weight ratios. (a) LSF46-LSCF8291 after calcined at 800°C, (b) LSF46-LSCF8282 after calcined at 800°C, (c) LSF46-LSCF8291 after calcined at 900°C and (d) LSF46-LSCF8282 after calcined at 900°C.

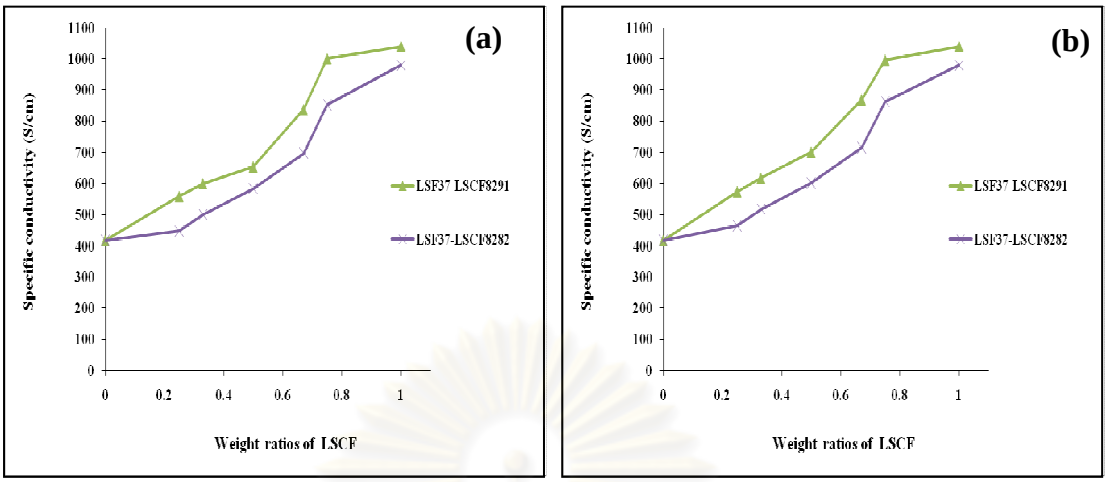

Figure 3.33 Weight ratios of LSCF dependence of the maximum specific conductivity for LSF37-LSCF8291 and LSF37-LSCF8282 composites. (a) calcined at 800^{o}C and (b) calcined at 900^{o}C.

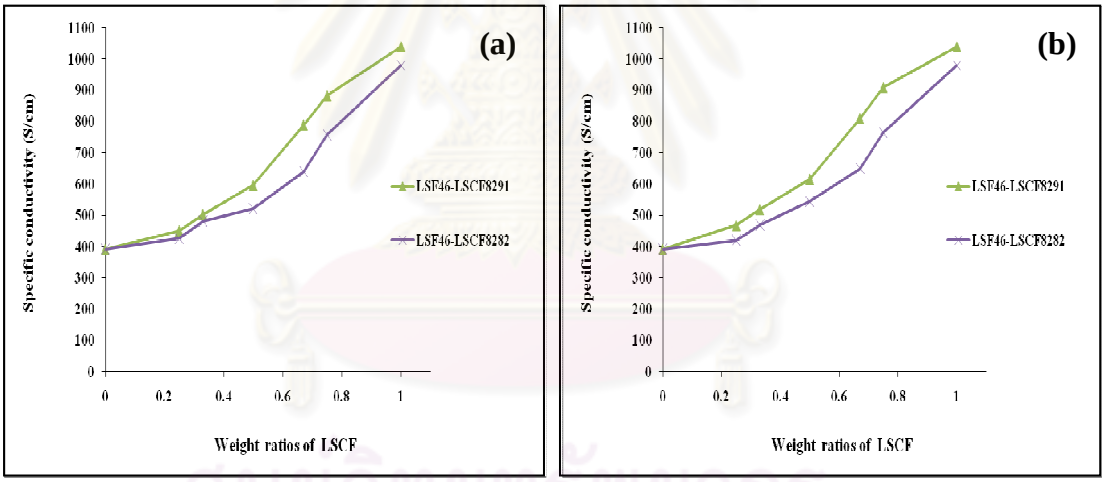

Figure 3.34 Weight ratios of LSCF dependence of the maximum specific conductivity for LSF46-LSCF8291 and LSF46-LSCF8282 composites. (a) calcined at 800^{o}C and (b) calcined at 900^{o}C.

Table 3.15 Maximum specific conductivity of LSF37-LSCF8291 and LSF37-LSCF8282 composites with different weight ratios of LSCF.

(a) Calcined at 800°C

Weight ratios of LSCF	LSF37-LSCF8291		LSF37-LSCF8282	
	Max σ (S/cm)	Temperature (°C)	Max σ (S/cm)	Temperature (°C)
0.00	417	550	417	550
0.25	559	550	447	550
0.33	600	550	500	550
0.50	654	550	584	650
0.67	837	650	697	650
0.75	1,000	650	852	650
1.00	1,040	650	979	650

(b) Calcined at 900°C

Weight ratios of LSCF	LSF37-LSCF8291		LSF37-LSCF8282	
	Max σ (S/cm)	Temperature (°C)	Max σ (S/cm)	Temperature (°C)
0.00	417	550	417	550
0.25	574	550	464	550
0.33	617	550	517	550
0.50	701	550	601	650
0.67	869	650	715	650
0.75	996	650	862	650
1.00	1,040	650	979	650

Table 3.16 Maximum specific conductivity of LSF46-LSCF8291 and LSF46-LSCF8282 composites with different weight ratios of LSCF.

(a) Calcined at 800°C

Weight ratios of LSCF	LSF46-LSCF8291		LSF46-LSCF8282	
	Max σ (S/cm)	Temperature (°C)	Max σ (S/cm)	Temperature (°C)
0.00	391	550	391	550
0.25	450	550	425	550
0.33	503	550	480	550
0.50	596	650	521	650
0.67	789	650	639	650
0.75	882	650	756	650
1.00	1,040	650	979	650

(b) Calcined at 900°C

Weight ratios of LSCF	LSF46-LSCF8291		LSF46-LSCF8282	
	Max σ (S/cm)	Temperature (°C)	Max σ (S/cm)	Temperature (°C)
0.00	391	550	391	550
0.25	468	550	461	550
0.33	518	550	502	550
0.50	616	650	544	650
0.67	810	650	650	650
0.75	908	650	764	650
1.00	1,040	650	979	650

Figures 3.31 and 3.32 show a semi-conducting behavior between 25-650°C and metallic property at higher temperature. It was found that the conductivities of all composite materials increase with an increase of temperature at about 650°C and begins to decrease. Figures 3.33, 3.34 and Tables 3.15, 3.16 show the conductivity of the composites with different weight ratios of LSCF after sinterd at 1,300°C for 10 hours in air. The data show that there is a dramatic increase in the conductivity of the composites when the content of LSCF increases. LSF-LSCF in a weight ratio 1:3 shows the highest conductivity which is higher than LSF but lower than LSCF. This suggests that electronic transport in the composites is determined by the property of LSCF based solid solution. Mixing a good mixed ionic-electronic

conductor LSCF with LSF causes the conductivity of LSF to improve. Moreover, LSF37-LSCF8291 (1:3) (1,000 S/cm) shows higher conductivity than LSF37-LSCF8282 (1:3) (852 S/cm) and the LSF46-LSCF8291 (1:3) (882 S/cm) shows higher conductivity than the LSF46-LSCF8282 (1:3) (756 S/cm) too. It is possible that the addition of LSCF8282 might increase the amount of Fe from 10% to 20% in the LSF-LSCF8282 composite, which results in a formation of oxygen vacancies. The vacancies also can act as random traps for electrons. The conductivity of composites after calcined at 800 and 900^{o}C do not differ significantly (< 50 S/cm). The study of the effect of sintering temperature for 10 hours, the samples in a weight ratio of 1:3 after calcined at 800^{o}C were used.

The activation energy values of LSF-LSCF composites calculated from the linear part of Figures 3.35 and 3.36 are shown in Tables 3.17 and 3.18. It is observed that the activation energy decreases with the amount of LSCF. Moreover, LSF-LSCF8291 shows lower activation energy than LSF-LSCF8282, corresponding to the specific conductivity.

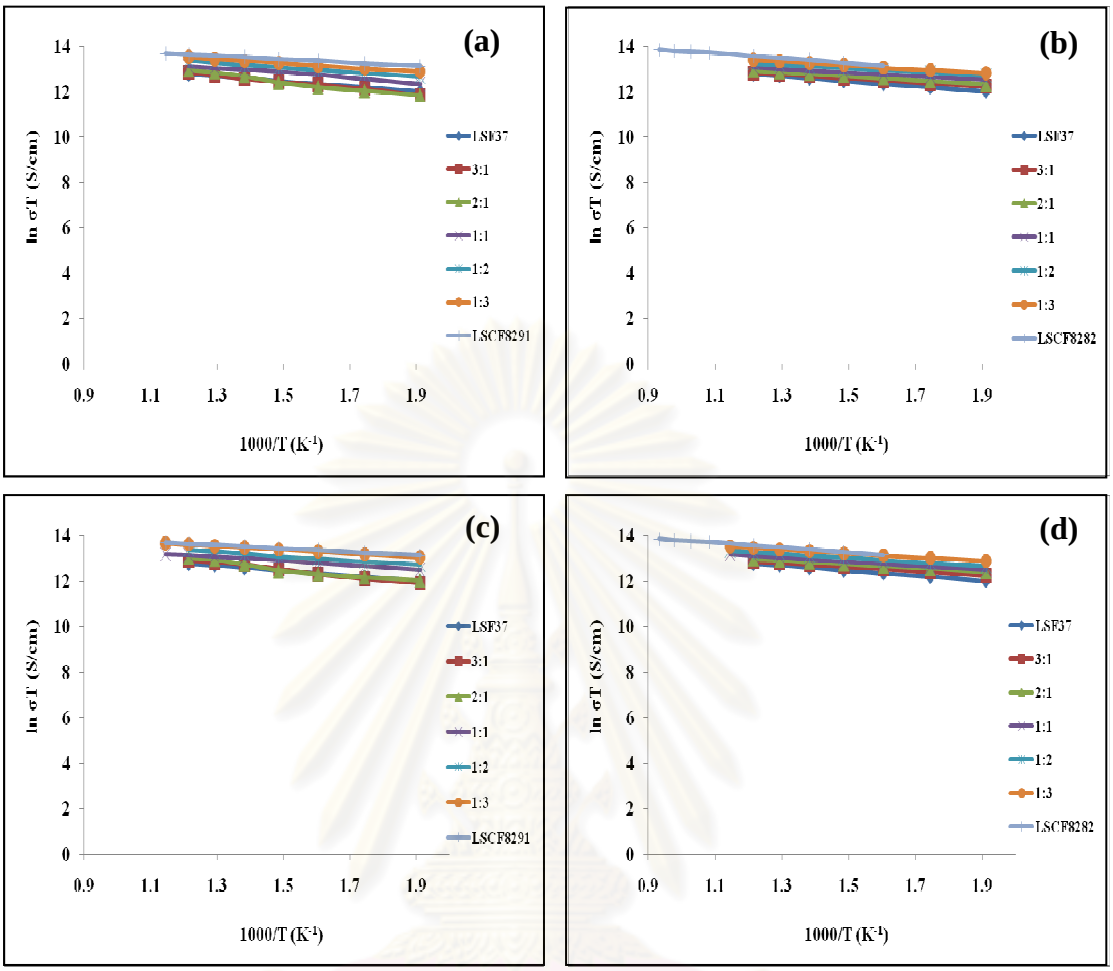

Figure 3.35 Arrhenius plots of the electrical conductivity of LSF-LSCF composites with different weight ratios. (a) LSF37-LSCF8291 after calcined at 800°C, (b) LSF37-LSCF8282 after calcined at 800°C, (c) LSF37-LSCF8291 after calcined at 900°C and (d) LSF37-LSCF8282 after calcined at 900°C.

Table 3.17 Activation energy of LSF37-LSCF8291 and LSF37-LSCF8282 composites with different weight ratios of LSCF.

(a) Calcined at 800°C

Weight ratios of LSCF	LSF37-LSCF8291	LSF37-LSCF8282
	E_a (kJ/mol)	E_a (kJ/mol)
0.00	9.77	9.77
0.25	7.18	8.54
0.33	7.08	8.36
0.50	6.94	8.13
0.67	6.67	7.52
0.75	6.27	7.30
1.00	6.09	7.05

(b) Calcined at 900°C

Weight ratios of LSCF	LSF37-LSCF8291	LSF37-LSCF8282
	E_a (kJ/mol)	E_a (kJ/mol)
0.00	9.77	9.77
0.25	7.08	8.62
0.33	6.98	8.25
0.50	6.86	7.96
0.67	6.60	7.40
0.75	6.33	7.21
1.00	6.09	7.05

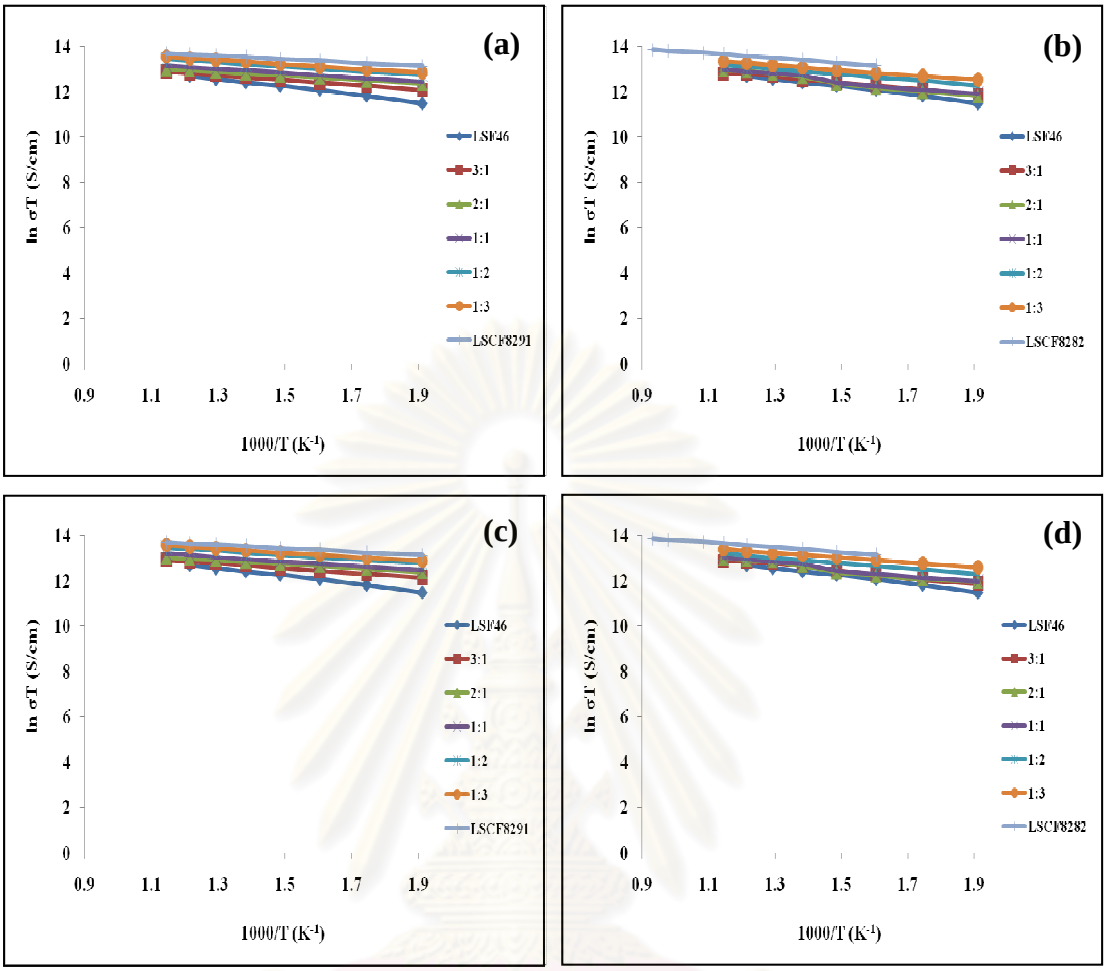

Figure 3.36 Arrhenius plots of the electrical conductivity of LSF-LSCF composites with different weight ratios. (a) LSF46-LSCF8291 after calcined at 800°C, (b) LSF46-LSCF8282 after calcined at 800°C, (c) LSF46-LSCF8291 after calcined at 900°C and (d) LSF46-LSCF8282 after calcined at 900°C.

Table 3.18 Activation energy of LSF46-LSCF8291 and LSF46-LSCF8282 composites with different weight ratios of LSCF.

(a) Calcined at 800°C

Weight ratios of LSCF	LSF46-LSCF8291	LSF46-LSCF8282
	E_a (kJ/mol)	E_a (kJ/mol)
0.00	10.98	10.98
0.25	8.41	9.22
0.33	7.87	9.05
0.50	7.62	8.58
0.67	7.39	8.30
0.75	6.87	8.05
1.00	6.09	7.05

(b) Calcined at 900°C

Weight ratios of LSCF	LSF46-LSCF8291	LSF46-LSCF8282
	E_a (kJ/mol)	E_a (kJ/mol)
0.00	10.98	10.98
0.25	8.34	8.96
0.33	7.73	8.78
0.50	7.52	8.28
0.67	7.20	8.04
0.75	6.69	7.85
1.00	6.09	7.05

The temperature dependence of the electrical conductivities of LSF-LSCF composites in a weight ratio of 1:3 after calcined at 800°C with different sintering temperatures for 10 hours were exhibited in Figure 3.37. The maximum electrical conductivity of composites with different sintering temperatures for 10 hours are shown in Figure 3.38 and Table 3.19.

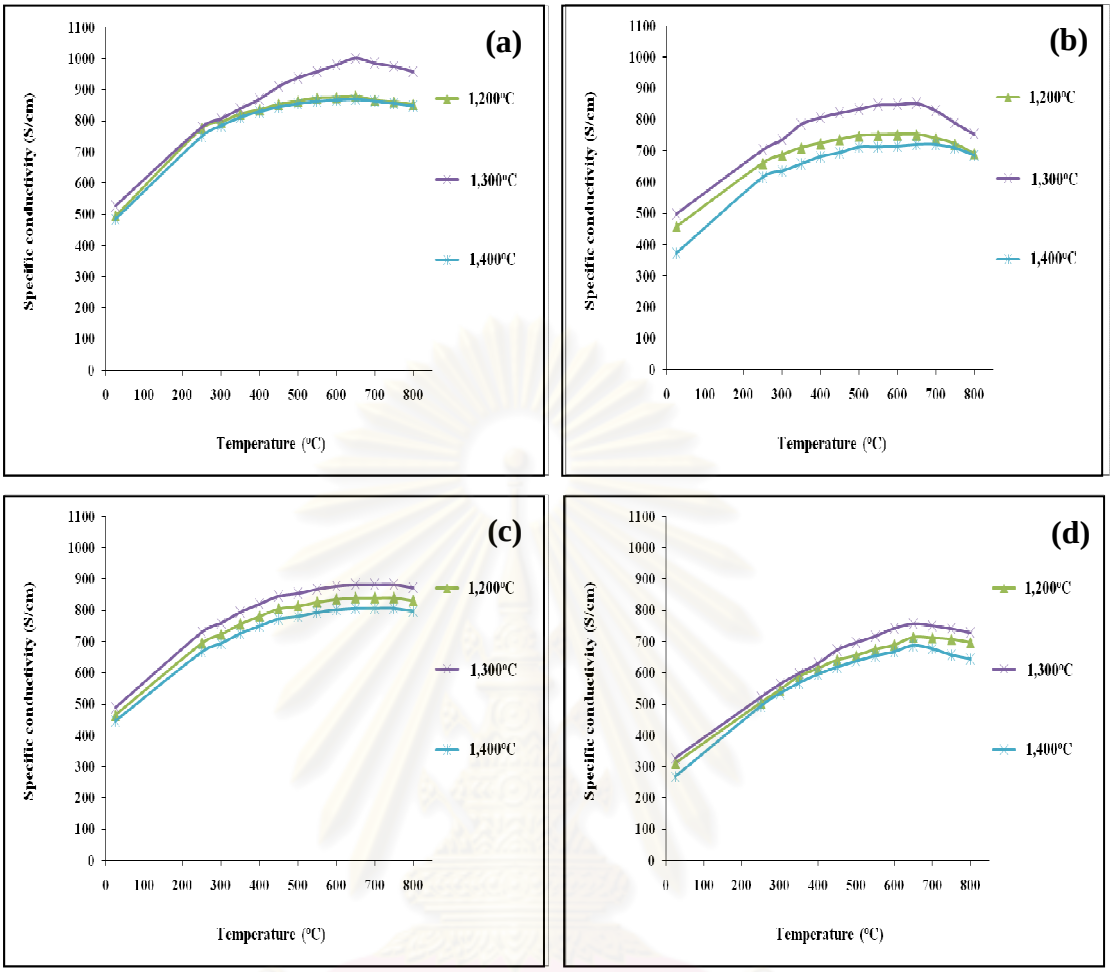

Figure 3.37 Temperature dependence of the specific conductivity (σ) for LSF-LSCF composites in a weight ratio of 1:3 after calcined at 800°C with different sintering temperatures for 10 hours. (a) LSF37-LSCF8291, (b) LSF37-LSCF8282, (c) LSF46-LSCF8291 and (d) LSF46-LSCF8282.

Figure 3.37 shows a semi-conducting behavior for all composite materials. It is found that the conductivities of all composite materials increase with an increase of temperature at about 650°C and begin to decrease. Figure 3.38 and Table 3.19 show the maximum conductivity of the composite in a weight ratio of 1:3 after calcined at 800°C as a function of sintering temperature. The data show that there is a dramatic increase in the conductivity of the composites after increasing the sintering temperature from 1,200 to 1,300°C but decreased when the temperature was raised to 1400°C. The influence of sintering temperature on the value of conductivity

most likely should be attributed to the density of LSF-LSCF composite, which influence the grain to grain connection.

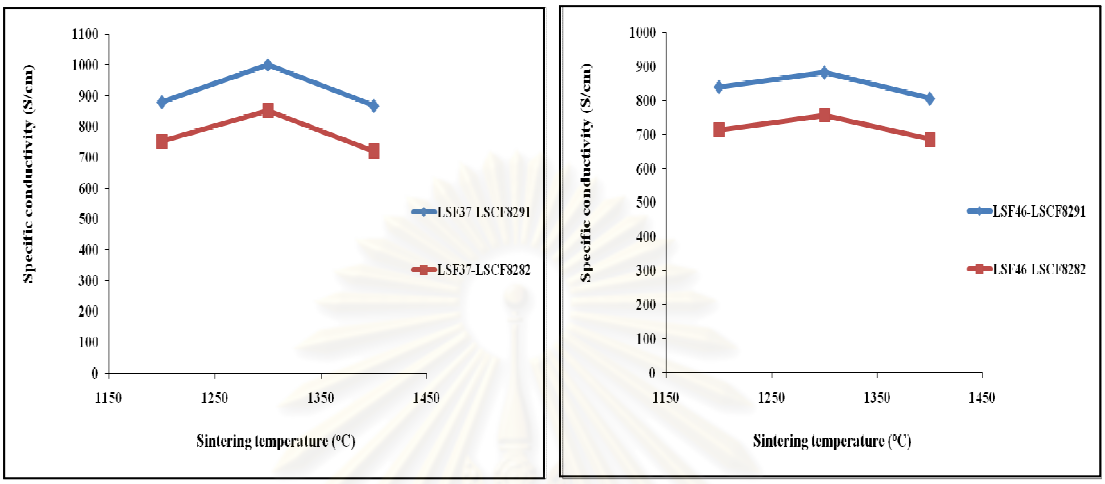

Figure 3.38 Sintering temperature dependence of the maximum specific conductivity for LSF-LSCF composites in a weight ratio of 1:3 for 10 hours.

Table 3.19 Maximum specific conductivity of LSF-LSCF composites in a weight ratio of 1:3 after calcined at 800°C with different sintering temperatures for 10 hours.

Sintering temperature (°C)	LSF37-LSCF8291		LSF37-LSCF8282	
	Max σ (S/cm)	Temperature (°C)	Max σ (S/cm)	Temperature (°C)
1,200	879	650	752	650
1,300	1,000	650	852	650
1,400	867	650	720	650

Sintering temperature (°C)	LSF46-LSCF8291		LSF46-LSCF8282	
	Max σ (S/cm)	Temperature (°C)	Max σ (S/cm)	Temperature (°C)
1,200	840	650	714	650
1,300	882	650	756	650
1,400	806	650	686	650

Shown in Table 3.20, the activation energy values of LSF-LSCF composites in a weight ratio of 1:3 after calcined at 800°C with different sintering temperature were calculated from the linear part of Figure 3.39.

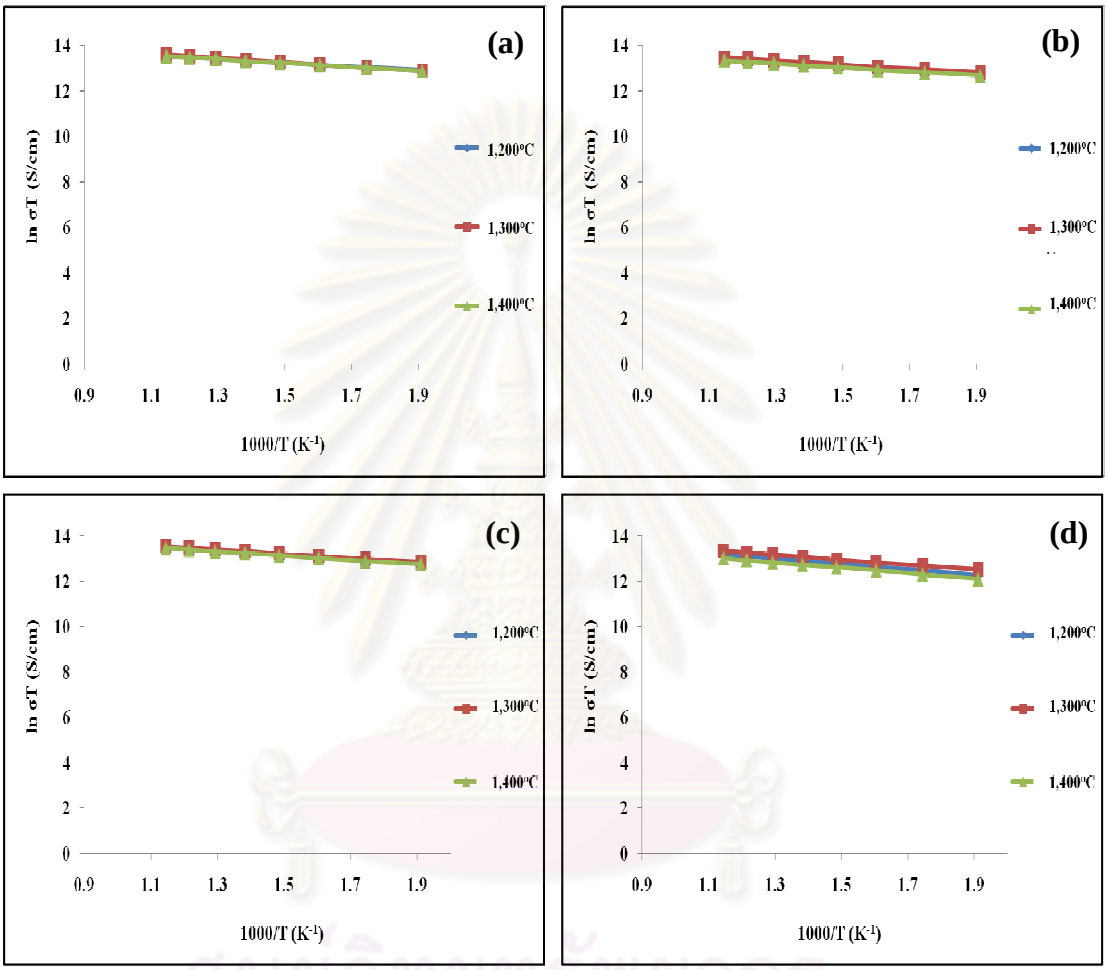

Figure 3.39 Arrhenius plots of the electrical conductivity of LSF-LSCF composites in a weight ratio of 1:3 after calcined at 800°C with different sintering temperature for 10 hours. (a) LSF37-LSCF8291, (b) LSF37-LSCF8282, (c) LSF46-LSCF8291 and (d) LSF46-LSCF8282.

.

Table 3.20 Activation energy of LSF-LSCF composites in a weight ratio of 1:3 after calcined at 800°C with different sintering temperature for 10 hours.

Sintering temperature (°C)	LSF37-LSCF8291	LSF37-LSCF8282
	E_a (kJ/mol)	E_a (kJ/mol)
1,200	6.58	7.54
1,300	6.27	7.30
1,400	6.74	7.73

Sintering temperature (°C)	LSF46-LSCF8291	LSF46-LSCF8282
	E_a (kJ/mol)	E_a (kJ/mol)
1,200	7.18	8.44
1,300	6.87	8.05
1,400	7.52	8.61

According to these results, the sintering temperature at 1,300°C showed the lowest activation energy, corresponding to the highest specific conductivity. It is concluded that the suitable sintering temperature is 1,300°C.

Figure 3.40 shows the temperature dependence of specific conductivity of LSF-LSCF composites in a weight ratio of 1:3 after calcined at 800°C with different sintering time for sintered at 1,300°C. Figure 3.41 and Table 3.21 show the maximum specific conductivity of composites with different sintering time for sintered at 1,300°C.

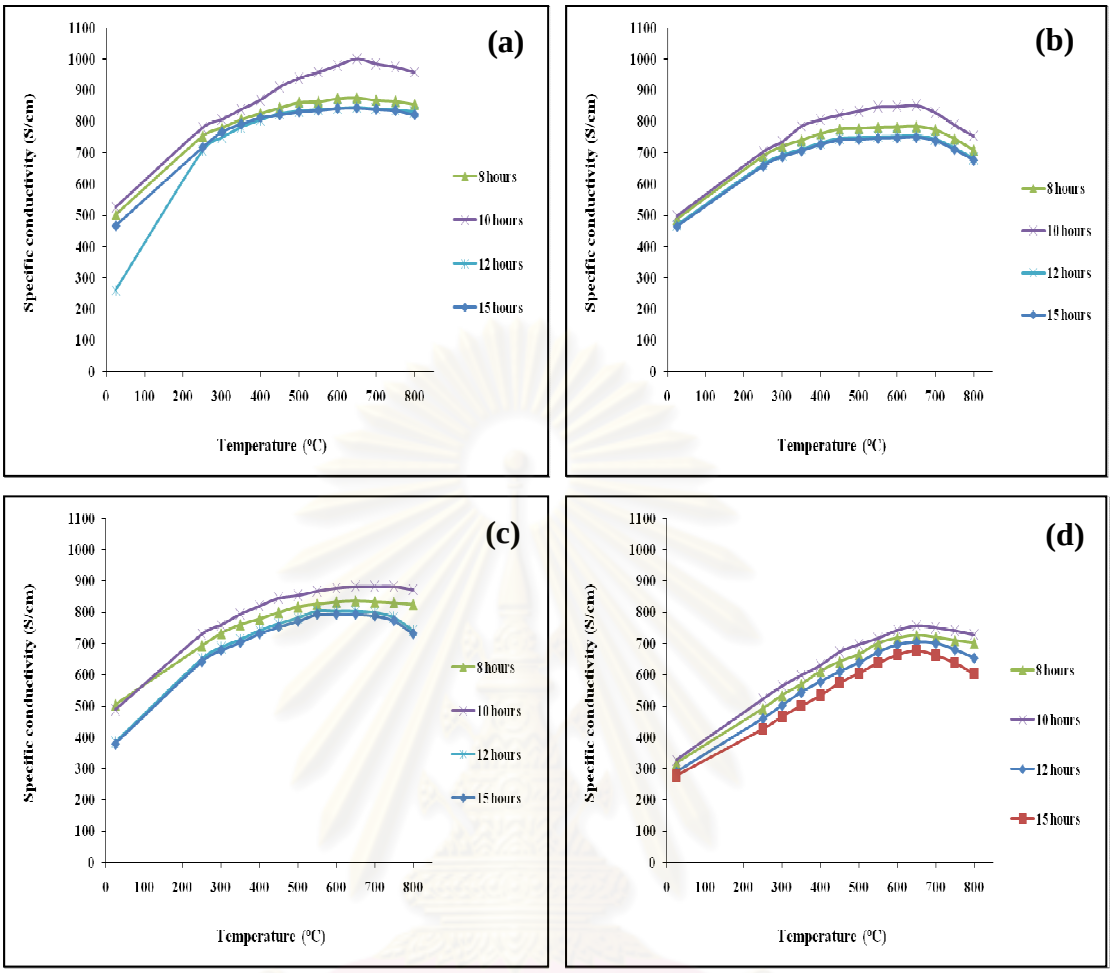

Figure 3.40 Temperature dependence of the specific conductivity (σ) for LSF-LSCF composites in a weight ratio of 1:3 after calcined at 800°C with different sintering time for sintered at 1,300°C. (a) LSF37-LSCF8291, (b) LSF37-LSCF8282, (c) LSF46-LSCF8291 and (d) LSF46-LSCF8282.

Figure 3.40 shows two regions of conductivity. In the lower temperature region (at room temperature to 650 °C), the composite materials are semi-conductor while these perovskites show metallic conductivity at higher temperature region. Figure 3.41 and Table 3.21 summarize the specific conductivity as a function of sintering time for the composite in a weight ratio of 1:3 for sinterd at 1,300°C. The data show that there is a dramatic increase in the conductivity of the composites after increasing the sintering time from 8 to 10 hours but decreased when sintered for 12 and 15 hours, suggesting the highest relative density when sintered for 10 hours.

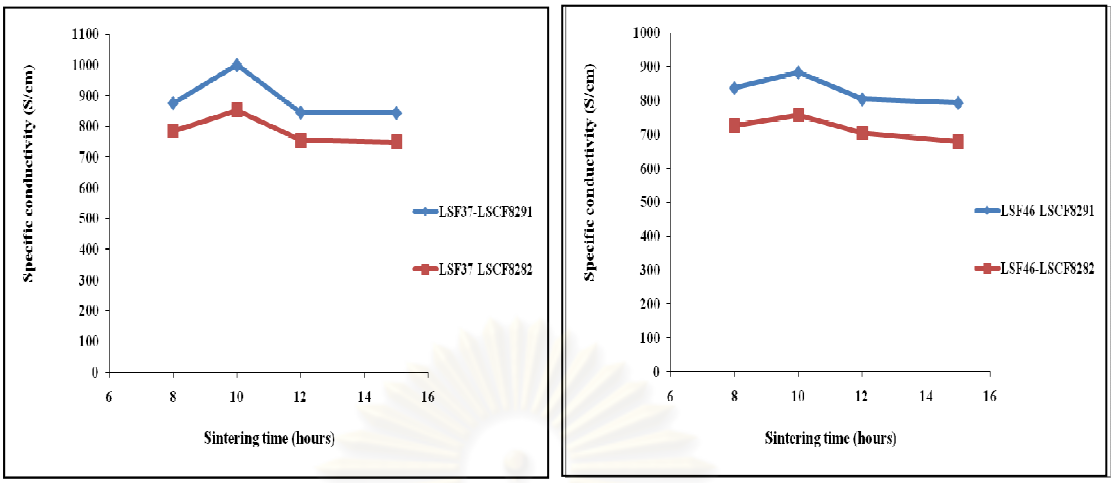

Figure 3.41 Sintering time dependence of the maximum specific conductivity for LSF-LSCF composites in a weight ratio of 1:3 for sintered at 1,300°C.

Table 3.21 Maximum specific conductivity of LSF-LSCF composites in a weight ratio of 1:3 after calcined at 800°C with different sintering time for sinterd at 1,300°C.

Sintering time (hour)	LSF37-LSCF8291		LSF37-LSCF8282	
	Max σ (S/cm)	Temperature (°C)	Max σ (S/cm)	Temperature (°C)
8	876	650	785	650
10	1,000	650	852	650
12	845	650	754	650
15	843	650	749	650

Sintering time (hour)	LSF46-LSCF8291		LSF46-LSCF8282	
	Max σ (S/cm)	Temperature (°C)	Max σ (S/cm)	Temperature (°C)
8	837	650	726	650
10	882	650	756	650
12	803	650	704	650
15	793	650	678	650

Shown in Table 3.22, the activation energy values of LSF-LSCF composites in a weight ratio of 1:3 after calcined at 800°C with different sintering time for sinterd at 1,300°C were calculated from the linear part of Figure 3.42.

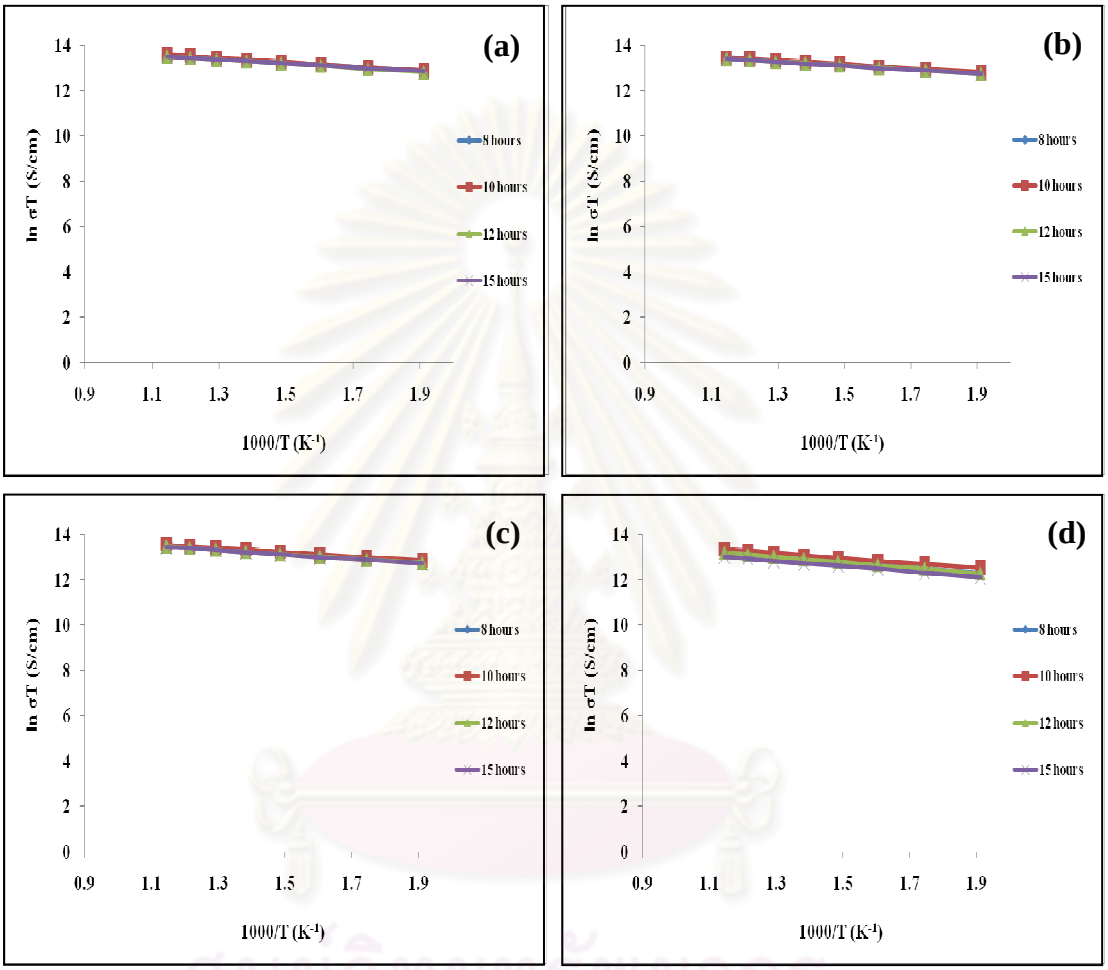

Figure 3.42 Arrhenius plots of the electrical conductivity of LSF-LSCF composites in a weight ratio of 1:3 after calcined at 800°C with different sintering time for sintered at 1,300°C. (a) LSF37-LSCF8291, (b) LSF37-LSCF8282, (c) LSF46-LSCF8291 and (d) LSF46-LSCF8282.

Table 3.22 Activation energy of LSF-LSCF composites in a weight ratio of 1:3 after calcined at 800°C with different sintering time for sintered at 1,300°C.

Sintering time (hour)	LSF37-LSCF8291	LSF37-LSCF8282
	E_a (kJ/mol)	E_a (kJ/mol)
8	6.69	7.66
10	6.27	7.30
12	6.82	7.73
15	6.90	7.83

Sintering time (hour)	LSF46-LSCF8291	LSF46-LSCF8282
	E_a (kJ/mol)	E_a (kJ/mol)
8	7.23	8.34
10	6.87	8.05
12	7.60	8.53
15	7.73	8.83

According to these results, the sintering time at 10 hours showed the lowest activation energy, corresponding to the highest specific conductivity. It is concluded that the suitable sintering time is 10 hours. In order to study the thermal expansion coefficient of the composite oxide, the samples in a weight ratio of 1:3 after calcined at 800°C and sintering at 1,300°C for 10 hours were used.

Table 3.23 shows the maximum specific conductivity of composites in a weight ratio of 1:3 after calcined at 800°C and sintered at 1,300°C for 10 hours.

Table 3.23 Maximum specific conductivity of LSF-LSCF8291 composites in a weight ratio of 1:3 after calcined at 800°C and sintered at 1,300°C for 10 hours.

Sample	Maximum specific conductivity (S/cm)	Temperature (°C)
LSF37-LSCF8291	1,000	650
LSF46-LSCF8291	882	650

From Table 3.23, it demonstrated that LSF37-LSCF8291 shows higher conductivity than LSF46-LSCF8291. It is possible that the addition of LSF37 might be increase the amount of Sr into the composite. It can be suggested that the addition of Sr into the composites increases the *p*-type conductivity.

From the conductivity results, it is concluded that mixing LSCF with LSF can improve the conductivity of LSF. In a weight ratio 1:3, the specific conductivity of LSF37-LSCF8291 shows the highest value which is 1,000 S/cm at 650^{o}C. For variation of the sintering temperature and sintering time, the composite materials sintered at 1,300^{o}C for 10 hours shows the highest conductivity. The highest specific conductivity obtained from this work is 1,000 S/cm at 650^{o}C for LSF37-LSCF8291 in a weight ratio of 1:3 after calcined at 800^{o}C and sintered at 1,300^{o}C for 10 hours. The conductivity of LSF37-LSCF8291 in this work is greater than that of 30% $La_{0.9}Sr_{0.1}Ga_{0.8}Mg_{0.2}O_{3-\delta}$ - 70% $La_{0.6}Sr_{0.4}Co_{0.2}Fe_{0.8}O_{3-\theta}$ composite cathodes (35 S/cm in air at 800°C) and 50% $La_2NiO_{4+\delta}$ - 50% $La_{0.6}Sr_{0.4}Co_{0.2}Fe_{0.8}O_{3-\delta}$ composite cathodes (230 S/cm in air at 800°C) reported by Lin and Lu, respectively [45-46].

3.3.2 Thermal expansion coefficients

Since SOFCs operate at high temperatures and should endure the thermal cycle from room temperature to operating temperature. Materials of SOFCs must be thermally compatible with the other cell components. Therefore, the thermal expansion coefficient (TEC) of materials must be close to those of the other cell components to minimize the thermal stresses.

The thermal expansions were measured by using a dilatometer (NETZSCH DIL 402C) in the temperature range from room temperature to 800°C. Measurements were performed at a heating rate of 10 °C/min and data acquisition of the differential length and the temperature was conducted every 10 seconds. No weight change of the sample was observed before and after the measurement.

3.3.2.1 Thermal expansion coefficients of $La_{1-x}Sr_xFeO_{3-\delta}$ (x = 0.6 and 0.7)

Dilatometric curves for the $La_{1-x}Sr_xFeO_{3-\delta}$ (x = 0.6 and 0.7) in air are shown in Figure 3.43. The average thermal expansion coefficient (TEC) is defined as the slope of dilatometric curves, is displayed in Table 3.24.

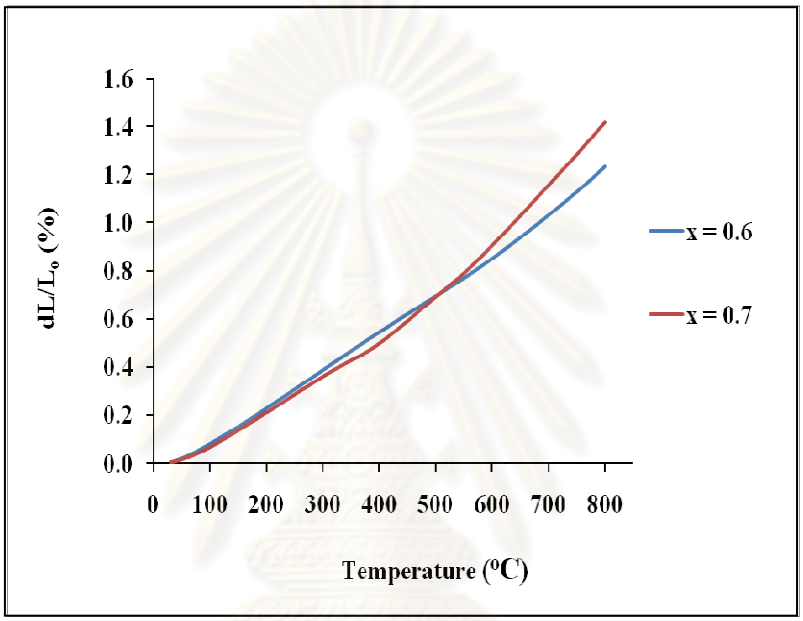

Figure 3.43 Temperature dependence of the thermal expansion for $La_{1-x}Sr_xFeO_{3-\delta}$ (x = 0.6 and 0.7).

The perovskite oxides expanded almost linearly in the temperature range 25-400°C but they became steeper at high temperature due to a loss of oxygen (i.e., the formation of oxygen vacancies) in the structure during heat-treatment [43]. The lattice expansion observed may be attributed to the loss of oxygen and the formation of oxygen vacancies. There were two reasons for the lattice expansion concerned with the formation of oxygen vacancies. Firstly, the repulsion force arising between those mutually exposed cations when oxygen ions are extracted from the lattice. Secondly, the increase in cation size due to the reduction of the valence state of iron from Fe^{4+} (r_{Fe}^{4+} = 0.585 Å) to Fe^{3+} (r_{Fe}^{3+} = 0.645 Å), which must occur concurrently with formation of oxygen vacancies in order to maintain electrical neutrality, described in equation (3.2) [38-40].

$$2Fe_{Fe}^{\bullet} + O_O^{x} \longrightarrow 2Fe_{Fe}^{x} + V_O^{\bullet\bullet} + \frac{1}{2}O_2 \quad (3.2)$$

The result of these chemical-induced mechanisms is a deformation and an increase of the unit cell volume [41]. Therefore, thermal reduction of Fe^{4+} to Fe^{3+} and the formation of oxygen vacancies enhanced the thermal expansion coefficient. From Table 3.24, it is seen that the thermal expansion coefficient increases with increasing value of x, due to the higher concentration of oxygen vacancies in the samples with more Sr.

Table 3.24 The TEC values of $La_{1-x}Sr_xFeO_3$ (x = 0.6 and 0.7).

Ratio	**TEC (x 10^{-6} $^oC^{-1}$)**
x = 0.6	14.95
x = 0.7	15.02

3.3.2.2 Thermal expansion coefficients of $La_{0.8}Sr_{0.2}Co_{1-x}Fe_xO_{3-\delta}$ (x = 0.1 and 0.2)

Dilatometric curves for the $La_{0.8}Sr_{0.2}Co_{1-x}Fe_xO_{3-\delta}$ (x = 0.1 and 0.2) in air are shown in Figure 3.44. The average thermal expansion coefficient (TEC) is defined as the slope of dilatometric curves, is displayed in Table 3.25.

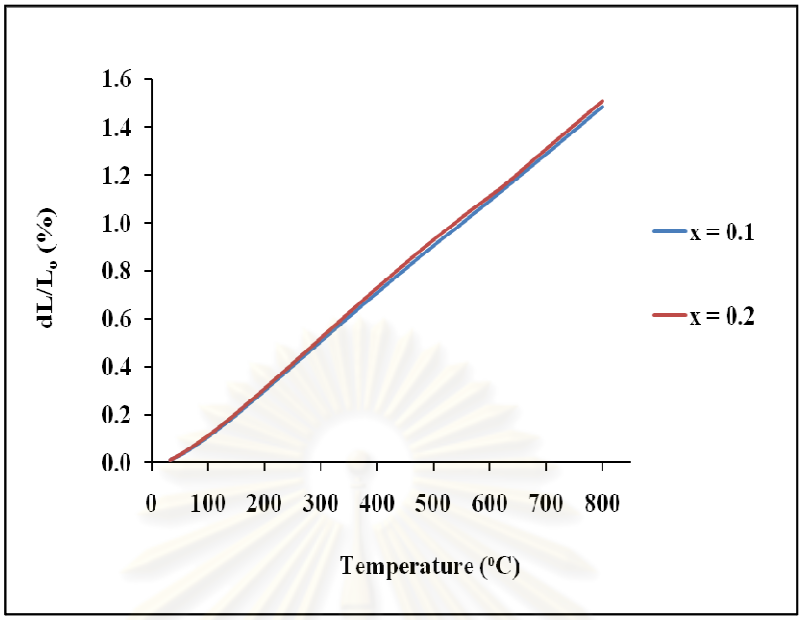

Figure 3.44 Temperature dependence of the thermal expansion for $La_{0.8}Sr_{0.2}Co_{1-x}Fe_xO_{3-\delta}$ (x = 0.1 and 0.2).

Thermal expansion curves in Figure 3.44 show gradual increases in the high temperature region for all compositions. The observed inflection of the curves is thought to be due to a loss of oxygen (i.e., the formation of oxygen vacancies) in the LSCF structure during heat-treatment, and this phenomenon might be associated with the reduction of the valence state of Co and Fe for compensating the charge neutrality of the crystal by the formation of oxygen vacancies [43]. From Table 3.25, it is seen that the thermal expansion coefficient increases with increasing value of x, due to the higher concentration of oxygen vacancies in the samples with more Fe.

Table 3.25 The TEC values of $La_{0.8}Sr_{0.2}Co_{1-x}Fe_xO_{3-\delta}$ (x = 0.0-0.2).

Ratio	TEC (x 10^{-6} $^oC^{-1}$)	Reference
x = 0.0	19.70	[43]
x = 0.1	19.47	This work
	20.10	[43]
x = 0.2	20.01	This work
	20.70	[43]

3.3.2.3 Thermal expansion coefficients of LSF-LSCF composites

The average thermal expansion coefficient (TEC) of LSF-LSCF composites in a weight ratio of 1:3 after calcined at 800°C and sintered at 1,300°C for 10 hours (the highest specific conductivity) in air, obtained from dilatometric curves (Figure 3.45) are showed in Table 3.26

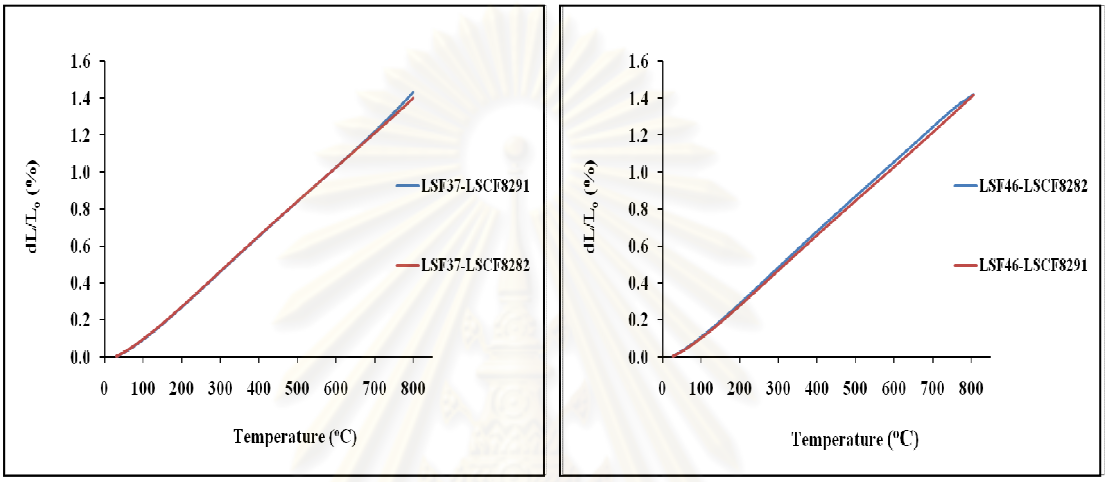

Figure 3.45 Temperature dependence of the thermal expansion for LSF-LSCF composites in a weight ratio of 1:3 after calcined at 800°C and sintered at 1,300°C for 10 hours.

Table 3.26 The TEC values of LSF-LSCF composites in a weight ratio of 1:3 after calcined at 800°C and sintered at 1,300°C for 10 hours.

Sample	TEC (x 10^{-6} °C^{-1})	Sample	TEC (x 10^{-6} °C^{-1})
LSF37	15.02	LSF46	14.95
LSF37-LSCF8291	18.15	LSF46-LSCF8291	18.10
LSF37-LSCF8282	18.70	LSF46-LSCF8282	18.40
LSCF8291	19.47	LSCF8291	19.47
LSCF8282	20.01	LSCF8282	20.01

It can be seen that mixing LSF with LSCF reduces the thermal expansion coefficient values as compared with LSCF but higher than LSF. This manifests a remarkable advantage of the composite design. In addition, mixing LSF

with LSCF8291 reduces the TEC values more than mixing LSF with LSCF8282, due to the concentration of oxygen vacancies in LSCF8282 higher than LSCF8291.

Table 3.27 shows the TEC values of LSF-LSCF8291 composites in a weight ratio of 1:3 after calcined at 800^{o}C and sintered at 1,300^{o}C for 10 hours.

Table 3.27 The TEC values of LSF-LSCF8291 composites in a weight ratio of 1:3 after calcined at 800^{o}C and sintered at 1,300^{o}C for 10 hours.

Sample	**TEC (x 10^{-6} $^{o}C^{-1}$)**
LSF37-LSCF8291	18.15
LSF46-LSCF8291	18.10

The data showed that the TEC values of LSF46-LSCF8291 lower than that of LSF37-LSCF8291. It is possible that the higher amount of Sr in LSF37 might increase the concentration of oxygen vacancies in the composites.

From the results of thermal expansion property, it is concluded that mixing LSF with LSCF can reduce the thermal expansion of LSCF but still greater than TEC value of ~ 12.5 x 10^{-6} $^{\circ}C^{-1}$ for gadolinium-doped ceria (GDC) and yttria-stabilised zirconia (~ 10.7 x 10^{-6} $^{\circ}C^{-1}$) electrolyte. The lowest thermal expansion coefficient obtained from this work is 18.10 x 10^{-6} $^{o}C^{-1}$ for LSF46-LSCF8291.

CHAPTER IV

CONCLUSIONS

4.1 Conclusions

$La_{1-x}Sr_xFeO_{3-\delta}$ (x = 0.6 and 0.7)-$La_{0.8}Sr_{0.2}Co_{1-x}Fe_xO_{3-\delta}$ (x = 0.1 and 0.2) composite cathodes were prepared by physical mixing method in various weight ratios, calcination temperature, sintering temperature and sintering time. The X-ray results indicated all composites showed single-phase of ABO_3 perovskite oxides and the optimum calcinations of the mixture are 800^{o}C and 900^{o}C.

Moreover, the XRD analysis indicated that sintering temperature affected on the lattice parameter of the composites. With the increasing of temperature, the lattice parameter increased. It was likely that the electrostatic repulsion between the cations via the formation of oxygen vacancies caused the expansion of lattice parameter. Therefore, the lattice parameter of the composites did not change significantly when increasing the sintering time.

Surface morphology of the sintered discs was examined by SEM. SEM characterization concluded that each sample exhibited high density (more than 92%) with homogeneous surface. The grain sizes of composites increased with increasing the amount of LSCF and the sintering temperature, but decreased with increasing the sintering time.

From the conductivity results, the increase of LSCF content results in an increase the electrical conductivity of the composites. This suggests that electronic transport in the composites is determined by the property of LSCF based solid solution. Mixing a good mixed ionic-electronic conductor LSCF with LSF causes the conductivity of LSF to improve. LSF37-LSCF8291 in a weight ratio of 1:3 shows the highest conductivity which is 1,000 S/cm at 650^{o}C. For variation of the sintering temperature, it was revealed that the conductivity of composites increased when the temperature was raised from 1,200 to 1,300^{o}C, but decreased when the temperature was raised to 1400^{o}C. In case of sintering time, the conductivity increased with increasing the sintering time from 8 to 10 hours and then decreased when the sintering

time was raised to 12 hours. The specific conductivity of 1,000 S/cm for LSF37-LSCF8291 in a weight ratio of 1:3 after calcined at 800^{o}C and sintered at 1,300^{o}C for 10 hours, at intermediate temperature (650°C) was obtained in this work.

The thermal expansion values proved that mixing LSF with LSCF is significant to reduce the thermal expansion coefficients of LSCF. The lowest thermal expansion coefficient obtained from this work is 18.10 x 10^{-6} $^{o}C^{-1}$ for LSF46-LSCF8291. Unfortunately, the thermal expansion coefficient of the composites is only 6-8 % lower.

As compared between LSF37-LSCF8291 (σ = 1,000 S/cm at 650°C, TEC = 18.15 x 10^{-6} $^{o}C^{-1}$) and LSF46-LSCF8291 (σ = 882 S/cm at 650°C, TEC = 18.10 x 10^{-6} $^{o}C^{-1}$), the TEC values of both composites did not differ significantly but the conductivity of LSF37-LSCF8291 was very higher than LSF46-LSCF8291. When adding 33 wt% LSF37, the conductivity value was slightly reduced but the TEC value was reduced from 19.47 x 10^{-6} to 18.15 x 10^{-6} $^{o}C^{-1}$. For LSF46-LSCF8291, the conductivity value was reduced from 1,040.42 to 882.69 S/cm and the TEC value was reduced from 19.47 x 10^{-6} to 18.10 x 10^{-6} $^{o}C^{-1}$. In summary, LSF-LSCF composites exhibit enhanced thermomechanical properties compared to single phase LSCF, while the electrical conducting property of these materials still have high values.

4.2 Suggestions

From experiment results, the future work should be focused on the following:

1. Determination for oxygen permeability of LSF37-LSCF8291 composites in a weight ratio of 1:3.
2. Study for the electrochemical performance of LSF37-LSCF8291 composite in a weight ratio of 1:3 specimen in single cell testing.

REFERENCES

[1] Stambouli, A.B., and Traversa, E. Fuel Cells, an Alternative to Standard Sources of Energy. Renewable and Sustainable Energy Reviews 6 (2002): 297-306.

[2] Parsons, I. Solid Oxide Fuel Cell. Fuel Cell Handbook., Fifth Edition ed., U.S. Department of Energy Office of Fossil Energy, Morgantown (2000): 1.

[3] Solid State Energy Conversion Alliance (SECA). Solid Oxide Fuel Cells (SOFCs) [Online]. (n.d.). Available from: http://www.netl.doe.gov/technologies/coalpower/fuelcells/seca [2010, September 16]

[4] Singhal, S.C. Science and Technology of Solid-Oxide Fuel Cells. Materials Research Society Bulletin 25 (2000): 16-21.

[5] Electrochemistry Encyclopedia. Solid Oxide Fuel Cells (SOFCs) [Online]. (n.d.). Available from: http://electrochem.cwru.edu/encycl [2010, September 16]

[6] Ishihara, T. Perovskite Oxide for Solid Oxide Fuel Cells. Fuel Cells and Hydrogen Energy (2009): 1-7.

[7] Peña, M.A., and Fierro, J.L.G. Chemical Structures and Performance of Perovskite Oxides. Chemical Reviews 101 (2001): 1981-2017.

[8] Rao, C.N.R., Gopalakrishnan, J., and Vidyasagar, K. Superstructure, Ordered Defects and Nonstoichiometry in Metal Oxides of Perovskite and Related Structure. Indian Journal of Chemistry 23A (1984): 265-284.

[9] Teraoka, Y., Nobunaga, T., and Yamazoe, N. Effect of Cation Substitution on the Oxygen Semipermeability of Perovskite-Type Oxide. Chemistry Latters (1988): 503-506.

[10] Goodenough, J.B., and Longo, J.M. Crystallographic and Magnetic Properties of Perovskite and Perovskite-Related Compounds. Landholt-Bornstein Numerical Data and Functional Relationships in Science and Technology New Series Group III/vol. 4a, Spinger-Verlag: Berlin-Heiderberg, 1970.

[11] West, A.R. Solid State Chemistry and Its Applications, John Wiley & Sons, Chichester, 1984.

[12] Tablet, C., et al. Oxygen Permeation Study of Perovskite Hollow Fiber Membranes. Catalysis in Membrane Reactors 104 (2005): 126-130.

[13] Taheri, Z., et al. Comparison of Oxygen Permeation Through Some Perovskite Membranes Synthesized with EDTNAD. Reaction Kinetics, Mechanisms and Catalysis, Budapest Hungary: Akadémiai Kiadó, 2010.

[14] Nagamoto, H., Hayashi, K., and Inoue, H. Methane Oxidation by Oxygen Transported Through Solid Electrolyte. Journal of Catalysis 126 (1990): 671-673.

[15] Schmidt, H., Jonschker, G., Goedicke, S., and Mennig, M. The Sol-Gel Process as a Basic Technology for Nanoparticle-Dispersed Inorganic-Organic Composites. Journal of Sol-Gel Science and Technology 19 (2000): 39-51.

[16] Encyclopædia Britannica. Advanced Ceramics [Online]. (n.d.). Available from: http://www.britannica.com/EBchecked/topic/6657/advanced-ceramics [2010, September 26]

[17] Scholarly Materials and Research at Tech (SMARTech). Continuous and Batch Hydrothermal Synthesis of Metal Oxide Nanoparticles and Metal Oxide-Activated Carbon Nanocomposites [Online]. (n.d.). Available from: http://smartech. gatech.edu/handle/1853/13982 [2010, September 26]

[18] Wikipedia. Hydrothermal Synthesis [Online]. (n.d.). Available from: http://en.wikipedia.org/wiki/Hydrothermal_synthesis [2010, September 26]

[19] Roy, D.M., and Oyefesobi, S.O. Preparation of Very Reactive Ca_2SiO_4 Powder. Journal of the American Ceramic Society 60 (1977): 178.

[20] Kuczynski, G.C. Transactions of the American Institute of Mining, Metallurgical, and Petroleum Engineering. Journal of Applied Physics 21 (1950): 632-637.

[21] Lenntech. Calcination [Online]. (n.d.). Available from: http://www.lenntech.com /chemistry/calcination.htm [2010, September 28]

[22] Gopalan, P., Bhandari, S., Kulkarni, A.R., and Palkar, V.R. Effect of Preparative Parameters on the Electrical Conductivity of Li_2SO_4 - Al_2O_3 Composites. Materials Reasearch Bulletin 37 (2002): 2043-2053.

[23] Shiratori, Y., Tietz, F., Buchkremer, H.P., and Stöver, D. YSZ - MgO Composite Electrolyte with Adjusted Thermal Expansion Coefficient to Other SOFC Components. Solid State Ionics 164 (2003): 27-33.

[24] Dyck, C.R., Yu, Z.B., and Krstic, V.D. Thermal Expansion Matching of Gd_{1-x} $Sr_xCoO_{3-\delta}$ Composite Cathodes to $Ce_{0.8}Gd_{0.2}O_{1.95}$ IT-SOFC Electrolytes. Solid State Ionics 171 (2004): 17-23.

[25] Huang, Y., Vohs, J.M., and Gorte, R.J. Fabrication of Sr-Doped $LaFeO_3$ - YSZ Composite Cathodes. Journal of the Electrochemical Society 151 (2004): A646-A651.

[26] Pelosato, R., Sora, I.N., Dotelli, G., Ruffo, R., and Mari, C.M. Characterization of (1-x) $La_{0.83}Sr_{0.17}Ga_{0.83}Mg_{0.17}O_{2.83}$ - $xLa_{0.8}Sr_{0.2}MnO_3$ ($0 \leq x \leq 1$) Composite Cathodes. Journal of the European Ceramic Society 25 (2005): 2587-2591.

[27] Zhou, W., et al. $Ba_{0.5}Sr_{0.5}Co_{0.8}$ $Fe_{0.2}O_{3-\delta}$ + $LaCoO_3$ Composite Cathode for $Sm_{0.2}Ce_{0.8}O_{1.9}$-Electrolyte Based Intermediate-Temperature Solid-Oxide Fuel Cells. Journal of Power Sources 168 (2007): 330-337.

[28] Xu, Q., et al. Structure, Electrical Conducting and Thermal Expansion Properties of $La_{0.6}Sr_{0.4}Co_{0.8}$ $Fe_{0.2}O_{3-\delta}$ - $Ce_{0.8}Sm_{0.2}O_{2-\delta}$ Composite Cathodes. Journal of Alloys and Compounds 454 (2008): 460-465.

[29] Zhu, W., et al. Study on $Ba_{0.5}Sr_{0.5}Co_{0.8}Fe_{0.2}O_{3-\delta}$ - $Sm_{0.5}Sr_{0.5}CoO_{3-\delta}$ Composite Cathode Materials for IT-SOFCs. Journal of Alloys and Compounds 465 (2008): 274-279.

[30] Zhou, W., Guo, Y., Ran, R., and Shao, Z. A Composite Oxygen-Reduction Electrode Composed of $SrSc_{0.2}Co_{0.8}O_{3-\delta}$ Perovskite and $Sm_{0.2}Ce_{0.8}O_{1.9}$ for an Intermediate-Temperature Solid-Oxide Fuel Cell. Journal of International Hydrogen Energy 35 (2010): 5601-5610.

[31] Zhang, Y., Zhoua, Q., and Hea, T. $La_{0.7}Ca_{0.3}CrO_3$ - $Ce_{0.8}Gd_{0.2}O_{1.9}$ Composites as Symmetrical Electrodes for Solid-Oxide Fuel Cells. Journal of Power Sources 196 (2011): 76-83.

[32] Ortiz-Vitoriano, N., Ruizde, L.I., Arriortua, M.I., and Rojo, T. Optimization of $La_{0.6}Ca_{0.4}Fe_{0.8}Ni_{0.2}O_3$ - $Ce_{0.8}Sm_{0.2}O_2$ Composite Cathodes for Intermediate-Temperature Solid Oxide Fuel Cells. Journal of Power Sources (2010).

[33] Petric, A., Huang, P., and Tietz, F. Evaluation of La–Sr–Co–Fe–O Perovskites for Solid Oxide Fuel Cells and Gas Separation Membranes. Solid State Ionics 135 (2000): 719-725.

[34] Tai, L.W., Nasrallah, M.M., Anderson, H.U., Sparlin, D.M., and Sehlin, S.R. Structure and Electrical Properties of $La_{1-x}Sr_xCo_{1-y}Fe_yO_3$. Part 2. The System La_{1-x} $Sr_xCo_{0.2}Fe_{0.8}O_3$. Solid State Ionics 76 (1995): 273-283.

[35] Armstrong, T.R., Stevenson, J.W., Pederson, L.R., and Raney, P.E. Dimensional Instability of Doped Lanthanum Chromite. Journal of the Electrochemical Society 143 (1996): 2919-2925.

[36] Vidal, K., et al. Isolating the Effect of Doping in the Structure and Conductivity of $(Ln_{1-x}M_x)FeO_{3-\delta}$ Perovskites. Solid State Ionics 178 (2007): 1310-1316.

[37] Patrakeev, M.V., Leonidov, I.A., Kozhevnikov, V.L., and Poeppelmeier, K.R. P-Type Electron Transport in $La_{1-x}Sr_xFe_{3-\delta}$ at High Temperatures. Solid State Chemistry 178 (2005): 921-927.

[38] Virattayanon, N. Synthesis of $La_{0.7}Sr_{0.3}Fe_{1-x}M_xO_3$ (M= Ni, Cu, Al and Mn) as Anode Materials for Solid Oxide Fuel Cell. Master's Thesis, Program in Petrochemistry and Polymer Science Faculty of Science Chulalongkorn University, 2008.

[39] Li, S., Lü, Z., Huang, X., and Su, W. Thermal, Electrical, and Electrochemical Properties of Nd-Doped $Ba_{0.5}Sr_{0.5}Co_{0.8}Fe_{0.2}O_{3-\delta}$ as a Cathode Material for SOFC. Solid State Ionics 178 (2008): 1853-1858.

[40] Shao, Z., Xiong, G., Tong, J., Dong, H., and Yang, W. Ba Effect in Doped $Sr(Co_{0.8}Fe_{0.2})O_{3-\delta}$ on the Phase Structure and Oxygen Permeation Properties of the Dense Ceramic Membranes. Separation and Purification Technology 25 (2001): 419-429.

[41] Justea, E., et al. Oxygen Permeation, Thermal and Chemical Expansions of (La, Sr)(Fe, Ga)$O_{3-\delta}$ Perovskite Membranes. Journal of Membrane Science 319 (2008): 185-191.

[42] Roth, R.S. Classification of Perovskite and Other ABO_3-Type Compounds. Journal of Research of the National Bureau of Standards 58 (1957): 75-88.

[43] Tai, L.W., Nasrallah, M.M., Anderson, H.U., Sparlin, D.M., and Sehlin, S.R. Structure and Electrical Properties of $La_{1-x}Sr_xCo_{1-y}Fe_yO_3$. Part 1. The System $La_{0.8}Sr_{0.2}Co_{1-y}Fe_yO_3$. Solid State Ionics 76 (1995): 259-271.

[44] Hong, L., et al. Effect of B-site Doping on $Sm_{0.5}Sr_{0.5}M_xCo_{1-x}O_{3-\delta}$ Properties for IT-SOFC Cathode Material (M = Fe, Mn). Materials Research Bulletin 42 (2007): 1999-2012.

[45] Lin, Y., and Barnett, S.A. $La_{0.9}Sr_{0.1}Ga_{0.8}Mg_{0.2}O_{3-\delta}$-$La_{0.6}Sr_{0.4}Co_{0.2}Fe_{0.8}O_{3-\theta}$ Composite Cathodes for Intermediate-Temperature Solid Oxide Fuel Cells. Solid State Ionics 179 (2008): 420-427.

[46] Lu, L., Guo, Y., Zhang, H., and Jin, J. Electrochemical Performance of $La_2NiO_{4+\delta}$ - $La_{0.6}Sr_{0.4}Co_{0.2}Fe_{0.8}O_{3-\delta}$ Composite Cathodes for Intermediate Temperature Solid Oxide Fuel Cells. Materials Research Bulletin 45 (2010): 1135-1140.

[47] Zhou, X., Zhu, M., Deng, F., Meng, G., and Liu, X. Electrical Properties, Sintering and Thermal Expansion Behavior of Composite Ceramic Interconnecting Materials, $La_{0.7}Ca_{0.3}CrO_{3-\delta}/Y_{0.2}Ce_{0.8}O_{1.9}$ for SOFCs. Acta Materialia 55 (2007): 2113-2118.

APPENDICES

APPENDIX

APPENDIX A

Tolerance number

Goldschmidt (1926) defined the tolerance limits of the size of ions through a tolerance factor, t as Equation (A.1)

$$t = (r_A + r_O)/ [\sqrt{2} (r_B + r_O)] \quad (A.1)$$

where r_A, r_B, and r_O are the radii of respective ions. For the substituted perovskite at A and B site, $A_{1-x}A'_xB_{1-y}B'_yO_{3-\delta}$, r_A and r_B were calcuated from the sum of each metal at A site and B site, respectively, time its compostition. The atomic weight, ionic charge, coordination number, and ionic radius of all concerned metals were shown in Table A.1

Table A.1 Atomic weight, ionic charge, coordination number, and ionic radius of concerned metals

Metal	Atomic weight	Ionic charge	Coordination No.	Ionic radius (Å)
La	138.92	3+	12	1.032
Fe	55.85	3+	6	0.645
Sr	87.62	2+	12	1.180
Co	58.94	2+	6	0.790
O	16.00	2-	6	1.400

Therefore, as Equation A.1 the tolerance number of perovskite compounds such as LSCF 8291 was calculated as below.

$$\text{tolerance number of LSCF8291} = \frac{(1.032 \times 0.8) + (1.18 \times 0.2) + 1.40}{\sqrt{2}\,[(0.79 \times 0.9) + (0.645 \times 0.1) + 1.40]}$$

$$= 0.80$$

APPENDIX B

Activation Energy (Ea)

Arrhenius plot of LSCF 8291 is given in Figure B-1. The linear part can be described by the small polaron conduction mechanism, following the formula:

$$\sigma = (A/T)\, e^{(-Ea/RT)}$$

$$\ln(\sigma T) = \ln A\, e^{(-Ea/RT)}$$

$$\ln(\sigma T) = \ln e^{(-Ea/RT)} + \ln A \qquad \text{(B.1)}$$

$$\ln(\sigma T) = (-Ea/R)\,(1000/T) + \ln A$$

y **slope** **x** **intercept y axis**

$$-Ea/K = \text{Slope of the linear}$$

$$Ea = -\text{Slope} \times K$$

A is material constant including the carrier concentration term,

σ = The specific conductivity (S/cm)

Ea = The activation energy (kJ/mol)

T = Temperature (K)

R = The gas constant = 8.314472 J/K.mol

From Equation B.1 Arrhenius plot of ln σT versus 1000/*T* gives a straight line, whose slope and intercept can be used to determine *E*a and *A*.

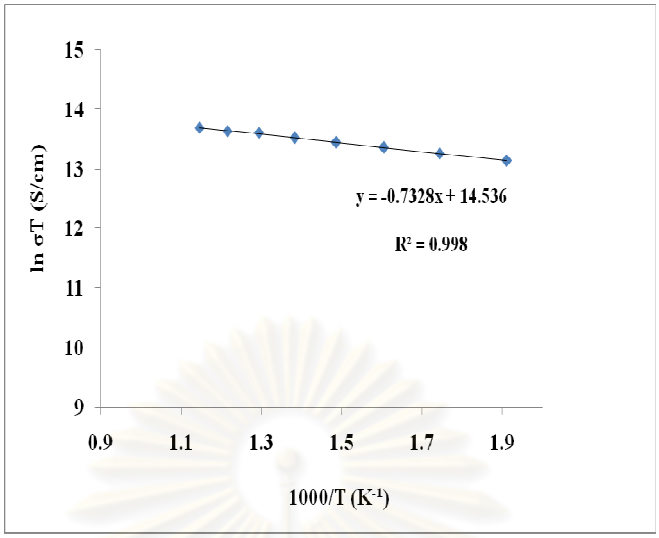

Figure B.1 Arrhenius plot of the electrical conductivity of $La_{0.8}Sr_{0.2}Co_{0.9}Fe_{0.1}O_{3-\delta}$.

The activation energy was calculated from the slope of the straight line of figure B.1. For example, the activation energy (*E*a) of $La_{0.8}Sr_{0.2}Co_{0.9}Fe_{0.1}O_{3-\delta}$, was calculated as below:

$$\text{Slope} = -E\text{a}/k$$

$$\text{Slope} = -E\text{a}\ /8.314472$$

$$E\text{a} = -\text{slope x } 8.314472$$

$$E\text{a} = -\ (-0.7328) \text{ x } 8.314472$$

$$E\text{a} = 6.09 \text{ kJ/mol}$$

APPENDIX C

Table C.1 Specific conductivity of $La_{1-x}Sr_xFeO_{3-\delta}$ (x = 0.6-0.7).

Ratio	Specific conductivity, σ (S/cm)						
	27°C	**250°C**	**300°C**	**350°C**	**400°C**	**450°C**	**500°C**
x = 0.6	18	185	237	282	313	338	363
x = 0.7	19	315	346	368	384	400	414

Ratio	Specific conductivity, σ (S/cm)						
	550°C	**600°C**	**650°C**	**700°C**	**750°C**	**800°C**	**σ_{max} (T, °C)**
x = 0.6	391	386	357	305	253	203	391 (550)
x = 0.7	417	402	368	315	266	216	417 (550)

Table C.2 Specific conductivity of $La_{0.8}Sr_{0.2}Co_{1-x}Fe_xO_{3-\delta}$ (x = 0.1-0.2).

Ratio	**Specific conductivity, σ (S/cm)**						
	27°C	**250°C**	**300°C**	**350°C**	**400°C**	**450°C**	**500°C**
x = 0.1	686	965	995	996	1,011	1,012	1,020
x = 0.2	486	718	761	828	873	911	947

Ratio	**Specific conductivity, σ (S/cm)**						
	550°C	**600°C**	**650°C**	**700°C**	**750°C**	**800°C**	**σ_{max} (T, °C)**
x = 0.1	1,027	1,031	1,040	1,030	1,015	1,000	1,040 (650)
x = 0.2	958	972	979	970	966	959	979 (650)

Table C.3 Specific conductivity of LSF37-LSCF8291 composites with different weight ratios of LSCF after calcined at 800°C.

Weight ratio of LSCF	Specific conductivity, σ (S/cm)						
	27°C	**250°C**	**300°C**	**350°C**	**400°C**	**450°C**	**500°C**
0.25	226	395	433	458	487	514	537
0.33	319	459	496	525	548	568	590
0.50	409	549	586	615	638	651	654
0.67	511	658	689	707	738	761	770
0.75	525	779	806	838	868	910	938

Weight ratio of LSCF	Specific conductivity, σ (S/cm)						
	550°C	**600°C**	**650°C**	**700°C**	**750°C**	**800°C**	**σ_{max} (T, °C)**
0.25	559	544	514	474	435	391	559 (550)
0.33	600	592	569	536	501	440	600 (550)
0.50	654	635	615	584	553	497	654 (550)
0.67	792	824	837	817	791	769	837 (650)
0.75	957	979	1,000	985	974	957	1,000 (650)

106

Table C.4 Specific conductivity of LSF37-LSCF8291 composites with different weight ratios of LSCF after calcined at 900°C.

Weight ratio of LSCF	Specific conductivity, σ (S/cm)						
	27°C	**250°C**	**300°C**	**350°C**	**400°C**	**450°C**	**500°C**
0.25	234	392	428	467	498	539	558
0.33	310	479	521	552	574	591	613
0.50	400	602	630	659	676	686	699
0.67	446	657	701	736	771	805	830
0.75	520	815	853	883	917	939	952

Weight ratio of LSCF	Specific conductivity, σ (S/cm)						
	550°C	**600°C**	**650°C**	**700°C**	**750°C**	**800°C**	**σ_{max} (T, °C)**
0.25	574	555	522	495	470	407	574 (550)
0.33	617	610	584	552	510	447	617 (550)
0.50	701	684	650	615	574	514	701 (550)
0.67	849	864	869	867	853	825	869 (650)
0.75	963	976	996	989	975	957	996 (650)

107

Table C.5 Specific conductivity of LSF37-LSCF8291 composites in a weight ratio of 1:3 with different sintering temperatures for 10 hours.

Sintering temp. (^oC)	**Specific conductivity, σ (S/cm)**						
	27^oC	**250^oC**	**300^oC**	**350^oC**	**400^oC**	**450^oC**	**500^oC**
1,200	493	776	796	821	835	853	863
1,300	525	779	806	838	868	910	938
1,400	484	749	783	810	828	843	853

Sintering temp. (^oC)	**Specific conductivity, σ (S/cm)**						
	550^oC	**600^oC**	**650^oC**	**700^oC**	**750^oC**	**800^oC**	**σ_{max} (T, ^oC)**
1,200	873	875	879	867	861	852	879 (650)
1,300	957	979	1,000	985	974	957	1,000 (650)
1,400	861	865	867	861	854	847	867 (650)

108

Table C.6 Specific conductivity of LSF37-LSCF8291 composites in a weight ratio of 1:3 with different sintering time for sintered at 1,300^{o}C.

Sintering time (hours)	**Specific conductivity, σ (S/cm)**						
	27^{o}C	**250^{o}C**	**300^{o}C**	**350^{o}C**	**400^{o}C**	**450^{o}C**	**500^{o}C**
8	502	753	780	807	826	844	861
10	525	779	806	838	868	910	938
12	260	707	748	782	805	825	834
15	467	717	766	792	812	822	831

Sintering time (hours)	**Specific conductivity, σ (S/cm)**						
	550^{o}C	**600^{o}C**	**650^{o}C**	**700^{o}C**	**750^{o}C**	**800^{o}C**	**σ_{max} (T, ^{o}C)**
8	864	874	876	868	865	855	876 (650)
10	957	979	1,000	985	974	957	1,000 (650)
12	839	842	845	841	838	831	845 (650)
15	836	842	843	840	835	822	843 (650)

109

Table C.7 Specific conductivity of LSF37-LSCF8282 composites with different weight ratios of LSCF after calcined at 800^{o}C.

Weight ratio of LSCF	**Specific conductivity, σ (S/cm)**						
	27^{o}C	**250^{o}C**	**300^{o}C**	**350^{o}C**	**400^{o}C**	**450^{o}C**	**500^{o}C**
0.25	190	388	407	427	435	441	444
0.33	238	430	454	478	485	491	500
0.50	411	526	552	559	568	570	578
0.67	491	628	659	667	678	681	690
0.75	497	703	735	785	806	821	834

Weight ratio of LSCF	**Specific conductivity, σ (S/cm)**						
	550^{o}C	**600^{o}C**	**650^{o}C**	**700^{o}C**	**750^{o}C**	**800^{o}C**	**σ_{max} (T, ^{o}C)**
0.25	447	427	391	339	290	243	447 (550)
0.33	500	480	434	379	320	269	500 (550)
0.50	580	581	584	567	546	518	584 (650)
0.67	692	694	697	677	651	619	697 (650)
0.75	847	849	852	829	790	753	852 (650)

110

Table C.8 Specific conductivity of LSF37-LSCF8282 composites with different weight ratios of LSCF after calcined at 900^{o}C.

Weight ratio of LSCF	**Specific conductivity, σ (S/cm)**						
	27^{o}C	**250^{o}C**	**300^{o}C**	**350^{o}C**	**400^{o}C**	**450^{o}C**	**500^{o}C**
0.25	208	396	425	445	449	455	460
0.33	259	463	489	507	511	516	517
0.50	339	507	531	554	570	582	591
0.67	404	604	632	660	678	693	703
0.75	488	717	761	803	826	842	844

Weight ratio of LSCF	**Specific conductivity, σ (S/cm)**						
	550^{o}C	**600^{o}C**	**650^{o}C**	**700^{o}C**	**750^{o}C**	**800^{o}C**	**σ_{max} (T, ^{o}C)**
0.25	464	434	398	350	305	233	464 (550)
0.33	517	494	444	378	318	241	517 (550)
0.50	595	598	601	587	568	535	601 (650)
0.67	708	712	715	699	676	636	715 (650)
0.75	850	855	862	839	808	769	862 (650)

111

Table C.9 Specific conductivity of LSF37-LSCF8282 composites in a weight ratio of 1:3 with different sintering temperatures for 10 hours.

Sintering temp. (^oC)	**Specific conductivity, σ (S/cm)**						
	27^oC	**250^oC**	**300^oC**	**350^oC**	**400^oC**	**450^oC**	**500^oC**
1,200	456	660	686	710	724	736	748
1,300	497	703	735	785	806	821	834
1,400	372	615	635	658	681	694	712

Sintering temp. (^oC)	**Specific conductivity, σ (S/cm)**						
	550^oC	**600^oC**	**650^oC**	**700^oC**	**750^oC**	**800^oC**	**σ_{max} (T, ^oC)**
1,200	750	752	752	740	722	691	752 (650)
1,300	847	849	852	829	790	753	852 (650)
1,400	712	715	720	720	709	686	720 (650)

112

Table C.10 Specific conductivity of LSF37-LSCF8282 composites in a weight ratio of 1:3 with different sintering time for sintered at 1,300^{o}C.

Sintering time (hours)	**Specific conductivity, σ (S/cm)**						
	27^{o}C	**250^{o}C**	**300^{o}C**	**350^{o}C**	**400^{o}C**	**450^{o}C**	**500^{o}C**
8	487	689	720	740	761	776	778
10	497	703	735	785	806	821	834
12	468	662	692	711	732	746	748
15	465	658	688	706	727	741	743

Sintering time (hours)	**Specific conductivity, σ (S/cm)**						
	550^{o}C	**600^{o}C**	**650^{o}C**	**700^{o}C**	**750^{o}C**	**800^{o}C**	**σ_{max} (T, ^{o}C)**
8	782	783	785	774	745	709	785 (650)
10	847	849	852	829	790	753	852 (650)
12	751	753	754	744	716	682	754 (650)
15	746	747	749	738	711	677	749 (650)

113

Table C.11 Specific conductivity of LSF46-LSCF8291 composites with different weight ratios of LSCF after calcined at 800°C.

Weight ratio of LSCF	Specific conductivity, σ (S/cm)						
	27°C	**250°C**	**300°C**	**350°C**	**400°C**	**450°C**	**500°C**
0.25	145	339	367	388	405	425	439
0.33	260	440	465	484	492	501	503
0.50	254	482	508	538	557	573	583
0.67	392	651	684	711	734	753	770
0.75	488	729	759	794	820	845	854

Weight ratio of LSCF	Specific conductivity, σ (S/cm)						
	550°C	**600°C**	**650°C**	**700°C**	**750°C**	**800°C**	**σ_{max} (T, °C)**
0.25	450	449	447	443	420	393	450 (550)
0.33	503	493	481	469	442	422	503 (550)
0.50	589	593	596	592	587	554	596 (650)
0.67	772	785	789	789	781	767	789 (650)
0.75	868	877	882	882	882	873	882 (650)

Table C.12 Specific conductivity of LSF46-LSCF8291 composites with different weight ratios of LSCF after calcined at 900^{o}C.

Weight ratio of LSCF	**Specific conductivity, σ (S/cm)**						
	27^{o}C	**250^{o}C**	**300^{o}C**	**350^{o}C**	**400^{o}C**	**450^{o}C**	**500^{o}C**
0.25	151	352	381	403	422	442	457
0.33	268	453	479	498	507	516	518
0.50	294	498	526	546	568	585	599
0.67	425	674	703	726	756	783	792
0.75	502	751	781	817	844	870	879

Weight ratio of LSCF	**Specific conductivity, σ (S/cm)**						
	550^{o}C	**600^{o}C**	**650^{o}C**	**700^{o}C**	**750^{o}C**	**800^{o}C**	**σ_{max} (T, ^{o}C)**
0.25	468	466	465	460	447	409	468 (550)
0.33	518	513	505	487	474	434	518 (550)
0.50	616	616	616	612	600	568	616 (650)
0.67	802	805	810	796	787	760	810 (650)
0.75	894	903	908	908	908	898	908 (650)

Table C.13 Specific conductivity of LSF46-LSCF8291 composites in a weight ratio of 1:3 with different sintering temperatures for 10 hours.

Sintering temp. (^oC)	**Specific conductivity, σ (S/cm)**						
	27^oC	**250^oC**	**300^oC**	**350^oC**	**400^oC**	**450^oC**	**500^oC**
1,200	464	694	722	756	781	805	813
1,300	488	730	759	794	820	845	854
1,400	445	666	693	725	749	772	780

Sintering temp. (^oC)	**Specific conductivity, σ (S/cm)**						
	550^oC	**600^oC**	**650^oC**	**700^oC**	**750^oC**	**800^oC**	**σ_{max} (T, ^oC)**
1,200	826	835	840	840	840	831	840 (650)
1,300	868	877	882	882	882	873	882 (650)
1,400	793	801	806	806	806	797	806 (650)

116

Table C.14 Specific conductivity of LSF46-LSCF8291 composites in a weight ratio of 1:3 with different sintering time for sintered at 1,300^{o}C.

Sintering time (hours)	**Specific conductivity, σ (S/cm)**						
	27^{o}C	**250^{o}C**	**300^{o}C**	**350^{o}C**	**400^{o}C**	**450^{o}C**	**500^{o}C**
8	505	693	733	761	779	800	818
10	488	730	759	794	820	845	854
12	384	651	687	712	741	763	782
15	379	642	678	703	731	753	771

Sintering time (hours)	**Specific conductivity, σ (S/cm)**						
	550^{o}C	**600^{o}C**	**650^{o}C**	**700^{o}C**	**750^{o}C**	**800^{o}C**	**σ_{max} (T, ^{o}C)**
8	827	834	837	834	831	826	837 (650)
10	868	877	882	882	882	873	882 (650)
12	803	803	803	799	783	741	803 (650)
15	793	793	793	788	772	731	793 (650)

117

Table C.15 Specific conductivity of LSF46-LSCF8282 composites with different weight ratios of LSCF after calcined at 800°C.

Weight ratio of LSCF	Specific conductivity, σ (S/cm)						
	27°C	**250°C**	**300°C**	**350°C**	**400°C**	**450°C**	**500°C**
0.25	122	257	294	328	357	383	415
0.33	166	309	353	379	411	432	460
0.50	201	347	389	414	438	461	483
0.67	276	411	462	492	529	551	573
0.75	326	522	563	598	630	673	696

Weight ratio of LSCF	Specific conductivity, σ (S/cm)						
	550°C	**600°C**	**650°C**	**700°C**	**750°C**	**800°C**	**σ_{max} (T, °C)**
0.25	425	412	383	343	305	252	425 (550)
0.33	480	472	460	437	403	371	480 (550)
0.50	505	512	521	509	488	465	521 (650)
0.67	602	626	639	636	631	623	639 (650)
0.75	717	742	756	751	741	728	756 (650)

118

Table C.16 Specific conductivity of LSF46-LSCF8282 composites with different weight ratios of LSCF after calcined at 900^{o}C.

Weight ratio of LSCF	**Specific conductivity, σ (S/cm)**						
	27^{o}C	**250^{o}C**	**300^{o}C**	**350^{o}C**	**400^{o}C**	**450^{o}C**	**500^{o}C**
0.25	130	273	319	357	396	436	454
0.33	155	297	338	378	419	460	487
0.50	192	329	372	408	443	481	504
0.67	280	428	469	500	537	561	583
0.75	333	568	613	647	681	699	719

Weight ratio of LSCF	**Specific conductivity, σ (S/cm)**						
	550^{o}C	**600^{o}C**	**650^{o}C**	**700^{o}C**	**750^{o}C**	**800^{o}C**	**σ_{max} (T, ^{o}C)**
0.25	461	442	420	384	349	308	461 (550)
0.33	502	491	470	449	427	405	502 (550)
0.50	526	538	544	531	510	486	544 (650)
0.67	602	626	650	647	631	613	650 (650)
0.75	737	747	764	763	750	737	764 (650)

119

Table C.17 Specific conductivity of LSF46-LSCF8282 composites in a weight ratio of 1:3 with different sintering temperatures for 10 hours.

Sintering temp. (^oC)	**Specific conductivity, σ (S/cm)**						
	27^oC	**250^oC**	**300^oC**	**350^oC**	**400^oC**	**450^oC**	**500^oC**
1,200	310	504	545	588	614	641	655
1,300	326	522	563	598	630	673	696
1,400	267	493	533	566	595	617	636

Sintering temp. (^oC)	**Specific conductivity, σ (S/cm)**						
	550^oC	**600^oC**	**650^oC**	**700^oC**	**750^oC**	**800^oC**	**σ_{max} (T, ^oC)**
1,200	675	689	714	712	707	697	714 (650)
1,300	717	742	756	751	741	728	756 (650)
1,400	653	666	686	676	656	644	686 (650)

120

Table C.18 Specific conductivity of LSF46-LSCF8282 composites in a weight ratio of 1:3 with different sintering time for sintered at 1,300^{o}C.

Sintering time (hours)	**Specific conductivity, σ (S/cm)**						
	27^{o}C	**250^{o}C**	**300^{o}C**	**350^{o}C**	**400^{o}C**	**450^{o}C**	**500^{o}C**
8	317	491	534	569	611	642	665
10	326	522	563	598	630	673	696
12	289	459	501	543	577	610	638
15	278	426	467	501	534	574	605

Sintering time (hours)	**Specific conductivity, σ (S/cm)**						
	550^{o}C	**600^{o}C**	**650^{o}C**	**700^{o}C**	**750^{o}C**	**800^{o}C**	**σ_{max} (T, ^{o}C)**
8	700	717	726	720	710	702	726 (650)
10	717	742	756	751	741	728	756 (650)
12	671	695	704	700	680	654	704 (650)
15	638	664	678	663	638	603	678 (650)

121

VITAE

Miss Petploy Vicheantawatchai was born on January 2, 1983 in Bangkok, Thailand. She graduated with Bachelor's Degree in Chemistry from Faculty of Science, Mahidol University in 2005. She continued her study in Petrochemistry and Polymer Science Program, Faculty of Science, Chulalongkorn University in 2008 and completed in 2011.

PRESENTATIONS:

October 26-28, 2010.

Poster Presentation: "Electrical conductivity of $La_{1-x}Sr_xFeO_{3-\delta}$ (LSF) - $La_{0.8}Sr_{0.2}Co_{1-x}Fe_xO_{3-\delta}$ (LSCF) composite oxides" The 36th congress on science and technology of Thailand (STT 36), Thammasat University, Thailand.